POLITECNICO DI MILANO

School of Industrial and Information Engineering

Master of Science Degree in Mathematical Engineering
Computational Science and Engineering

Master Degree Thesis

A fully implicit formulation for Navier-Stokes/Darcy coupling

Supervisor
Prof. Luca Formaggia
Co-supervisors
Dr. Anna Scotti
Prof. Dr.-Ing. Rainer Helmig

Candidate
Andrea Vescovini
Matr. 872279

Academic Year 2017–2018

Abstract

Exchange processes between free-flows and porous-media flows are common in many industrial and environmental applications. In the case of turbulent flows and rough interfaces, an accurate description of the free-flow is important because the turbulent eddies near the interface strongly affect the exchanges.

The aim of this thesis is the investigation of the effects of rough interfaces in coupled free-flow and porous-media flow systems. In particular, this work exploits the application of high resolution schemes for the finite volumes discretization of the convective term in the momentum equation of the incompressible Navier-Stokes equations. The focus is on the Total Variation Diminishing (TVD) methods, which have been implemented in the code DuMu^{x}, within the framework of a staggered-grid approach. Two possible extension to the case of non-uniform grids have been considered.

Several comparison tests with the first order upwind method have been performed, showing more accurate solutions for the TVD methods on the same grid. Afterwards the RANS equations have been used in order to simulate turbulent flows, employing the k-ω turbulence model. The backward facing step test has been used to validate the results against the ones from the NASA CFL3D code. A good prediction of the reattachment length has been obtained. At last, a coupled free and porous-medium flow configuration has been studied, with focus on the effect that a rough interface has on the flow field. With high values of permeability, the porous-medium flow, modelled using the Forchheimer's law, has an influence on the flow in the free-flow region.

Keywords: TVD methods, RANS, porous-media, coupled problem, DuMu^{x}.

Sommario

Processi di scambio tra flussi liberi e flussi in mezzi porosi sono comuni in molte applicazioni industriali o ambientali. In caso di regimi turbolenti e interfacce che presentano rugosità, è importante avere un'accurata descrizione del flusso libero, in quanto i vortici che si vengono a creare vicino all'interfaccia, a causa della turbolenza, hanno una grande influenza su tali scambi.

L'obbiettivo di questa tesi è l'investigazione dell'effetto di un'interfaccia rugosa in un sistema accoppiato comprendente un flusso libero ed un flusso in un mezzo poroso. In particolare questo lavoro sfrutta l'applicazione di schemi ad alta risoluzione (high resolution schemes) per la discretizzazione a volumi finiti del termine convettivo nelle equazioni di Navier-Stokes incomprimibili. L'attenzione è rivolta ai metodi Total Variation Diminishing (TVD), i quali sono stati implementati all'interno del codice DuMu^{x}, nell'ambito di una discretizzazione su griglia sfalsata (staggered grid). Sono state inoltre considerate due possibili generalizzazioni al caso di griglie cartesiane non uniformi.

I molteplici test di confronto con il metodo upwind di ordine 1 che sono stati effettuati hanno evidenziato una migliore accuratezza dei metodi TVD a parità di griglia. In seguito, per simulare flussi turbolenti, sono state utilizzate le equazioni RANS, scegliendo il modello di turbolenza k-ω. È stato utilizzato il test del backward facing step per validare i risultati, confrontandoli con quelli disponibili prodotti dal codice CFL3D della NASA. È stata ottenuta una buona previsione della distanza di riattacco, in accordo con i risultati di riferimento. Infine è stato studiato un problema accoppiato tra flusso libero e flusso in un mezzo poroso, ponendo attenzione all'effetto che un'interfaccia con ostacoli ha sul campo di velocità. Si è ottenuto che per valori alti di permeabilità il flusso nel mezzo poroso, descritto con la legge di Forchheimer, influenza il flusso libero.

Parole chiave: metodi TVD, RANS, mezzi porosi, problema accoppiato, DuMu^{x}.

Aknowledgements

I thank prof. Formaggia and dr. Scotti for having shown me the possibility of carrying on my thesis in Stuttgart and having helped me to catch it. I thank prof. Helmig, that during my six months of scholarship has helped me a lot with his infinite passion and enthusiasm. I thank all the members of the department LH^2 for the great time spent there in such a friendly and stimulating environment, always willing to implement a new feature in $DuMu^x$ but also to bake a cake for the colleagues. In particular I thank Ned and Melanie, that have supervised my work and were always positive about how it was going and ready to discuss together the last developments.

Infine un ringraziamento speciale a tutti gli amici che hanno condiviso con me questi anni di università per i bei momenti passati insieme, alla mia famiglia, per aver sempre supportato le mie scelte, e a Valeria, che crede sempre in me e mi è sempre vicina.

Funded by the Deutsche Forschungsgemeinschaft (DFG, German Research Foundation) - Project Number 327154368 - SFB 1313

Contents

List of Figures

List of Tables

Chapter 1

Introduction

Flow and transport processes between free-flows and porous-media flows are common in a wide range of environmental, industrial, civil and medical applications. For example a turbulent air flow has a significant effect on the drying rate of an adjacent wet porous-medium like a soil, as studied by Mosthaf [Mos14], Davarzani et al. [Dav+14] and Fetzer [Fet18]. Although systems like this are very common, they involve many different physical phenomena that act at different scales and, due to the variety of time and space scales involved and the complexity of the phenomena, a reliable prediction of the evaporation rates is still a challenge. In Figure 1.1 we can see a schematic representation of the mechanisms that play a role in such a situation, where both transport and thermal effects can be relevant. Moreover, considering natural phenomena, an additional difficulty is given by the intrinsic uncertainty and heterogeneity of material properties, such as the soil porosity, and atmospheric conditions, e.g. the air humidity or the solar radiation.

These studies can be exploited, for example, to better understand the process of soil salinization, one of the most serious agricultural problems in many arid and coastal areas in the world. It consists in the excessive accumulation of salt in the soil pores, with the consequence of a partial or complete loss of fertility. A limited amount of salt precipitation in the soil, due to evaporation of irrigation water, is inevitable, but a mismanaged irrigation plan could lead to salinity problems in the long term, especially in arid areas where irrigation is necessary to increase the production for food supply (see [FAO19]). According to [MT08], more than 6% of world's total land area is affected by salinization. The section of soil which is most affected by salinization is the one near the surface, hence the importance of studying the interactions between the free-flow and the porous-medium flow that occur there. For example, Jambhekar et al. [Jam+16] have investigated the application of kinetic approaches to describe the salt precipitation in a

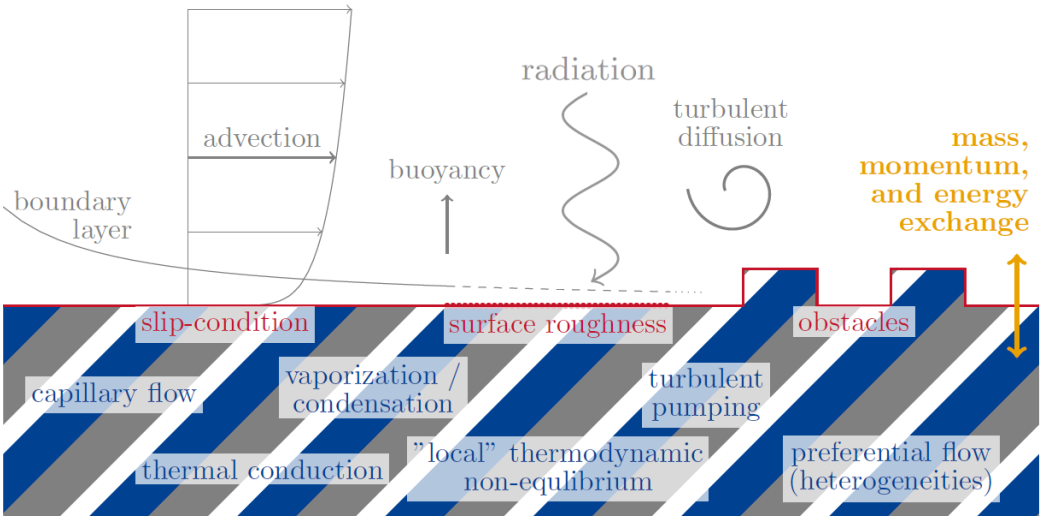

Figure 1.1: Example of physical phenomena affecting the exchange processes between a free-flow and a porous-medium flow. Figure source: [Fet18].

coupled system.

Switching to technical applications, Proton Exchange Membrane (PEM) fuel cells represent a possible alternative power source that, in particular, could be used for transportation. In their design, transport and diffusion phenomena through gas channels and gas diffusers play an important role in the electrochemical reactions that determine the cell performances and efficiency. As we can see in Figure 1.2, reactant gases are transported through gas channels and supplied at the anode and cathode, then they diffuse into porous layers called gas diffusers, that should deliver them uniformly and efficiently to the catalyst layers, where reactions take place (see [Wu16], [Bab14] and [Wal08]). Protons are produced at the anode and transported through the membrane to react with oxygen at the cathode and produce water. The water management within the cells is of great importance, because it is essential to have a certain level of humidity in the membrane in order to facilitate the transport of protons, but an excess of water could flood the catalyst layers, with the result of an inhibition of the reactions. Because of the complex and compact geometry of PEM fuel cells, it is generally difficult and expensive to take measurements, thus mathematical and numerical models are helpful in order to better understand the mechanical, thermal and chemical phenomena that take place and this way improve the cell performances and lifetime.

Other examples of applications can be found in the fields of refrigeration of stored food [Ver+06], cooling systems for aerospace engineering [Dah+14],

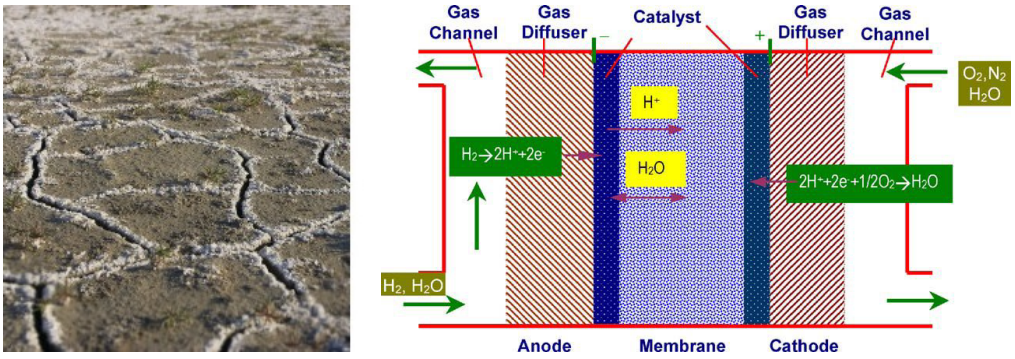

(a) (b)

Figure 1.2: (a): Salt-affected soil. Figure source: [FAO19]. (b): Operation principle of PEM fuel cells. Figure source: [YL05].

ventilation of motorcycle helmets [CD13], wind flow around buildings in urban environments [DBC10] and hemodynamics [BQQ09].

1.1 State of the art

In order to study these processes we focus on the case of the evaporation from a porous material and we consider a system that involves two subdomains: the upper one with a free-flow and the lower one occupied by a porous-medium, represented in Figure 1.1. At the interface between the two subdomains there is exchange of mass, momentum and energy.

Numerical studies of this coupled system can be performed with a *single-domain* approach or with a *two-domain* approach [Fet18]. Within the single-domain approach, the same equations are solved in the whole computational domain, including both the free-flow region and the porous-medium. A first possibility is to use the Navier-Stokes equations to model the fluid motion and thus to perform a direct numerical simulation (DNS) of the whole system. The porous-medium has to be resolved at the pore-scale, thus a detailed knowledge of the pore structure and geometry, which is not easy to obtain for real materials, is necessary. The computational effort is very high because of the strict spatial and temporal requirements of a DNS, all of which increase further if the system is non-isothermal, multi-phase and multi-component. Fattahia et al. [Fat+15] and Krafczyk et al. [Kra+15] have performed DNS in porous-media domains using the lattice Boltzmann method, while Yang et al. [Yan+18] have performed coupled simulations considering idealised coarse porous materials. A cheaper possibility for the case of laminar single-phase

flows is to employ the Brinkman's equation [Bri47], which is a superposition of the Stokes equations and Darcy's law, with a modified viscosity. Then the transition between the two regions can be expressed with a spatial variation of the involved physical parameters, either considering a transition region or admitting a discontinuous variation at the interface. Shavit et al. [SRA04] proposed a modification of the Brinkman's equation and applied it to the case of shallow water flows over porous surfaces.

Within the two-domain approach, adopted also in this thesis, different sets of equations are used in the two subdomains and they are coupled imposing suitable conditions at the interface. This allows to keep separated models to describe phenomena that act on different temporal and spatial scales. The free-flow can be modelled with the Stokes equations, Navier-Stokes equations or Reynolds Averaged Navier-Stokes (RANS) equations, depending on the flow regime. The porous-medium flow, instead, is usually described using a Reference Elementary Volume (REV) scale approach, exploiting the Darcy's law or the Forchheimer's law when the Reynolds number is higher or the Richards' equation when the flow is unsaturated. The interface could also be *complex*, i.e. it could be adapted to store mass, to, for example, take into account information about the formation of droplets (see [Bab14]).

Cimolin and Discacciati [CD13] compared the performances of a single-domain approach exploiting a penalization technique and a two-domain approach, using the Navier-Stokes equations and the Forchheimer's law to model an incompressible, single-phase, single-component flow. They concluded that the former is easier to implement, but the latter more accurately describes the physics of the problem. Alternative approaches may exploit pore-networks models in the porous-medium subdomain, that allow to focus on the pore scale effects, avoiding the complexity of a DNS (see [WJH19]).

Mosthaf et al. [Mos+11] proposed a Stokes/Darcy coupling concept for multi-phase, multi-component, non-isothermal flows. It is based on phenomenological arguments and it tries to be as close as possible to the imposition of thermodynamic equilibrium. Davarzani et al. [Dav+14], instead, focused on the coupling in case of non-equilibrium conditions among phases. Fetzer et al. [FSH16] generalized the equilibrium concept to the case of turbulent flows, in [Fet18] several turbulence models are tested and possible simplifications in the implementation of interface conditions are considered. The effects of turbulence, as well as the non-linear inertial effects of the Navier-Stokes equations, are sometimes neglected for simplicity, but to model natural systems they must be included as they affect the physical factors important in most applications. Another aspect investigated in [Fet18] is the influence of a rough interface between the two subdomains. In particular, both the effects of a sand-grain roughness and of periodical porous obstacles

are studied. Rough interfaces have been taken into account also in [KB04] and [Kuz04] to analyse heat transfer within a duct, while rough boundaries for free-flows are considered in [LYC04] to study flow paths around buildings, in [Bro+18], in a limnological framework, and in [TK08] to study heat exchangers.

Theoretical results about the well-posedness can be found in [DMQ02], for the Stokes/Darcy problem, and in [DQ09], for the Navier-Stokes/Darcy problem. They are based on classical results for saddle-point problems. Regarding the numerical aspects, many different methods have been employed in literature. In [DQ09] several finite elements choices are considered, in [Mos14] the box method is used, while in [Fet18] the same box method is compared to a combined staggered and collocated finite volumes method. In [DMQ02] an iterative algorithm is proposed in order to decouple the two subdomains, while in [RMH15] a temporal decoupling strategy is used.

1.2 Content of the thesis

In this thesis the focus is on the improvement, from the numerical point of view, of the free-flow model with respect to [Fet18] and on the further investigation of the effects of a rough interface between the two subdomains.

When the flow is in a turbulent regime, turbulent eddies develop near the interface and they cascade through consecutively smaller scales until the kinetic energy dissipates into internal thermal energy. Because of their location, they have a strong influence on the exchange processes between the two subdomains, so an accurate evaluation of their behaviour is of crucial importance. Improvements can be obtained with a refinement of the grid, but also by employing high order methods. In particular, in the discretization of the Navier-Stokes equations using finite volumes, the approximation used for the non-linear term $\nabla \cdot (\mathbf{v}\mathbf{v}^{\mathrm{T}})$ plays a key role. A common and easy choice is to employ a first order upwind approximation for the *transported* velocity, but this option can produce solutions with excessive numerical diffusion. Other possibilities are given by high order methods like the Linear Upwind Differencing (LUD) scheme, the Central Differencing (CD) scheme or the Quadratic Upstream Interpolation for Convective Kinetics (QUICK) scheme. Under specific conditions, they can produce accurate solutions but they have also been shown to be unstable in certain situations and to produce overshoots or undershoots that may lead to unphysical values of quantities which, for example, have to be non-negative (see [VM07]). With this in mind, our interest is in the Total Variation Diminishing (TVD) methods, a family of methods that has been derived with the purpose of providing a solution

with a second order accuracy, but without any risk of numerical oscillations. They are called also high resolution methods [Har83].

Using this tool, we study a coupled system involving a turbulent free-flow and a porous-medium flow, considering an isothermal, single-phase, single-component fluid. It is a simplified model with respect to the one employed in [Fet18] to study evaporation processes, but it allows to focus on the fluid mechanical phenomena that occur at the interface. In particular, being the soil surface intrinsically rough in nature, it is important to investigate the effects given by a rough interface, to obtain a deeper understanding of the flow behaviour in this situation.

The thesis is organized as follows. In Chapter 2, the equations employed in the models will be presented, with particular attention to the free-flow equations. In Chapter 3, the finite volume method will be described and, in Subsection 3.1.3, the TVD methods will be introduced. At last, in Chapter 4, the numerical results will be shown. In particular, we will compare the results obtained with the TVD methods with those obtained with the first order upwind scheme. Then, two tests involving turbulent flows are presented and, finally, more complex scenarios involving a rough interface, consisting of cavities or porous obstacles, between a free-flow region and a porous-medium are investigated.

The high order methods mentioned above have been implemented in the framework of the open-source simulator DuMu^{x}: DUNE for multi-{phase, component, scale, physics, ...} flow in porous-media, see [Koc+18] and [Fle+11]. DuMu^{x} is an additional module of DUNE (Distributed and Unified Numerics Environment, [DUN18]) and, through the use of an object-oriented design in conjunction with template programming, it provides a C++ environment that allows an efficient implementation of numerical models related to porous-media flows.

All the source code used for the simulations performed can be found at `https://git.iws.uni-stuttgart.de/dumux-pub/vescovini2019a`, together with the instructions to install the required software.

Chapter 2

Governing equations

In this chapter we present the equations that we have used to model the free-flow and the porous-medium flow. For the free-flow we start considering the incompressible Navier-Stokes equations to simulate laminar flows, then we move to the Reynolds Averaged Navier-Stokes (RANS) equations with the k-ω model as a turbulence model. For the porous-medium flow our choice is the Forchheimer's law, which is an extension of the more common Darcy's law to higher Reynolds numbers.

2.1 Free-flow

2.1.1 Navier-Stokes equations

The Navier-Stokes equations describe the motion of a Newtonian viscous fluid, defining a relation between the following physical quantities:

- ϱ, the density of the fluid [kg/m^3],
- $\mathbf{v} = [u, v, w]^{\mathrm{T}}$, the velocity vector [m/s],
- e, the specific total energy [J/kg].

They can be derived starting from the general principles of conservation of mass:

$$\frac{d}{dt}\int_V \varrho \, dV = 0, \tag{2.1}$$

the second Newton's law:

$$\frac{d}{dt}\int_V \varrho \mathbf{v} \, dV = \int_V \varrho \mathbf{b} \, dV + \int_{\partial V} \boldsymbol{\sigma} \mathbf{n} \, dA \tag{2.2}$$

and the first law of thermodynamics:

$$\frac{d}{dt}\int_V e\, dV = \dot{Q} + \dot{W} \tag{2.3}$$

for any material volume V. In equation (2.2) vector $\mathbf{b}$ represents possible external volume forces per unit of mass, for example the gravity $\mathbf{g}$, $\boldsymbol{\sigma}$ is the Cauchy stress tensor and $\mathbf{n}$ is the outward unit vector normal to the surface ∂V of V. In equation (2.3) $\dot{Q}$ is the net rate of heat added to the fluid and $\dot{W}$ is the net rate of work done on the fluid.

For viscous fluids we can identify two contributions in the Cauchy stress tensor:

$$\boldsymbol{\sigma} = -p\mathbf{I} + \boldsymbol{\tau}, \tag{2.4}$$

$-p\mathbf{I}$ is a contribution due to pressure, while $\boldsymbol{\tau}$ is the viscous stress tensor, for which the constitutive relation of Newtonian fluids is used:

$$\boldsymbol{\tau} = 2\mu\mathbf{S} + \lambda(\nabla\cdot\mathbf{v})\mathbf{I}, \tag{2.5}$$

where μ is the dynamic viscosity [Pa s], λ is a dilatation factor and $\mathbf{S}$ is the symmetric strain rate tensor:

$$\mathbf{S} = \frac{\nabla\mathbf{v} + \nabla\mathbf{v}^{\mathrm{T}}}{2}.$$

Moreover we define the kinematic viscosity [m^2/s] as

$$\nu = \frac{\mu}{\varrho}. \tag{2.6}$$

We want to deal with incompressible fluids with a constant density that is not related to the pressure through a state equation. Thus, the energy equation can be decoupled from the others and we can exclude it from the system. Notice that, with this assumption, p is no longer the thermodynamic pressure. Using these assumptions from the balance equations (2.1) and (2.2) we obtain the incompressible Navier-Stokes equations:

$$\nabla\cdot\mathbf{v} = 0 \tag{2.7}$$

$$\frac{\partial\mathbf{v}}{\partial t} + \nabla\cdot(\mathbf{v}\mathbf{v}^{\mathrm{T}}) - \nabla\cdot(\nu\nabla\mathbf{v}) + \frac{1}{\varrho}\nabla p - \mathbf{g} = \mathbf{0} \tag{2.8}$$

All the computations needed to obtain these equations can be found in any book of fluid mechanics, for example in [VM07]. The continuity equation reduces to an incompressibility constraint (2.7) that is enforced in the momentum equation through the pressure that acts as a Lagrangian multiplier. The second term of the momentum equation (2.8) is non-linear and represents the advection that the velocity enforces on itself, while the third one is a diffusive term that express the action of the viscosity.

Boundary conditions

When the equations (2.7) and (2.8) are solved in a bounded domain Ω_{ff}, suitable conditions have to be provided at the boundary $\partial\Omega_{\text{ff}}$, depending on the situation that we want to model. Common choices, adopted also in the test cases in Chapter 4, are the following:

- on inflow boundaries, Dirichlet conditions are imposed to the velocity:

$$\mathbf{v} = \mathbf{v}_{\text{in}}, \tag{2.9}$$

- on solid walls, homogeneous Dirichlet conditions are imposed to the velocity (also called no-slip conditions):

$$\mathbf{v} = \mathbf{0}, \tag{2.10}$$

- on outflow boundaries, natural boundary conditions are imposed, resulting in the following prescription for the stress :

$$\boldsymbol{\sigma}\mathbf{n} = -p\mathbf{n} + 2\mu\mathbf{S}\mathbf{n} = \varrho\mathbf{d}, \tag{2.11}$$

  where $\mathbf{n}$ is the outward unit vector normal to the surface. However outflow boundary conditions are usually located where the flow is almost unidirectional and the surface stresses are known, so, especially when using the finite volumes method, they are replaced by:

$$(\nabla\mathbf{v})\mathbf{n} = \mathbf{0}, \quad p = p_{\text{ext}}, \tag{2.12}$$

  thus fixing a a zero-gradient condition for the velocity and imposing a Dirichlet condition to the pressure (see [VM07]).

Moreover it is usually useful to take advantage of symmetries in the flow field, when they are known because of the domain and of the boundary conditions. For example, to model a flow in a channel, we can impose the following symmetry conditions along the centre of the domain and consider only half of it:

$$\nabla p \cdot \mathbf{n} = 0, \quad \nabla v_t \cdot \mathbf{n} = 0, \quad v_n = 0, \tag{2.13}$$

where v_t an v_n are the tangential and normal components of the velocity.

Reynolds number

If we consider the non-dimensional form of equation (2.8), scaling the lengths by a reference quantity L and the velocities by a reference quantity U, and neglecting gravity, we obtain

$$\frac{\partial \tilde{\mathbf{v}}}{\partial \tilde{t}} + \tilde{\nabla} \cdot (\tilde{\mathbf{v}}\tilde{\mathbf{v}}^{\mathrm{T}}) - \tilde{\nabla} \cdot \left(\frac{1}{Re} \tilde{\nabla} \tilde{\mathbf{v}} \right) + \tilde{\nabla} \tilde{p} = 0, \tag{2.14}$$

where $\tilde{\cdot}$ denotes non-dimensional quantities. The non-dimensional number Re that multiplies the viscous term is the Reynolds number and it is defined as:

$$Re = \frac{UL}{\nu}. \tag{2.15}$$

This quantity plays an important role characterising the behaviour of the solution of the Navier-Stokes equations, since it expresses the ratio between the inertial forces and the viscous forces. This can be easily seen in equation (2.14) since, when $Re \gg 1$, the viscous term loses importance with respect to the advective one and vice versa.

If $Re < 1$ we have a creeping flow and generally the advection term can be neglected, reducing the Navier-Stokes equations to the Stokes equations, that are much simpler to analyse and to solve because they are linear. The assumption of creeping flow is common in porous-media models, as we will see in Section 2.2. If $Re > 1$ we have a laminar flow, which is characterized by a well-ordered viscosity-dominated motion, with adjacent layers of the fluid that slide with little interaction between each others. There exists a critical value Re_c such that when $Re > Re_c$ a transition from a laminar to a turbulent flow regime starts to take place, but this threshold value is very problem dependent as it is affected by the geometry of the domain and by the boundary conditions imposed.

2.1.2 Turbulence and RANS equations

Turbulence is characterized by an irregular, chaotic and intermittent behaviour, that shows space and time fluctuations of the physical quantities related to the flow, as we can see in Figure 2.1. Due to this complexity, turbulence is usually studied with a statistical approach, relying on the theory developed by Kolmogorov in 1941 [Kol41]. A complete description of turbulence can be found for example in [Pop06], [Wil06] or [Dav04].

The first thing that can be observed in a turbulent flow is the presence of many three-dimensional eddies, that enhance the dispersive and mixing properties of the flow. They cover a wide spectrum of length scales, in which

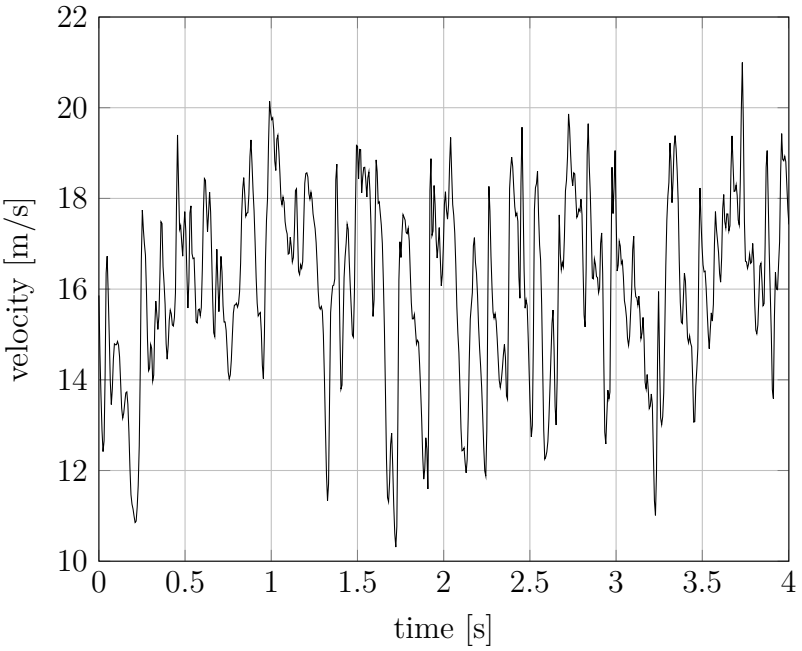

Figure 2.1: Example of fluctuating velocity in a turbulent flow.

we can identify three distinct bands; in the first one, corresponding to large scales, comparable to the size of the domain, there is an injection of kinetic energy and eddies are generated. Then, there is an intermediate band in which convection is dominant and eddies shrink without a significant loss of energy. The third band corresponds to the smallest scales at which eddies are present. In fact, once they reach a certain size, the effect of viscosity starts to be relevant and the kinetic energy of the eddies is dissipated into internal thermal energy. So, globally, energy is transferred from the large scales to the small ones, until it gets dissipated; this process is known as the Richardson energy cascade (Figure 2.2).

Simulation of turbulent flows

From the Kolmogorov theory we can obtain useful information for the simulation of turbulent flows. Let us indicate with l_0 the length scale at which eddies are generated and with l_D the length scale at which they dissipate. Then, according to [Kol41], it can be obtained that

$$\frac{l_0}{l_D} \sim Re^{\frac{3}{4}}. \tag{2.16}$$

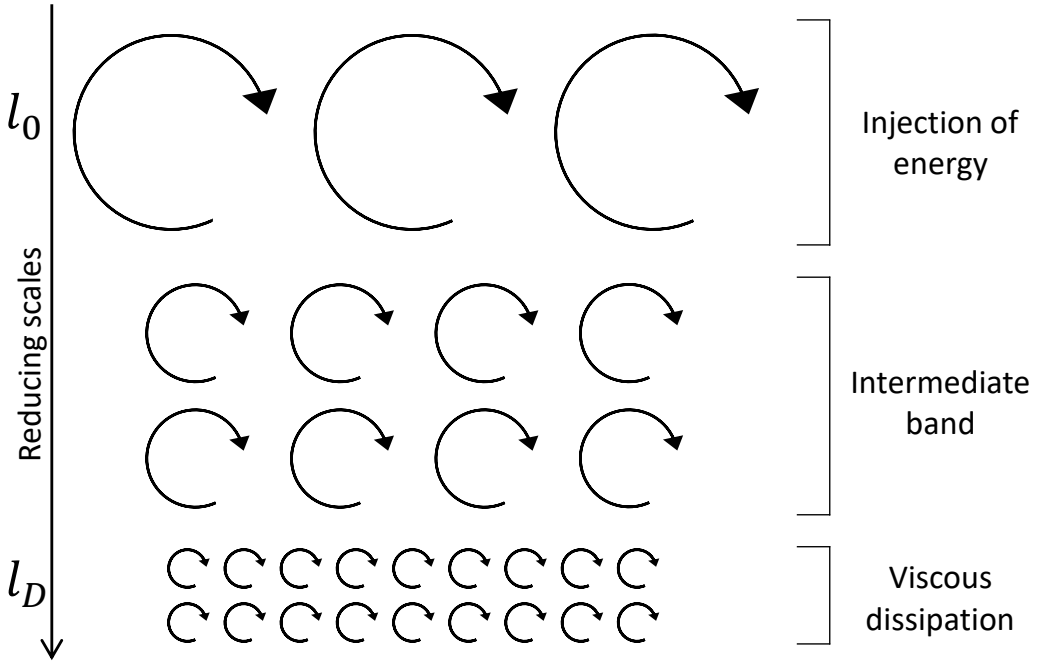

Figure 2.2: Scheme of the Richardson energy cascade.

If we want to perform a reliable simulation of a turbulent flow using the Navier-Stokes equations (2.7)-(2.8), we need a grid with a spatial resolution sufficient to resolve all the eddies until the smallest ones, otherwise we would neglect important information about the viscous dissipation of these structures. Assuming to have a domain of size comparable to l_0, then we need a size of the cells of the grid not bigger than l_D and from (2.16) we deduce that we need at least $Re^{\frac{3}{4}}$ cells in each of the three dimensions of the domain. Because of the fluctuating behaviour of turbulence, we always have to perform unsteady simulations, so let us denote with t_0 the characteristic time of evolution of the eddies at l_0 and with t_D the characteristic time of evolution of the eddies at l_D. Again from [Kol41] we have that

$$\frac{t_0}{t_D} \sim Re^{\frac{1}{2}}. \tag{2.17}$$

The total number of "operations" N needed in a simulation can be considered proportional to:

$$N \sim N_t N_{\text{elem}}, \tag{2.18}$$

where N_t is the total number of time-steps and N_{elem} is the total number of elements in the grid and. From the previous relations we obtain:

$$N \sim N_t N_{\text{elem}} \sim \frac{t_0}{t_D}\left(\frac{l_0}{l_D}\right)^3 = Re^{\frac{11}{4}}. \tag{2.19}$$

Reynolds numbers can be easily of the order of 10^6 or greater in common situations, so even with this rough estimate we can see that the computational effort for these simulations, called Direct Numerical Simulations (DNS), is usually very high. Moreover such a detailed information that we would obtain usually goes beyond the real need in many applications, therefore other approaches have been developed in order to solve this issue, such as the one proposed by the RANS equations.

RANS equations

The Reynolds Averaged Navier-Stokes (RANS) equations focus on the mean flow field, avoiding to simulate all the eddies but without forgetting to take into account their effect. In engineering applications this is the most common way to simulate turbulent flows because it is cheap and usually the mean information is enough for many applications, but we must not forget that the obtained result is not the flow field as it appears in reality. In case that more detail is needed, another approach is given by the Large Eddy Simulations (LES), that consist in applying a filter to the Navier-Stokes equation that let us resolve the eddies until a certain threshold size.

The first step towards the RANS equations is to decompose each instantaneous quantity in the sum of a mean value $\bar{\cdot}$ and a fluctuation $\cdot'$:

$$\mathbf{v} = \bar{\mathbf{v}} + \mathbf{v}', \quad p = \bar{p} + p'. \tag{2.20}$$

According to [VM07] the mean value can be obtained with a time average over a long time interval for steady flows, while it is obtained with an ensemble average for unsteady flows, so that by definition

$$\overline{\mathbf{v}'} = \mathbf{0}, \quad \overline{p'} = 0. \tag{2.21}$$

We want equations for the mean velocity $\bar{\mathbf{v}}$ and the mean pressure $\bar{p}$, so we apply the average operation to the Navier-Stokes equations (2.7)-(2.8) and we obtain:

$$\nabla \cdot \bar{\mathbf{v}} = 0 \tag{2.22}$$

$$\frac{\partial \bar{\mathbf{v}}}{\partial t} + \nabla \cdot (\bar{\mathbf{v}}\bar{\mathbf{v}}^{\mathrm{T}}) + \nabla \cdot (\overline{\mathbf{v}'\mathbf{v}'^{\mathrm{T}}}) - \nabla \cdot (\nu \nabla \bar{\mathbf{v}}) + \frac{1}{\varrho}\nabla \bar{p} - \mathbf{g} = \mathbf{0} \tag{2.23}$$

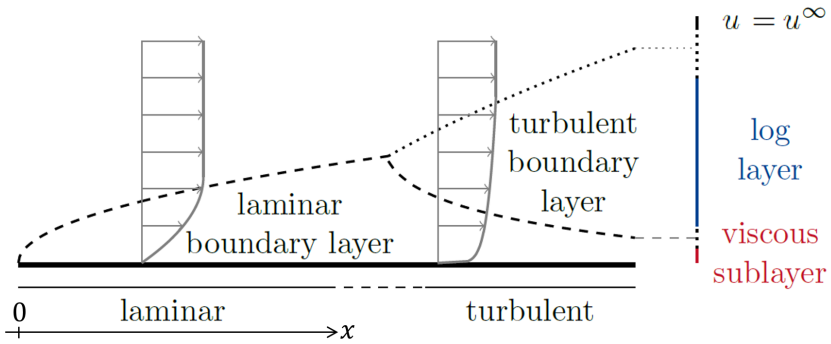

Figure 2.3: Scheme of the evolution of a boundary layer along a flat plate. The origin of the x-axis is set at the stagnation point. Figure source: [Fet18].

For what concerns the continuity equation, the average commutes with the divergence operator, so we obtain that also the mean velocity has to fulfil the incompressibility constraint (2.22). Averaging the momentum equation all the terms behave analogously, except the non linear term which produces an extra contribution:

$$\overline{\mathbf{v}\mathbf{v}^{\mathrm{T}}} = \overline{(\bar{\mathbf{v}} + \mathbf{v}')(\bar{\mathbf{v}} + \mathbf{v}')^{\mathrm{T}}} = \bar{\mathbf{v}}\bar{\mathbf{v}}^{\mathrm{T}} + \overline{\mathbf{v}'\mathbf{v}'^{\mathrm{T}}}. \tag{2.24}$$

The new term

$$\boldsymbol{\tau}_R = -\varrho\overline{\mathbf{v}'\mathbf{v}'^{\mathrm{T}}} \tag{2.25}$$

is called Reynolds stress tensor. Mathematically, it expresses the correlation between the components of the instantaneous velocity field, while physically it represents the diffusive effect of turbulence (see [VM07]).

Boundary layers

When a fluid flows along a boundary, such as a solid wall, the region near the the wall is called boundary layer and it is important because the viscosity plays a major role there, even in turbulent conditions. Independently of the flow regime, the no-slip condition imposes a null velocity at the wall and thus a gradient orthogonal to the flow direction. The thickness of the boundary layer δ is conventionally defined as the position where the velocity reaches the 99% of its maximum value and different values are observed for different kinds of flow. See for example [SG17], [Pop06] or [Dav04] for a complete description.

Let us consider a flow over a flat plate as depicted in Figure 2.3: when the flow reaches the plate a laminar boundary layer starts to develop. Initially a laminar regime holds and the layer is characterized by a moderate gradient of

the velocity profile at the wall. After a certain distance a turbulent boundary layer starts to grow: it is thicker but the gradient of the velocity at the wall is stronger. We can define a Reynolds number based on the distance from the beginning of the plate and another one based on the boundary layer thickness, respectively

$$Re_x = \frac{u^\infty x}{\nu}, \quad Re_\delta = \frac{u^\infty \delta}{\nu}, \tag{2.26}$$

where u^∞ is the maximum velocity far from the wall.

For the laminar boundary layer the profile can be computed analytically through the Blasius equation, which is obtained using dimensional arguments (see [SG17]). The thickness grows as the square root x, i.e. the distance from the stagnation point:

$$\delta(x) = 4.9\frac{x}{\sqrt{Re_x}} = 4.91\sqrt{\frac{x\nu}{u^\infty}}. \tag{2.27}$$

When Re_δ is higher than a certain threshold, the turbulent boundary layer begins, but in this case the velocity profile can be expressed only through some empirical laws. In order to do that it is useful to define a non-dimensional wall coordinate:

$$y^+ = \frac{u_* y}{\nu}, \quad u_* = \sqrt{\frac{\tau_w}{\varrho}}, \tag{2.28}$$

where τ_w is the shear stress at the wall. In the boundary layer four different regions can be identified:

- near the wall, for approximately $y^+ < 5$, a small laminar viscous sub-layer is always present and it cannot be neglected. In this area the viscous stresses are dominant over the Reynolds stresses and the velocity profile can be approximated with a linear relation:

$$u = u_* y^+, \tag{2.29}$$

- after that there is a buffer layer in which the viscous and Reynolds stresses are comparable,

- then, approximately in the region $30 < y^+ < 150$, there is the so called log-layer, in which the velocity profile can be approximated with a logarithmic function:

$$u = u_*\left(\frac{1}{\kappa}\log y_+ + A\right), \quad \kappa = 0.41, \quad A = 5.5, \tag{2.30}$$

  where κ is the von Kármán constant,

- at last there is an external region, in which the behaviour depends on the external flow field.

Be aware that the numbers given above as bounds for y^+ are not universal but are very problem-dependent.

Turbulence models

The quantity $\boldsymbol{\tau}_R$ is a symmetric tensor with $dim \times dim$ entries, so in three dimensions we have 6 new unknowns that need to be modelled in order to close the problem, this procedure is known as turbulence modelling. In 1877 Boussinesq [Bou77] suggested that $\boldsymbol{\tau}_R$ could be similar to the viscous stress tensor, thus expressed as

$$\boldsymbol{\tau}_R = 2\mu_t \bar{\mathbf{S}} - \frac{2}{3}\varrho k \mathbf{I}. \tag{2.31}$$

The first term has the same form of $\boldsymbol{\tau}$ if we consider the mean velocity field, the only difference is that the dynamic viscosity μ is substituted by a turbulent viscosity μ_t [Pa s]. The second term is needed to model the isotropic part of $\boldsymbol{\tau}_R$ correctly:

$$tr(\boldsymbol{\tau}_R) = -tr(\varrho\overline{\mathbf{v}'\mathbf{v}'^{\mathrm{T}}}) = -\varrho\sum_{i=1}^{dim}\overline{(v_i')^2} = -2\varrho k, \tag{2.32}$$

where k is the turbulent kinetic energy defined as

$$k = \frac{1}{2}\sum_{i=1}^{dim}\overline{(v_i')^2}, \tag{2.33}$$

while exploiting equation (2.22) we get

$$tr(2\mu_t\bar{\mathbf{S}}) = 2\mu_t\sum_{i=1}^{dim}\frac{\partial\bar{v}_i}{\partial x_i} = 2\mu_t(\nabla\cdot\bar{\mathbf{v}}) = 0. \tag{2.34}$$

With this hypothesis μ_t and k are the only unknowns left and the momentum equation (2.23) becomes:

$$\frac{\partial\bar{\mathbf{v}}}{\partial t} + \nabla\cdot(\bar{\mathbf{v}}\bar{\mathbf{v}}^{\mathrm{T}}) - \nabla\cdot(\nu_{\mathrm{eff}}\nabla\bar{\mathbf{v}}) + \frac{1}{\varrho}\nabla(\bar{p} + \frac{2}{3}\varrho k) - \mathbf{g} = \mathbf{0}, \tag{2.35}$$

where we have introduced an effective kinematic viscosity

$$\nu_{\mathrm{eff}} = \nu + \nu_t, \quad \nu_t = \frac{\mu_t}{\varrho}. \tag{2.36}$$

Since for incompressible fluids we have removed the thermodynamic relation between ϱ and p, we can consider as unknown a generalized pressure p_{gen} such that:

$$p_{\text{gen}} = \bar{p} + \frac{2}{3}\varrho k, \tag{2.37}$$

reducing the unknowns to ν_t alone, which can be estimated using different turbulence models.

The idea of the Boussinesq hypothesis (2.31) comes partially from an analogy between the motion of the turbulent structures and the molecular motion, but there are cases in which it can be shown that this hypothesis leads to poor results (see [Pop06]). There exist also turbulence models called Reynolds stress equations models (RSM) that do not use it and try to find equations for all the entries of the Reynolds stress tensor, but in this way a large set of equations is obtained and consequently the required computational effort increases. See [Pop06] or [VM07] for more information.

From now, on the over-bar used to denote averaged quantities will be neglected in order to simplify the notation.

Zero-equations models

The simplest turbulence models are called zero-equations models or algebraic models because they compute the turbulent viscosity using an algebraic relation that exploits geometrical quantities, so they do not introduce any additional PDE to the problem. Due to their simplicity they were used in the past years when the computational resources were limited, but they have intrinsic weak points and they can be applied only in special simple situations.

An important example is Prandtl's *mixing length* model [Pra25]. It is useful with two-dimensional flows when the mean velocity field has a dominant direction and the gradient in the longitudinal direction is negligible with respect to that in the orthogonal direction. Let us assume that u is the main component of the velocity and that the flow is bounded by a wall at $y = 0$. From dimensional considerations it can be assumed that

$$\nu_t = l_{\text{mix}} v_{\text{mix}}, \tag{2.38}$$

where l_{mix} and v_{mix} are a characteristic length scale and a velocity scale of turbulence. Then, it is reasonable to choose

$$v_{\text{mix}} = l_{\text{mix}} \left| \frac{\partial u}{\partial y} \right|, \tag{2.39}$$

because the shear stress in the mean flow gives its contribution to the turbulent mixing of the largest eddies. At last, l_{mix} is chosen from empirical

considerations derived from the boundary layer theory previously described. For example,

$$l_{\text{mix}} = \kappa y, \tag{2.40}$$

in the original version, or

$$l_{\text{mix}} = \kappa y[1 - exp(y^+/26)], \tag{2.41}$$

using a correction proposed by Van Driest [Van56] that dampens ν_t for $y \to 0$.

k-ε model

Two-equation models involve the solution of two additional PDEs and the k-ε is probably the most famous one in this category. The key contribution to this model was given by Launder and Sharma [LS74]. It is based on the assumption that the turbulent viscosity ν_t could be correctly determined through the turbulent kinetic energy k and its dissipation rate ε. Considering the dimension units, the relation must be

$$\nu_t = C_\mu \frac{k^2}{\varepsilon}, \tag{2.42}$$

where C_μ is a non-dimensional constant and ε is defined as

$$\varepsilon = 2\nu\overline{\mathbf{S}' \cdot \mathbf{S}'}, \quad \mathbf{S}' = \frac{\nabla\mathbf{v}' + (\nabla\mathbf{v}')^{\mathrm{T}}}{2}. \tag{2.43}$$

Starting from the momentum equation of the Navier-Stokes model (2.8) and from the decomposition in mean value plus fluctuation (2.20), we derive an equation for k:

$$\frac{\partial k}{\partial t} + \nabla \cdot (k\mathbf{v}) - \nabla \cdot \left[\left(\nu + \frac{\nu_t}{\sigma_k}\right)\nabla k\right] - 2\nu_t \mathbf{S} \cdot \mathbf{S} + \varepsilon = 0, \tag{2.44}$$

where σ_k is a non-dimensional constant. In a similar way we could derive an evolution equation for ε, but it would contain too many terms difficult to model and to measure, so an empirical equation built in analogy with the one for k is used instead:

$$\frac{\partial \varepsilon}{\partial t} + \nabla \cdot (\varepsilon\mathbf{v}) - \nabla \cdot \left[\left(\nu + \frac{\nu_t}{\sigma_\varepsilon}\right)\nabla \varepsilon\right] - C_{\varepsilon_1}\frac{\varepsilon}{k}2\nu_t \mathbf{S} \cdot \mathbf{S} + C_{\varepsilon_2}\frac{\varepsilon^2}{k} = 0. \tag{2.45}$$

The standard model sets the following constants (see [VM07]):

$$C_\mu = 0.09, \quad \sigma_k = 1, \quad \sigma_\varepsilon = 1.3, \quad C_{\varepsilon_1} = 1.44, \quad C_{\varepsilon_2} = 1.92. \tag{2.46}$$

This model behaves best for confined flows and high Reynolds number, where the Reynolds stresses are dominant. Near the wall this assumption fails, so it is common to use a wall function such as the one given by the boundary layer theory (2.30) in order to compute the velocities at the cells near the wall. This can be done easily for flat walls and it brings also computational advantages, because we can avoid to have very small cells near the wall to resolve the viscous sublayer.

Over the years, many variants of this model have been developed, for example the *RNG* k-ε model, which is derived with a different procedure with the purpose of improving the equation for ε, or the *low-Re* k-ε model, which adds extra terms in order to correctly model the behaviour near the wall. See [VM07] for more details.

k-ω model

The k-ω model is another two-equations model that uses a specific dissipation rate ω instead of the dissipation rate ε. It was originally proposed by Kolmogorov [Kol42] and subsequently refined many times by Wilcox [Wil08].

The equation for the turbulent kinetic energy is analogous to the one used in the k-ε model:

$$\frac{\partial k}{\partial t} + \nabla \cdot (k\mathbf{v}) - \nabla \cdot \left[\left(\nu + \sigma^* \frac{k}{\omega} \right) \nabla k \right] - P + \beta^* k\omega = 0, \tag{2.47}$$

with the production term P that can be limited in the following way:

$$P = \min\{2\nu_t \mathbf{S} \cdot \mathbf{S}, 20\beta^* k\omega\}. \tag{2.48}$$

The equation for ω is empirical and driven by physical considerations as it was the equation (2.45) for ε. It reads:

$$\frac{\partial \omega}{\partial t} + \nabla \cdot (\omega \mathbf{v}) - \nabla \cdot \left[\left(\nu + \sigma \frac{k}{\omega} \right) \nabla \omega \right] - \alpha \frac{\omega}{k} 2\nu_t \mathbf{S} \cdot \mathbf{S} - \frac{\sigma_d}{\omega} \nabla k \cdot \nabla \omega + \beta \omega^2 = 0. \tag{2.49}$$

The term

$$\frac{\sigma_d}{\omega} \nabla k \cdot \nabla \omega \tag{2.50}$$

is a new addition with respect to (2.45). It is related to cross-diffusion and its activation depends on the direction of the gradients of k and ω:

$$\sigma_d = \begin{cases} 0 & \text{if } \nabla k \cdot \nabla \omega \leq 0 \\ \sigma_{do} & \text{if } \nabla k \cdot \nabla \omega > 0 \end{cases}, \quad \sigma_{do} = \frac{1}{8}. \tag{2.51}$$

The turbulent viscosity ν_t is obtained as

$$\nu_t = \frac{k}{\tilde{\omega}}, \quad \tilde{\omega} = \max\left\{\omega, C_{\text{lim}}\sqrt{2\frac{\mathbf{S}\cdot\mathbf{S}}{\beta^*}}\right\}. \tag{2.52}$$

The model is closed with the following empirical coefficients:

$$\beta^* = \frac{9}{100}, \quad \sigma^* = \frac{3}{5}, \quad \alpha = \frac{13}{25}, \quad \beta = \frac{177}{2500}, \quad \sigma = \frac{1}{2}, \quad C_{\text{lim}} = \frac{7}{8}. \tag{2.53}$$

The interpretation of ω is not straight-forward: originally it was defined by Kolmogorov as "the rate of dissipation of energy in unit volume and time", therefore defined as

$$\omega = \frac{k}{\varepsilon}. \tag{2.54}$$

Other contributors to the development of this model have referred to it as the the root mean square (RMS) of the fluctuating vorticity, i.e.

$$\omega = \sqrt{\overline{(\boldsymbol{\omega}')^2}}, \quad \boldsymbol{\omega} = \nabla \times \mathbf{v}. \tag{2.55}$$

In this case, ω^2 is the double of the *enstrophy*, which is a quantity associated to the energy related to vorticity.

This model has shown good results also near boundaries, so it does not require any wall correction. For our purposes it is the most appropriate choice because we would like to have non-flat boundaries, so employing a wall law would be cumbersome, if not impossible. Moreover, the values near the boundary are very important in our tests, because they influence the exchange processes across the interface between free-flow and porous-medium flow.

As boundary conditions, we have:

- on inflow boundaries, Dirichlet conditions are set both for k and ω. According to [ANS09], the following formulas can be used:

$$k = \frac{3}{2}(\|\mathbf{v}_{\text{in}}\|I)^2, \quad \omega = \frac{100k^{1/2}}{7C_\mu^{1/4}L}, \tag{2.56}$$

  where $\mathbf{v}_{\text{in}}$ is the inflow velocity and I is a non-dimensional quantity called turbulence intensity that could be estimated as

$$I = \frac{0.16}{Re^{1/8}}. \tag{2.57}$$

  Here, $C_\mu = 0.09$ and L is a characteristic size of the domain,

- on solid walls, $k = 0$, while, according to [Wil06], the following asymptotic behaviour for ω is used:

$$\omega \to \frac{6\nu}{\beta d^2} \quad \text{as} \quad d \to 0, \tag{2.58}$$

  where d is the distance from the nearest wall,

- on outflow and symmetry boundaries, a zero-gradient condition is assumed:

$$\nabla k \cdot \mathbf{n} = 0, \quad \nabla \omega \cdot \mathbf{n} = 0. \tag{2.59}$$

2.2 Porous-medium flow

According to [NB17] a porous-medium is "a material consisting of a solid matrix with an interconnected void". The void spaces are called *pores* and they allow a fluid to flow through the material. We consider the solid matrix to be fixed, neglecting the fluid-structure interaction. Examples of porous-media are sand, wood, soil, sandstone and ceramics.

To simulate flow through a porous medium theoretically we could use the standard fluid dynamics equations at the pore scale, but this approach is extremely expensive because of the strict spatial and temporal requirement of a direct numerical simulation in such a complex domain. Moreover, from the point of view of applications, the knowledge of the model variables at such level of detail is often useless, considering also the fact that at this scale they are very irregular and, also, it is hard to get measurements of them. What is usually done is to upscale the description of the flow by considering averaged quantities within a Representative Elementary volume (REV), thus considering the porous-medium as a continuum at a larger scale. In this way we lose the information at the pore scale, but we obtain results that are comparable to experimental measurements. The upscaling procedure can be done by rigorous homogenization techniques [All89] or by formal averaging [Wit99]. We briefly describe the latter approach.

Given a domain Ω_{pm} occupied by the porous-medium, we consider at every point $\mathbf{x} \in \Omega_{\text{pm}}$ a ball $B_r(\mathbf{x})$ of radius r, that will be the REV. Starting from a function f defined at the pore scale we compute its average $\hat{f}$:

$$\hat{f}(\mathbf{x}) = \frac{1}{|B_r(\mathbf{x})|} \int_{B_r(\mathbf{x})} f(\mathbf{y}) d\mathbf{y}, \quad \forall \mathbf{x} \in \Omega_{\text{pm}}. \tag{2.60}$$

The radius r, and thus the dimension of the REVs, should be chosen such that

$$l \ll r \ll L, \tag{2.61}$$

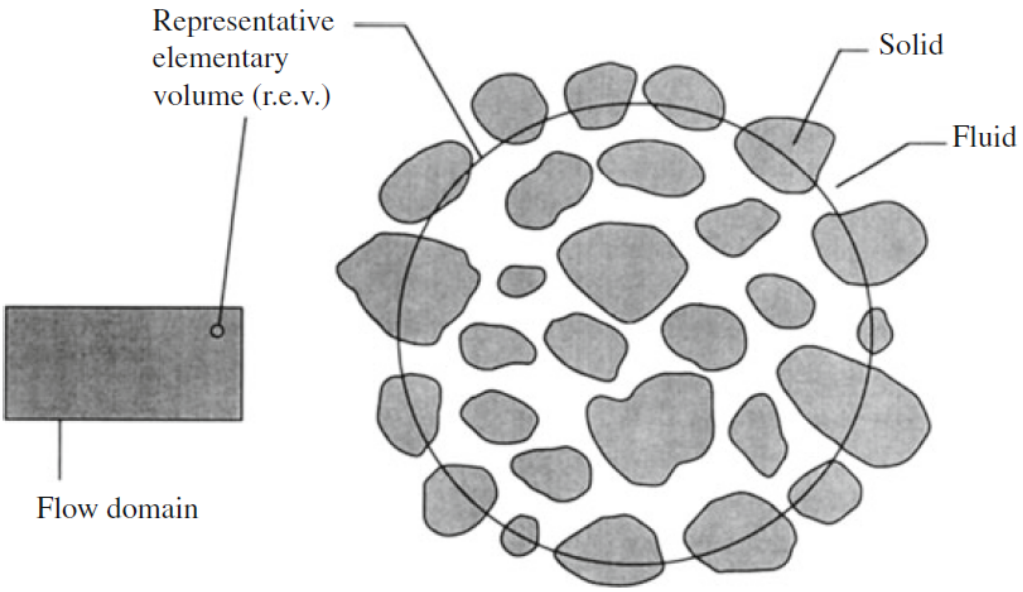

Figure 2.4: An example of a REV in a porous-medium. Comparison of its size with the one of the pores and the one of Ω_{pm}. Figure source: [NB17].

where l is the pore scale size and L is the macro scale size, as for example in Figure 2.4. In such a way the high frequency variations of microscopic properties are averaged out at the REV scale, but the low frequency variations of macroscopic properties are kept (see [Hel97]).

Let us define the *porosity* of the porous-medium as

$$\varphi(\mathbf{x}) = \frac{1}{|B_r(\mathbf{x})|} \int_{B_r(\mathbf{x})} \chi(\mathbf{y}) d\mathbf{y}, \tag{2.62}$$

where $\chi(\mathbf{x})$ is the characteristic function of the void space:

$$\chi(\mathbf{x}) = \begin{cases} 1 & \text{if } \mathbf{x} \text{ is void} \\ 0 & \text{if } \mathbf{x} \text{ is not void} \end{cases}, \quad \forall \mathbf{x} \in \Omega_{\text{pm}}. \tag{2.63}$$

For simplicity we will assume to have porous-media with constant porosity. In natural materials usually φ is not greater then 0.6, but for some artificial materials, such as metallic foams, φ could be almost 1.

When two or more fluids flow through the pores, for example liquid water and gaseous air, we have a *multiphase* flow system. According to [Hel97], the term *phase* denotes each of the distinct fluids that are separated by a sharp interface, across which discontinuities in fluid properties exist. A phase can be a pure substance or a mixture of substances with uniform

chemical structure and physical properties, so a phase is a homogeneous system. Different phases, instead, can present different physical properties and thermodynamic variables. In general, multiple liquid phases can coexist, for example water and oil, but only one gaseous phase is possible because gases are always miscible. Each chemical substance a phase is made of is called *component*. Each component can be present in different phases in different physical states, for example water in a liquid phase and water vapour is a gaseous phase, and phases may exchange components by phase transitions processes, like vaporization or condensation. In the following, we will limit our description and test cases to single-phase, single-component flows.

2.2.1 Continuity equation

The governing equations for a porous-medium at the REV scale can be computed from the standard equations for the fluid through the application of volume averaging techniques (see [Wit99]).

We obtain the following continuity equation:

$$\varphi \frac{\partial \varrho}{\partial t} + \nabla \cdot (\varrho \mathbf{v}) = 0, \tag{2.64}$$

where ϱ denotes the density of the fluid. $\mathbf{v}$ is the velocity obtained averaging over a REV containing both fluid and solid and it can be called *Darcy* velocity or *seepage* velocity. It should not be confused with the *intrinsic* velocity $\mathbf{V}$ that we would obtain averaging over a REV containing only fluid, as they are related by:

$$\mathbf{v} = \varphi \mathbf{V}. \tag{2.65}$$

If we assume that the fluid is incompressible, then the continuity equation reduces to

$$\nabla \cdot \mathbf{v} = 0. \tag{2.66}$$

2.2.2 Momentum equation

According to the assumptions, we can obtain different laws.

Darcy's law

For the momentum equation the most common choice is the Darcy's law:

$$\mathbf{v} = -\frac{1}{\mu}\mathbf{K}(\nabla p - \varrho \mathbf{g}), \tag{2.67}$$

where $\mathbf{K}$ [m^2] is the permeability tensor of the porous-medium; it is symmetric and positive-definite and it can be simplified to a scalar for isotropic porous-media. This equation holds for creeping flows, with $Re < 1$, for which inertial effect can be neglected.

It was first obtained experimentally by Henry Darcy in 1856, who discovered a proportionality between the flow rate and the pressure drop across a uniform porous-medium. After that there have been many attempts to derive it analytically, starting from the Navier-Stokes equations and using volume averaging techniques with different assumptions made, see for example [Wit86]. Moreover it can be obtained through a homogenization procedure if the porous-medium is periodic (see [Hol95]).

The permeability is a quantity that depends only on the geometry of the porous medium and not on the flow, typical values range from $10^{-7}\,m^2$ of gravel to $10^{-16}\,m^2$ of limestone. There are models to compute it in the case of simple geometries, for example through the Carman-Kozeny equation (see [NB17]).

Forchheimer's law

There exist many generalizations of Darcy's law, for example to multiphase and multicomponent flows, to non-Newtonian fluids or, as in this case, to higher Reynolds numbers. The extension that we are interested in is the so called Forchheimer's law [For01], that reads:

$$\mathbf{v} + C_F\sqrt{\mathbf{K}}\frac{\varrho}{\mu}|\mathbf{v}|\mathbf{v} = -\frac{1}{\mu}\mathbf{K}(\nabla p - \varrho\mathbf{g}), \tag{2.68}$$

where the second term is added to the Darcy's law in order to take into account any possible inertial effect. C_F is a non-dimensional coefficient which is here taken equal to 0.55, even if there exist many different corrections (see [NB17] and [Jam11]).

As reported by Nield and Bejan [NB17], the equation was originally proposed by Forchheimer in 1901, but the dependence on $\sqrt{\mathbf{K}}$ was later introduced by Ward [War64]. Withaker [Wit96] derived it with the volume averaging starting from the Navier-Stokes equations.

This equation holds when the flow in the porous-medium is laminar, but the drag from linear becomes quadratic because the contribution due to solid obstacles becomes comparable to the one due to friction. According to [NB17], the transition from a linear to a quadratic regime is smooth and takes place at

$$Re_{\mathrm{K}} \simeq 100, \tag{2.69}$$

where Re_{K} is a Reynolds number based on the square root of the permeability:

$$Re_{\mathrm{K}} = \frac{U\sqrt{\mathrm{K}}}{\nu}. \tag{2.70}$$

2.3 Coupling conditions

At the interface between the free-flow region and the porous-medium we have to impose suitable conditions in order to couple the two subdomains. Let us denote with Ω_{ff} the free-flow domain and with Ω_{pm} the porous-medium domain, then

$$\Gamma_{\mathrm{int}} = \overline{\Omega}_{\mathrm{ff}} \cap \overline{\Omega}_{\mathrm{pm}} \tag{2.71}$$

is the interface between them.

Following Mosthaf et al. [Mos+11], we would like to have conditions such that the interface could be as close as possible to local thermodynamic equilibrium. However, this cannot be rigorously achieved due to the different model concepts in the two subdomains. Since we are dealing with single-phase, single-component isothermal flows, we only have to impose the mechanical equilibrium, for which we need:

- the continuity of normal mass fluxes, that in our incompressible case reduces to the continuity of the normal component of the velocity:

$$[\mathbf{v}\cdot\mathbf{n}]_{\mathrm{ff}} = -[\mathbf{v}\cdot\mathbf{n}]_{\mathrm{pm}} \quad \text{on } \Gamma_{\mathrm{int}}, \tag{2.72}$$

  where the subscripts $_{\mathrm{ff}}$ and $_{\mathrm{pm}}$ denote that the quantities are evaluated in the free-flow or in the porous-medium subdomain. Notice that

$$\mathbf{n}_{\mathrm{ff}} = -\mathbf{n}_{\mathrm{pm}} \quad \text{on } \Gamma_{\mathrm{int}}, \tag{2.73}$$

- the continuity of normal stresses:

$$[(\varrho\mathbf{v}\mathbf{v}^{\mathrm{T}} - \mu_{\mathrm{eff}}\nabla\mathbf{v} + p\mathbf{I})\mathbf{n}]_{\mathrm{ff}} = -[p\mathbf{n}]_{\mathrm{pm}} \quad \text{on } \Gamma_{\mathrm{int}}, \tag{2.74}$$

  that may result in a jump of the pressure at the interface, although pressure is typically a continuous thermodynamic variable,

- a condition for the tangential component of the velocity in the free-flow and in particular we use the one proposed by Beavers and Joseph [BJ67]:

$$\left[\left(-\frac{\sqrt{\mathrm{K}}}{\alpha_{BJ}}(\nabla\mathbf{v})\mathbf{n}-\mathbf{v}\right)\cdot\mathbf{t}_i\right]_{\mathrm{ff}} = [\mathbf{v}\cdot\mathbf{t}_i]_{\mathrm{pm}}, \quad \forall i \in \{1,\dots,dim-1\}, \tag{2.75}$$

on Γ_{int}, where α_{BJ} is a non-dimensional coefficient that depends on properties of the permeable material and $\mathbf{t}_i,\ i \in \{1, \dots, dim-1\}$ is a basis of the plane tangential to the interface Γ_{int}. With this condition we allow a slip of the tangential component of the velocity and the more the porous-medium is permeable, the more slip is allowed.

We also employ the simplification introduced by Saffman [Saf71]:

$$[\mathbf{v} \cdot \mathbf{t}_i]_{\text{pm}} \simeq 0, \quad \forall i \in \{1, \dots, dim-1\}, \tag{2.76}$$

so we neglect the tangential velocity in the porous-medium since it is very small with respect to the one in the free-flow region, thus obtaining the Beavers-Joseph-Saffman (BJS) condition:

$$\left[\left(-\frac{\sqrt{\mathrm{K}}}{\alpha_{\text{BJ}}} (\nabla \mathbf{v}) \mathbf{n} - \mathbf{v} \right) \cdot \mathbf{t}_i \right]_{\text{ff}} = 0, \quad \forall i \in \{1, \dots, dim-1\}. \tag{2.77}$$

This condition can be derived also using homogenizations techniques (see [JM00] and [DQ09]).

Chapter 3

Numerical model

In this chapter we describe the methods that we have chosen to discretize the mathematical model. For the spatial discretization we use the finite volumes method, which allows to solve flow problems efficiently, guaranteeing the conservation of mass also locally. See [LeV02] for a general description. In the free-flow region, we discretize the equations using the staggered grid concept, while in the porous-medium we employ a cell-centred approach with a Two Point Flux Approximation (TPFA).

For the temporal discretization we use the implicit finite differences methods Backward Euler (BE) and Backward Differencing Formula of order 2 (BDF2).

3.1 Free-flow

3.1.1 Staggered grid discretization

The staggered grid discretization is characterized by the distinction between the degrees of freedom related to scalar primary variables and those related to vectorial primary variables. In saddle point problems, like the incompressible Navier-Stokes or RANS equations, if we locate all the primary variables, i.e. pressure, velocity and possibly the turbulent kinetic energy and its dissipation rate, at the same positions in the grid, spurious modes in the pressure solution may arise, leading to wrong results. In the context of finite volumes, a possible solution to this issue is to represent the variables in a *staggered* fashion, putting the degrees of freedom related to scalar variables, particularly the pressure, at the centre of the cells and those related to vectorial variables on the faces, aligned to the faces normal direction. Therefore, we obtain different control volumes, as we can see in Figure 3.1 for the case of

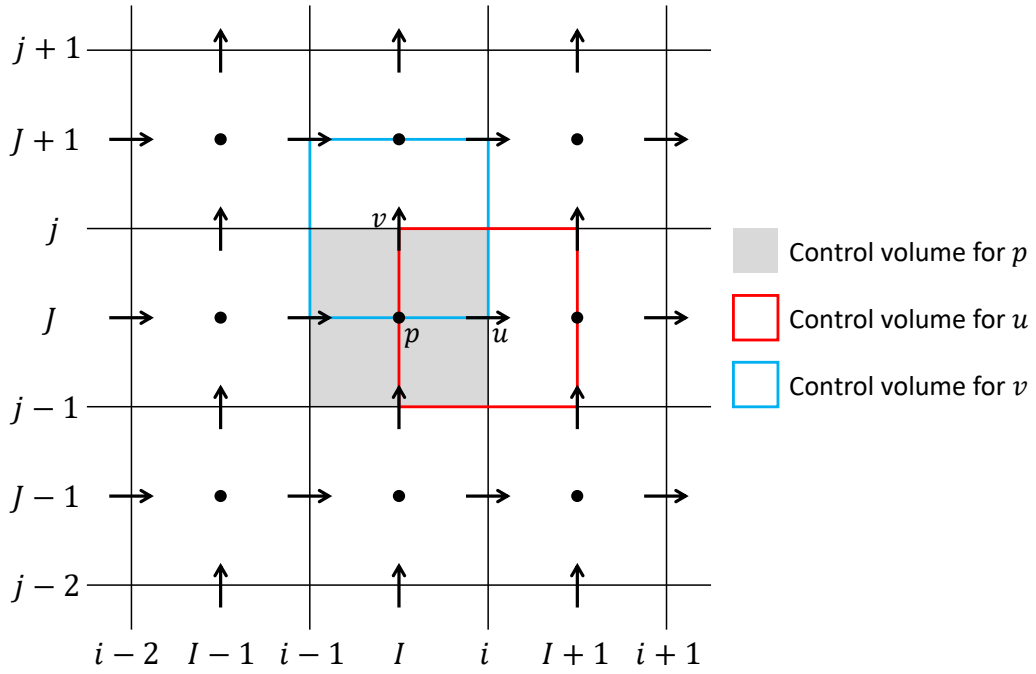

Figure 3.1: An example of a uniform staggered grid with the pressure degrees of freedom (dofs) stored at the centres of the cells and the velocity dofs stored on the faces. The different control volumes are highlighted. The indices in capital letters $\ldots, I-1, I, I+1, \ldots$ and $\ldots, J-1, J, J+1, \ldots$ refer to cells, thus to the position of cell-centred variables, while the indices in lower case letters $\ldots, i-1, i, i+1, \ldots$ and $\ldots, j-1, j, j+1, \ldots$ refer to faces, thus to the position of staggered variables.

the Navier-Stokes equations in a two-dimensional domain.

This approach is known also as Marker and Cell (MAC), as it was names in its first appearance in a paper by Harlow and Welch [HW65], within a finite differences framework. A more recent description can be found in [VM07].

Another advantage of this discretization method is that on the boundary we have naturally the degrees of freedom of the normal component of the velocity, so it is easier to impose boundary and interface conditions with respect to the case where all the degrees of freedom are stored at the cell centres.

For the sake of simplicity we focus our attention on the two-dimensional case, where the velocity vector is $\mathbf{v} = [u, v]^{\mathrm{T}}$.

Continuity equation

The continuity equation (2.22) is discretized using control volumes that coincide with the cells of the grid, thus it is treated is a cell-centred way. Since we are dealing with incompressible fluids, it does not involve the density and this makes its approximation simpler. We integrate over the "grey" control volume $V_p = [x_{i-1}, x_i] \times [y_{j-1}, y_j]$, according to Figure 3.1, and we apply the Gauss's divergence theorem:

$$\int_{V_p} \nabla \cdot \mathbf{v} \, dV = \int_{\partial V_p} \mathbf{v} \cdot \mathbf{n} \, dA = 0. \tag{3.1}$$

The integral over the boundary ∂V_p can be split over the four faces, that we identify with e_p (east), n_p (north), w_p (west), s_p (south):

$$\int_{\partial V_p} \mathbf{v} \cdot \mathbf{n} \, dA = \int_{e_p} u \, dA + \int_{n_p} v \, dA - \int_{w_p} u \, dA - \int_{s_p} v \, dA. \tag{3.2}$$

At this point we discretize the equation approximating the values of the velocity with the values at the centre of the faces, for example:

$$\int_{e_p} u \, dA \approx u_{i,J} |e_p|, \tag{3.3}$$

where $|e_p|$ denotes the measure of the face e_p. Thus we obtain

$$u_{i,J}|e_p| + v_{I,j}|n_p| - u_{i-1,J}|w_p| - v_{I,j-1}|s_p| = 0. \tag{3.4}$$

Momentum equation

The momentum equation (2.35) is discretized using the staggered control volumes. Let us consider the equation for the component u of the velocity:

$$\frac{\partial u}{\partial t} + \nabla \cdot (u\mathbf{v}) - \nabla \cdot (\nu_{\text{eff}} \nabla u) + \frac{1}{\varrho} \frac{\partial}{\partial x} \big(p + \varrho k\big) = 0. \tag{3.5}$$

Notice that, since we are considering a two-dimensional model, we have substituted the factor 2/3 with a 1 in front of ϱk, because it comes from the requirement (2.32).

We integrate it over the "red" control volume $V_u = [x_I, x_{I+1}] \times [y_{j-1}, y_j]$, according to Figure 3.1, and apply the Gauss's divergence theorem:

$$\begin{aligned} \int_{V_u} \left[\frac{\partial u}{\partial t} + \nabla \cdot (u\mathbf{v}) - \nabla \cdot (\nu_{\text{eff}} \nabla u) + \frac{1}{\varrho} \frac{\partial}{\partial x} \big(p + \varrho k\big) \right] dV = \\ = \frac{d}{dt} \int_{V_u} u \, dV + \int_{\partial V_u} u(\mathbf{v} \cdot \mathbf{n}) \, dA - \int_{\partial V_u} \nu_{\text{eff}} (\nabla u \cdot \mathbf{n}) \, dA + \\ + \frac{1}{\varrho} \int_{\partial V_u} (p + \varrho k) n_x \, dA = 0, \end{aligned} \tag{3.6}$$

where n_x is the component in the x direction of the outward unit normal $\mathbf{n}$. Let us identify again the four faces of ∂V_u with e_u (east), n_u (north), w_u (west), s_u (south), so that

$$\partial V_u = e_u \cap n_u \cap w_u \cap s_u. \tag{3.7}$$

In the equation (3.6) there are four terms of different nature, let us consider each of them separately, starting from the simplest one:

- in the storage term we approximate the velocity with the value at the centre of the control volume:

$$\frac{d}{dt}\int_{V_u} u \, dV \approx \frac{du_{i,J}}{dt}|V_u|. \tag{3.8}$$

- in the pressure term the contributions from the faces n_u and s_u are null because $n_x = 0$ on them, so

$$\int_{\partial V_u} (p + \varrho k) n_x \, dA = \int_{e_u} (p + \varrho k) \, dA - \int_{w_u} (p + \varrho k) \, dA. \tag{3.9}$$

  Then we approximate p and k with the values at the centre of the faces:

$$\int_{e_u} (p + \varrho k) \, dA \approx (p_{I+1,J} + \varrho k_{I+1,J})|e_u|, \tag{3.10}$$

$$\int_{w_u} (p + \varrho k) \, dA \approx (p_{I,J} + \varrho k_{I,J})|w_u|. \tag{3.11}$$

- in the diffusive term we have both a frontal momentum flux contribution from the faces e_u and w_u and a lateral momentum flux contribution from the faces n_u and s_u:

$$\begin{aligned}\int_{\partial V_u} \nu_{\text{eff}} (\nabla u \cdot \mathbf{n}) \, dA = \int_{e_u} \nu_{\text{eff}} \frac{\partial u}{\partial x} \, dA - \int_{w_u} \nu_{\text{eff}} \frac{\partial u}{\partial x} \, dA + \\ + \int_{n_u} \nu_{\text{eff}} \frac{\partial u}{\partial y} \, dA - \int_{s_u} \nu_{\text{eff}} \frac{\partial u}{\partial y} \, dA.\end{aligned} \tag{3.12}$$

  Here, we develop the contributions from e_u and n_u, the other two are analogous.
  For the frontal momentum flux we approximate the viscosity with the value at the centre of the face, while we approximate the derivative of the velocity with a centred finite difference:

$$\int_{e_u} \nu_{\text{eff}} \frac{\partial u}{\partial x} \, dA \approx \nu_{\text{eff},\{I+1,J\}} \frac{u_{i+1,J} - u_{i,J}}{x_{i+1} - x_i}|e_u|. \tag{3.13}$$

For the lateral momentum flux we split the face n_u into the two halves related to the two cells $[x_{i-1}, x_i] \times [y_{j-1}, y_j]$ and $[x_i, x_{i+1}] \times [y_{j-1}, y_j]$:

$$n_u = [x_I, x_i] \times \{y_j\} \cup [x_i, x_{I+1}] \times \{y_j\}. \tag{3.14}$$

We employ again a centred finite difference to approximate the derivative of the velocity, while, for the approximation of the viscosity, we compute an average between the two cells sharing the face:

$$\int_{n_u} \nu_{\text{eff}} \frac{\partial u}{\partial y}\, dA = \int_{x_{I,j}}^{x_{i,j}} \nu_{\text{eff}} \frac{\partial u}{\partial y}\, dA + \int_{x_{i,j}}^{x_{I+1,j}} \nu_{\text{eff}} \frac{\partial u}{\partial y}\, dA, \tag{3.15}$$

$$\int_{x_{I,j}}^{x_{i,j}} \nu_{\text{eff}} \frac{\partial u}{\partial y}\, dA \approx \frac{1}{2}\Big(\nu_{\text{eff},\{I,J\}} + \nu_{\text{eff},\{I,J+1\}}\Big) \frac{u_{i,J+1} - u_{i,J}}{y_{J+1} - y_J} \frac{|n_u|}{2},$$

$$\int_{x_{i,j}}^{x_{I+1,j}} \nu_{\text{eff}} \frac{\partial u}{\partial y}\, dA \approx \frac{1}{2}\Big(\nu_{\text{eff},\{I+1,J\}} + \nu_{\text{eff},\{I+1,J+1\}}\Big) \frac{u_{i,J+1} - u_{i,J}}{y_{J+1} - y_J} \frac{|n_u|}{2}.$$

- in the convective term we have again both a frontal momentum flux contribution from the faces e_u and w_u and a lateral momentum flux contribution from the faces n_u and s_u:

$$\int_{\partial V_u} u(\mathbf{v} \cdot \mathbf{n})\, dA = \int_{e_u} uu\, dA - \int_{w_u} uu\, dA + \\ + \int_{n_u} uv\, dA - \int_{s_u} uv\, dA. \tag{3.16}$$

For the discretization we have to distinguish between the *transporting velocity*, coming from $\mathbf{v} \cdot \mathbf{n}$, and the *transported field*, that in this case is the velocity itself. For the former we average between the values sharing the face, while for the latter we have to consider an approximation using a differencing scheme, like the upwind method or the TVD methods. For the moment we simply denote this approximation with a superscript *, then several possible options will be explained in detail in Subsections 3.1.2 and 3.1.3. We develop only the contributions from e_u and n_u, the other two are analogous.
For the frontal momentum flux we approximate the transporting velocity with an average between the values at the centre of the two staggered cells sharing the staggered face:

$$\int_{e_u} uu\, dA \approx u^* \frac{u_{i,J} + u_{i+1,J}}{2} |e_u|. \tag{3.17}$$

For the lateral momentum flux we approximate the transporting velocity with an average between the values a the two ends of the face (see Figure 3.2):

$$\int_{n_u} uv\, dA \approx u^* \frac{v_{I,j} + v_{I+1,j}}{2} |n_u|. \tag{3.18}$$

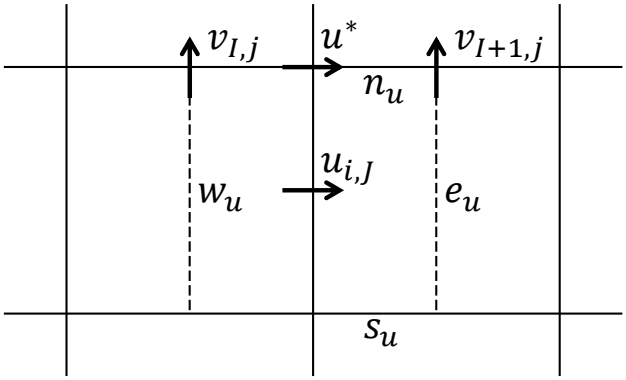

Figure 3.2: Degrees of freedom involved in the lateral part of the advective flux.

The equation for the component v of the velocity is analogous to the one for u described above, with the only addition of the gravity term:

$$\frac{\partial v}{\partial t} + \nabla \cdot (v\mathbf{v}) - \nabla \cdot (\nu_{\text{eff}} \nabla v) + \frac{1}{\varrho}\frac{\partial}{\partial y}\big(p + \varrho k\big) - g = 0, \tag{3.19}$$

with $g = -9.81\,\text{m/s}$. The gravity term is discretized simply as:

$$\int_{V_v} g \, dV = g|V_v|, \tag{3.20}$$

where $V_v = [x_{i-1}, xi] \times [y_J, y_{J+1}]$ is the "blue" control volume in Figure 3.1.

Turbulence model equations

The equations for the turbulent kinetic energy (2.47) and the specific dissipation rate (2.49) are treated analogously to the continuity equation, but they involve more terms. Let us integrate them over the same control volume $V_p = [x_{i-1}, x_i] \times [y_{j-1}, y_j]$:

- the storage terms are approximated with the values at the centre of the cell:

$$\int_{V_p} \frac{\partial k}{\partial t} \, dV = \frac{d}{dt} \int_{V_p} k \, dV \approx \frac{dk_{I,J}}{dt} |V_p|, \tag{3.21}$$

$$\int_{V_p} \frac{\partial \omega}{\partial t} \, dV = \frac{d}{dt} \int_{V_p} \omega \, dV \approx \frac{\partial \omega_{I,J}}{\partial t} |V_p|. \tag{3.22}$$

- the Gauss's divergence theorem is applied to the convective terms:

$$\int_{V_p} \nabla \cdot (k\mathbf{v})\, dV = \int_{\partial V_p} k(\mathbf{v} \cdot \mathbf{n})\, dA, \tag{3.23}$$

$$\int_{V_p} \nabla \cdot (\omega\mathbf{v})\, dV = \int_{\partial V_p} \omega(\mathbf{v} \cdot \mathbf{n})\, dA, \tag{3.24}$$

then the velocity is approximated with its value at the centre of the face, while for the transported quantities k and ω we employ the upstream value with respect to the sign of the velocity, so considering for example the face e_p and supposing that $u_{i,J} > 0$ we have:

$$\int_{e_p} ku\, dA \approx k_{I,J} u_{i,J} |e_p|, \quad \int_{e_p} \omega u\, dA \approx \omega_{I,J} u_{i,J} |e_p|. \tag{3.25}$$

Notice that this approach is not the only possible choice, as it will be explained with more details in Subsections 3.1.2 and 3.1.3.

- the Gauss's divergence theorem is applied to the diffusive terms:

$$\int_{V_p} \nabla \cdot \left[\left(\nu + \sigma^* \frac{k}{\omega} \right) \nabla k \right] dV = \int_{\partial V_p} \left(\nu + \sigma^* \frac{k}{\omega} \right) \nabla k \cdot \mathbf{n}\, dA, \tag{3.26}$$

$$\int_{V_p} \nabla \cdot \left[\left(\nu + \sigma \frac{k}{\omega} \right) \nabla \omega \right] dV = \int_{\partial V_p} \left(\nu + \sigma \frac{k}{\omega} \right) \nabla \omega \cdot \mathbf{n}\, dA. \tag{3.27}$$

Then, considering for example the face e_p, the derivatives of k and ω are approximated with centred finite differences, while the coefficients involving the viscosity are approximated by a weighted average between the values at the centre of the cells sharing the face, thus assuming a linear trend:

$$\int_{e_p} \left(\nu + \sigma^* \frac{k}{\omega} \right) \frac{\partial k}{\partial x}\, dA \approx \left(\nu + \sigma^* \frac{k}{\omega} \right)_{\text{avg}} \frac{k_{I+1,J} - k_{I,J}}{x_{I+1} - x_I} |e_p|, \tag{3.28}$$

$$\int_{e_p} \left(\nu + \sigma \frac{k}{\omega} \right) \frac{\partial \omega}{\partial x}\, dA \approx \left(\nu + \sigma \frac{k}{\omega} \right)_{\text{avg}} \frac{\omega_{I+1,J} - \omega_{I,J}}{x_{I+1} - x_I} |e_p|, \tag{3.29}$$

where the subscript $_{\text{avg}}$ denotes the weighted average

$$(*)_{\text{avg}} = \frac{x_{I+1} - x_i}{x_{I+1} - x_I} (*)_{I,J} + \frac{x_i - x_I}{x_{I+1} - x_I} (*)_{I+1,J}. \tag{3.30}$$

- in the source terms all the quantities are approximated with their value at the centre of the cell. We report here only the derivatives appearing in the entries of symmetric strain rate tensor $\mathbf{S}$, ∇k and $\nabla \omega$, that are computed with centred finite differences:

$$\left.\frac{\partial u}{\partial x}\right|_{I,J} \approx \frac{u_{i+1,J} + u_{i,J} - u_{i-1,J} - u_{i-2,J}}{2(x_{I+1} - x_{I-1})}, \tag{3.31}$$

$$\left.\frac{\partial v}{\partial y}\right|_{I,J} \approx \frac{v_{I,j+1} + v_{I,j} - v_{I,j-1} - v_{I,j-2}}{2(y_{J+1} - y_{J-1})}, \tag{3.32}$$

$$\left.\frac{\partial u}{\partial y}\right|_{I,J} \approx \frac{u_{i,J+1} + u_{i-1,J+1} - u_{i,J-1} - u_{i-1,J-1}}{2(y_{J+1} - y_{J-1})}, \tag{3.33}$$

$$\left.\frac{\partial v}{\partial x}\right|_{I,J} \approx \frac{v_{I+1,j} + v_{I+1,j-1} - v_{I-1,j} - v_{I-1,j-1}}{2(x_{I+1} - x_{I-1})}, \tag{3.34}$$

$$\left.\frac{\partial k}{\partial x}\right|_{I,J} \approx \frac{k_{I+1,J} - k_{I-1,J}}{x_{I+1} - x_{I-1}}, \quad \left.\frac{\partial k}{\partial y}\right|_{I,J} \approx \frac{k_{I,J+1} - k_{i,J-1}}{y_{J+1} - y_{J-1}}, \tag{3.35}$$

$$\left.\frac{\partial \omega}{\partial x}\right|_{I,J} \approx \frac{\omega_{I+1,J} - \omega_{I-1,J}}{x_{I+1} - x_{I-1}}, \quad \left.\frac{\partial \omega}{\partial y}\right|_{I,J} \approx \frac{\omega_{I,J+1} - \omega_{i,J-1}}{y_{J+1} - y_{J-1}}. \tag{3.36}$$

- the sink terms are approximated with the values at the centres of the cells:

$$\int_{V_p} \beta^* k\omega \, dV \approx \beta^* k_{I,J} \omega_{I,J} |V_p|, \tag{3.37}$$

$$\int_{V_p} \beta \omega^2 \, dV \approx \beta \omega_{I,J}^2 |V_p|. \tag{3.38}$$

3.1.2 Linear differencing schemes

The choice of the scheme for the approximation of a transported field is of great importance for both the accuracy and the stability of the solution of the problem. In general this decision has to be taken for every convective term, in our case in the discretization of the Navier-Stokes equations and of the turbulence model equations. As already mentioned, an important property that the scheme should have is the *transportativeness* (see [VM07]), i.e. it should take into account the direction of the flow. From a physical point of view this comes from the fact that, when in a flow convection dominates over diffusion, a bias towards the value on the face from which the flow comes should be applied. From a mathematical point of view instead we can introduce the following dimensionless number, the *Péclet number*:

$$Pe = \frac{|u|h}{2\nu}, \tag{3.39}$$

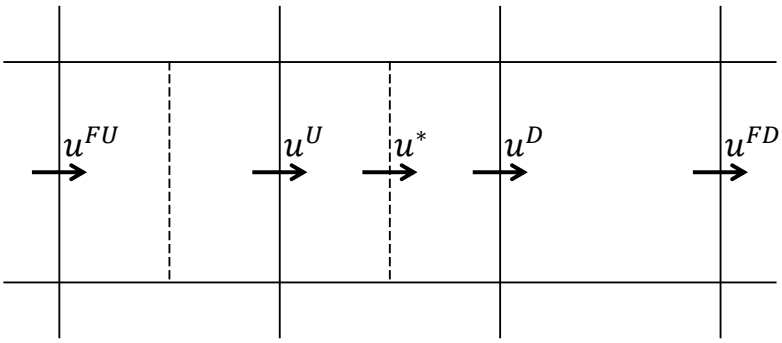

Figure 3.3: Location of the degrees of freedom used to approximate u^*. The superscripts ^{U}, ^{FU}, ^{D} and ^{FD} stand respectively for upstream, far-upstream, downstream and far-downstream. They hold for the case of positive transporting velocity at the face where u^* is.

where h denotes the cell width. It discriminates between stable and unstable discretization for a given flow: when the grid is too coarse or the viscosity is too low $Pe \to \infty$, and this can lead to a loss of stability of the numerical method (see for example [Qua14]).

In the following we will list the most straight-forward options for linear schemes, referring to the convective term of the equation (3.5) for the u component of the velocity. Here we consider uniform grids, with positive transporting velocity according to Figure 3.3, but all the schemes can be generalized to the case of non-uniform grids. Moreover the basic construction is one-dimensional, so that it may be used in every dimension for a multi-dimensional problems. For a complete description see for example [VM07].

CD scheme

The Central Differencing (CD) scheme consists in using an average between the two first neighbouring values:

$$u^* = \frac{u^D + u^U}{2}. \tag{3.40}$$

Employing Taylor expansions, it can be easily seen that this approximation is of second order, but, being symmetric, it does not have the transportativeness property. Indeed it can be shown that, when $Pe > 1$, it is not stable.

Upwind scheme

Opposed to the CD scheme, the upwind scheme consists in using only the upstream value:

$$u^* = u^U. \tag{3.41}$$

It is a simple, widely used and robust scheme as it has the transportativeness property, but its accuracy is only of first order, indeed it introduces in the solution an important amount of numerical diffusion that smooths the gradients.

Hybrid scheme

The hybrid scheme [Spa72] consists in evaluating if $Pe < 1$ or $Pe > 1$ at each face and then employing respectively the CD or the upwind. It exploits the good properties of the two schemes mentioned above, so it is highly stable and accurate when the diffusion is dominant, however the overall accuracy in terms of Taylor expansions reduces to first order.

QUICK scheme

The Quadratic Upstream Interpolation for Convective Kinetics (QUICK) scheme [Leo79] is a higher order method that involves an extended stencil of degrees of freedom. It can be obtained evaluating the quadratic interpolator of u^D, u^U and u^{FU} at the position where u^* is:

$$u^* = \frac{3u^D + 6u^U - u^{FU}}{8}. \tag{3.42}$$

Its accuracy is of third order, but it may produce unphysical overshoots or undershoots in the solution when there are strong gradients. This behaviour is not desirable, in particular in the case where the simulation involves quantities such as the turbulent kinetic energy k that have to be positive.

LUD scheme

The Linear Upwind Differencing (LUD) scheme is an extension of the upwind scheme that has a second order accuracy, however it can produce unphysical oscillations too. It can be obtained evaluating the linear interpolator of u^U and u^{FU} at the position where u^* is:

$$u^* = \frac{3u^U - u^{FU}}{2}. \tag{3.43}$$

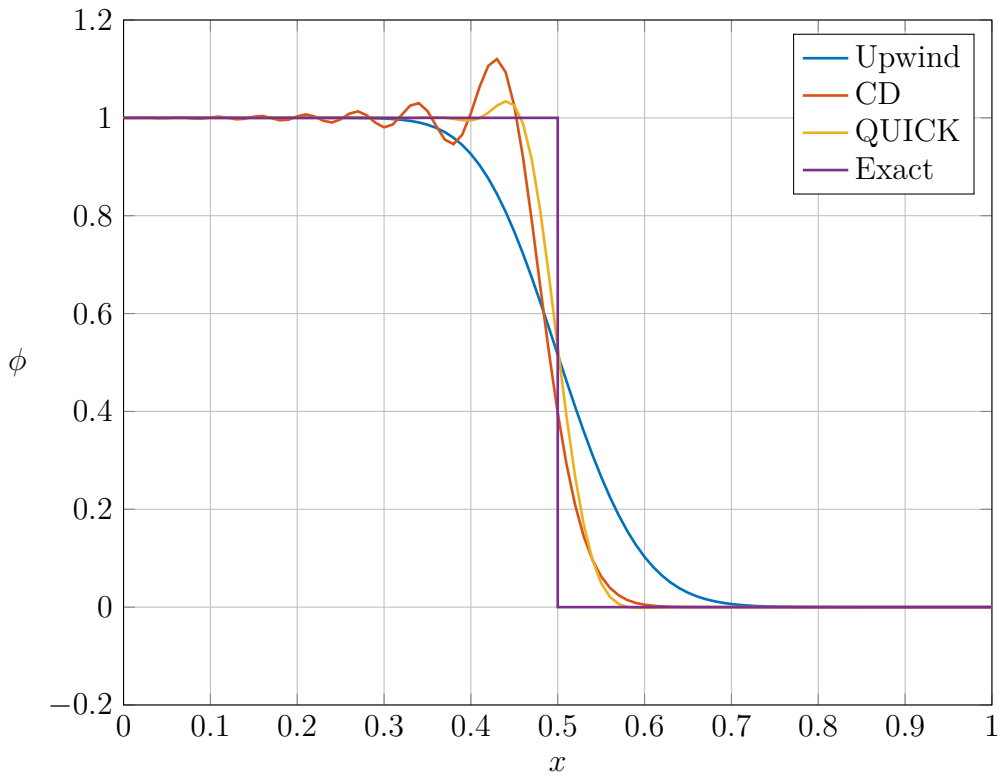

Figure 3.4: Solution of the problem (3.44)–(3.46) at the time $t = 0.5$. The upwind method smooths the gradient, while the CD and QUICK methods produce oscillations.

An example

We test the behaviour of the CD, Upwind and QUICK methods when they are applied to a one-dimensional scalar conservation law:

$$\frac{\partial \phi}{\partial t} + \frac{\partial \phi}{\partial x} = 0, \quad \forall x \in (0,1),\ \forall t > 0 \tag{3.44}$$

$$\phi(0,t) = 1, \quad \forall t > 0 \tag{3.45}$$

$$\phi(x,0) = 0, \quad \forall x \in (0,1) \tag{3.46}$$

In this case there is no diffusion but only the linear transport of a step from left to right. The equation (3.44) can be discretized with finite volumes storing the degrees of freedom at the ends of each cells, as it is in the staggered grid concept. Then the differencing schemes presented above can be applied to the discretization of the transport term, while for the temporal discretization we use the Backward Euler method (see Subsection 3.1.4).

In Figure 3.4 we can see the solution at $t = 0.5$. The upwind method is very diffusive near the step, but bounded within the extrema of the exact solution. The CD and QUICK methods instead better approximate the steep gradient, but produce oscillations for $x < 0.5$.

3.1.3 TVD methods

Total Variation Diminishing (TVD) methods belong to a category of methods called *high resolution methods* [Har83], that address the problem of computing a solution without any oscillation and with higher order accuracy, second order in this case. They were originally developed for scalar conservation laws of the type:

$$\frac{\partial \phi}{\partial t} + \frac{\partial f(\phi)}{\partial x} = 0. \tag{3.47}$$

For this kind of problems the *total variation* of the numerical solution can be defined as:

$$TV(\phi) = \sum_{i=1}^{N_{\text{dof}}-1} |\phi_{i+1} - \phi_i|, \tag{3.48}$$

where ϕ_i is the numerical solution at the node i of the discretized domain. A method is called TVD if the total variation of the solution does not increase with time:

$$TV(\phi^{n+1}) \leq TV(\phi^n) \quad \forall n > 0, \tag{3.49}$$

where ϕ^n is the numerical solution at the time-step t^n. In [Har83] it has been proved that a TVD scheme is *monotonicity preserving*, i.e. it does not create new local extrema, local minima are non-decreasing and local maxima are non-increasing. This is the desirable property that we would like to have to avoid the creation of solutions containing overshoots and undershoots, as it happens using the higher order methods presented in the previous subsection.

According to [Swe84] and [MMD16] we can achieve our goal adding to the first order upwind approximation a second order non-linear anti-diffusive flux:

$$u^* = u^U + \frac{1}{2}\psi(r)(u^D - u^U), \quad r = \frac{u^U - u^{FU}}{u^D - u^U}. \tag{3.50}$$

The flux includes a function ψ called *flux limiter*, which should dampen the flux contribution in regions of the domain where it could produce oscillations. It is chosen non-negative in order to preserve the sign of the flux and it depends on the variable r, defined as the ratio between two consecutive differences of the solution. The non-linearity cannot be avoided, in fact it was

proved by Godunov [God59] that any monotonicity preserving linear scheme can be at most first order accurate.

Exploiting the approximation (3.50) to solve a problem like (3.47) and imposing the TVD condition (3.49) on the solution, we obtain the following bounds for the flux limiter function:

$$\begin{aligned} \psi(r) &= 0 \quad \text{if} \quad r < 0, \\ \psi(r) &\leq \min\{2r, 1\} \quad \text{if} \quad 0 \leq r \leq 1, \\ \psi(r) &\leq 2 \quad \text{if} \quad r > 2. \end{aligned} \tag{3.51}$$

Notice that when $r < 0$ we are in presence of a local maximum or minimum, because the differences between the upstream and downstream nodes and the one between the far upstream and upstream nodes have opposite signs. When this happens, ψ is set to zero, so only the first order upwind contribution is employed in the approximation of u^*. It is also required to ψ to fulfil the following symmetry property:

$$\frac{\psi(r)}{r} = \psi\left(\frac{1}{r}\right), \tag{3.52}$$

which ensures that backward- and forward-facing gradients are treated in the same way.

In order to have a second order scheme, ψ must be at least Lipschitz-continuous, i.e. there must exists a constant $L > 0$ such that

$$|\psi(x_1) - \psi(x_2)| \leq L|x_1 - x_2| \quad \forall x_1, x_2 \in \mathbb{R}. \tag{3.53}$$

Moreover, following [Swe84] and [Van74], any second order scheme can be obtained as a convex combination of the CD scheme (3.40) and the LUD scheme (3.43), in the following way:

$$\psi(r) = \theta(r)\psi_{CD}(r) + (1 - \theta(r))\psi_{LUD}(r) \quad \forall r > 0, \tag{3.54}$$

where $\theta(r)$ is a parameter such that $0 \leq \theta(r) \leq 1$, $\forall r > 0$, while ψ_{CD} and ψ_{LUD} are the linear flux limiter functions that can be associated to the schemes CD and LUD rearranging the approximations (3.40) and (3.43) in the general TVD form expressed by (3.50):

$$\psi_{CD}(r) = 1 \quad \forall r, \tag{3.55}$$

$$\psi_{LUD}(r) = r \quad \forall r. \tag{3.56}$$

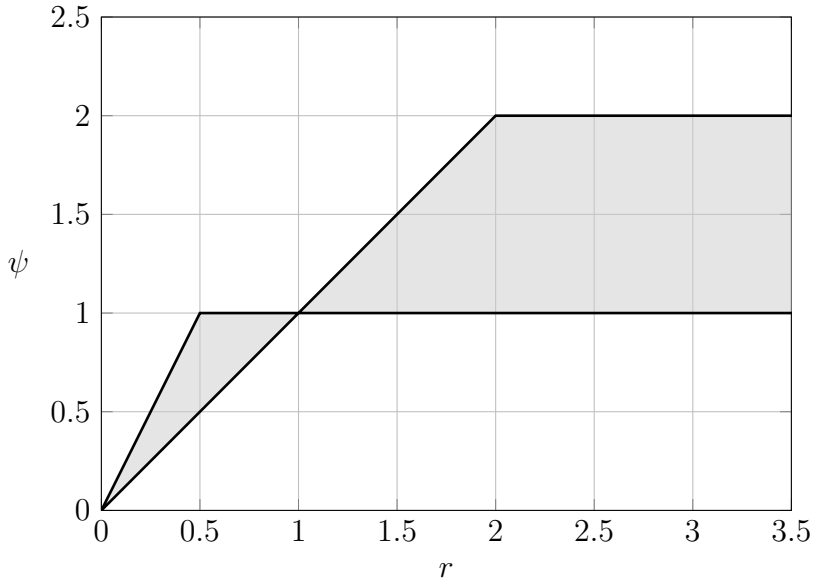

Figure 3.5: In grey the TVD region in which the flux limiter functions must fit. It is called also Sweby's diagram.

Thus, adding these requirements to the previous ones, we obtain the following bounds for the flux limiter function of a TVD method:

$$\begin{aligned} \psi(r) &= 0 \quad \text{if} \quad r < 0, \\ r \leq \psi(r) &\leq \min\{2r, 1\} \quad \text{if} \quad 0 \leq r \leq 1, \\ 1 \leq \psi(r) &\leq \min\{r, 2\} \quad \text{if} \quad r > 2. \end{aligned} \tag{3.57}$$

In Figure 3.5 they are reported in a $\psi - r$ diagram known also as Sweby's diagram.

Flux limters

Starting from the bounds (3.57), it is easy to create a flux limiter function. In literature many possible choices can be found. We list here some of the most popular functions that have been implemented in DuMu$^{\text{x}}$ and in Figure 3.6 we can see their graph in the Sweby's diagram:

- Van Leer [Van74]:

$$\psi(r) = \frac{r + |r|}{1 + r}. \tag{3.58}$$

  It is a smooth function that asymptotically reaches 2 for $r \to \infty$.

- Van Alabada [Van82]:

$$\psi(r) = \begin{cases} \dfrac{r^2 + r}{r^2 + 1} & \text{if } r \geq 0 \\ 0 & \text{if } r < 0 \end{cases}. \tag{3.59}$$

  It is a smooth function that instead goes to 1 as $r \to \infty$.

- Min-Mod [Roe85]:

$$\psi(r) = \max\{0, \min\{r, 1\}\}. \tag{3.60}$$

  It is a piecewise linear function that lies on the lower boundary of the TVD region. Intuitively, using this limiter we add to the upstream value half of the smallest increment in absolute value between $u^U - u^{FU}$ and $u^D - u^U$.

- Superbee [Roe85]:

$$\psi(r) = \max\{0, \min\{2r, 1\}, \min\{r, 2\}\}. \tag{3.61}$$

  It is a piecewise linear function that lies on the upper boundary of the TVD region.

- UMIST [LL94]:

$$\psi(r) = \max\left\{0, \min\left\{2r, \frac{3r+1}{4}, \frac{r+3}{4}, 2\right\}\right\}. \tag{3.62}$$

  It is a piecewise linear function that was designed as a symmetrical TVD version of QUICK.

- MC (Monotinized Central) limiter [Van77]:

$$\psi(r) = \max\left\{0, \min\left\{2r, \frac{r+1}{2}, 2\right\}\right\}. \tag{3.63}$$

  It is also known as MUSCL (Monotonic Upstream-Centred Scheme for Conservation Laws) limiter.

It is not easy to compare the different flux limiters in order to find the best one. Generally the Van Alabada and the Min-Mod can be slightly less accurate since $\psi \to 1$ as $r \to \infty$, while a scheme like the Superbee can produce sharper gradients, but sometimes the convergence can be slower.

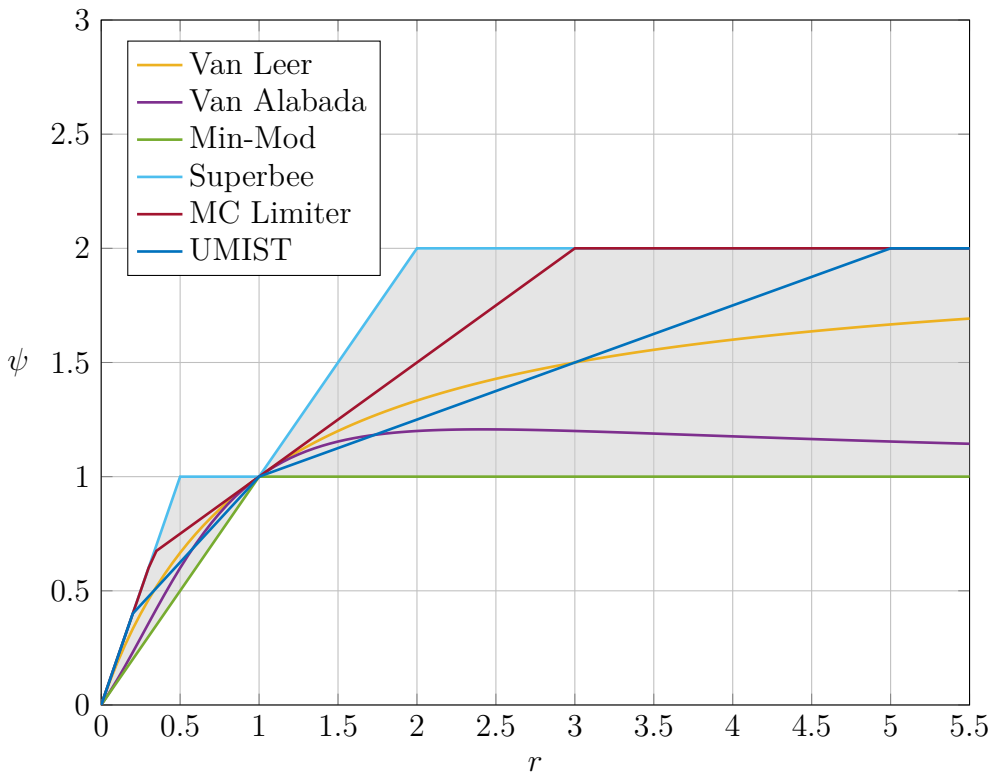

Figure 3.6: The Sweby's diagram with the flux limiters presented in this section as functions of r.

In particular, according to [Swe84], it is said to be *overcompressive*, i.e. it may turn sine waves into square waves. The UMIST instead has a more complex function, so its evaluation can be more expensive. However their performances should be compared case by case.

In Figure 3.7 we can see the application of the TVD method using the Van Leer flux limiter (3.58) to the problem (3.44)–(3.46). It can be observed that the gradient is approximated with the same accuracy of the QUICK scheme (3.42), but the overshoot for $x < 0.5$ is avoided. Because of their good behaviour, we will broadly use TVD methods in the numerical experiments reported in Chapter 4.

Non-uniform grids

The theory of TVD methods presented above holds for structured uniform grids. In order to deal with Cartesian non-uniform grids, that, for example, employ a grading, we have to generalize it considering the information about the distances between the degrees of freedom involved in the approximation.

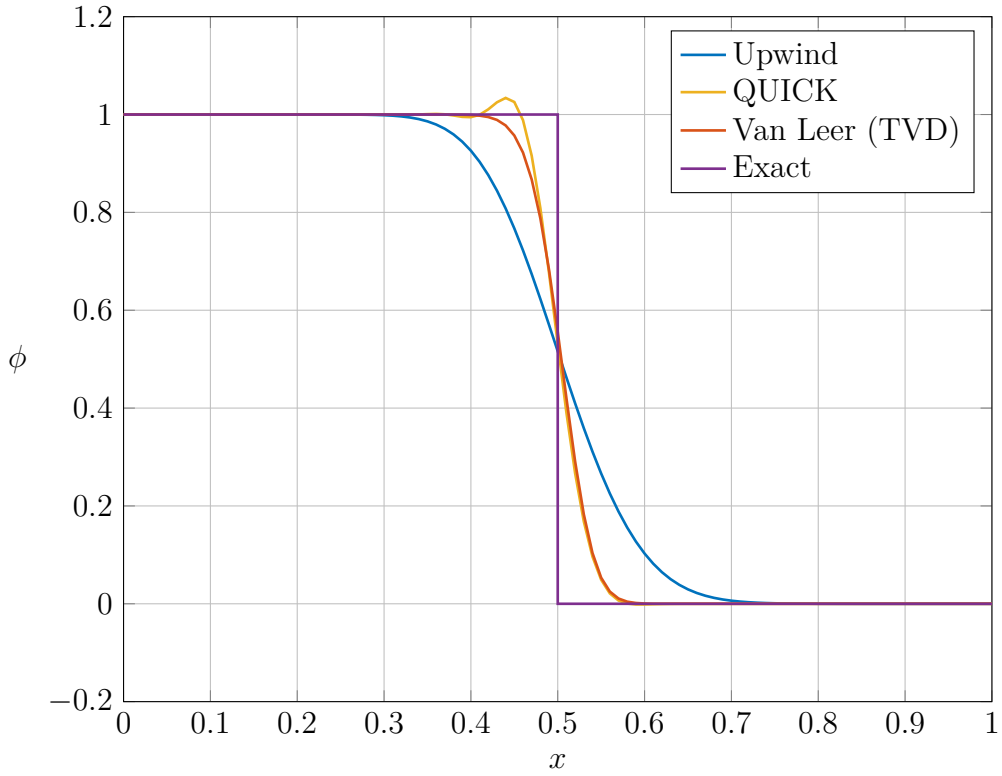

Figure 3.7: Solution of the problem (3.44)–(3.46) at the time $t = 0.5$. The TVD method approximates the gradient as accurately as the QUICK method, but it does not produce any overshoot for $x < 0.5$.

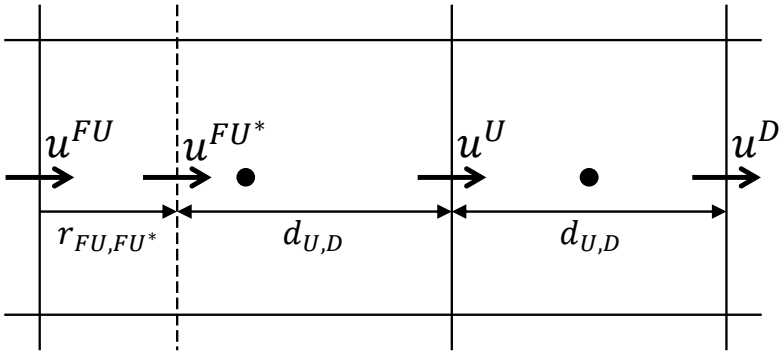

Figure 3.8: Non-uniform staggered grid. The distance between u^{FU^*} and u^U is the same that there is between u^U and u^D.

The generalization has always to be consistent, i.e. the approximation (3.50) has to be recovered in case of uniform grid. In literature several slightly different approaches can be found, see for example [Bru96], [DM03], [LL08], [BAM05], [HSH12] and [Zen13]. We describe here some of them.

A first simple approach consists in modifying the value of u^{FU} appearing in the factor r defined in (3.50).

The idea is that if the grid is not uniform, the distances between u^D and u^U and between u^U and u^{FU} might be different, as it is represented in Figure 3.8. In this situation the formula (3.50) cannot be used directly, because the degree of freedom u^{FU} is not at the position u^{FU^*}, where it would be if the grid was uniform, with cell sizes equal to the distance between u^U and u^D, i.e. at the position upstream with respect to u^U, at a distance equal to the one between u^U and u^D, see Figure 3.8. We want to use the ratio:

$$r = \frac{u^U - u^{FU^*}}{u^D - u^U},$$

thus we need to build an approximation for u^{FU^*}.

Darwish and Moukalled [DM03] proposed the following scheme that approximates the difference $u^D - u^{FU^*}$:

$$r = \frac{u^U - u^{FU^*}}{u^D - u^U} = \frac{(u^D - u^{FU^*}) - (u^D - u^U)}{u^D - u^U} = \frac{u^D - u^{FU^*}}{u^D - u^U} - 1, \tag{3.64}$$

$$u^D - u^{FU^*} \approx \frac{du^U}{dx} r_{FU^*,D} = 2\frac{du^U}{dx} r_{U,D}, \tag{3.65}$$

where $r_{A,B}$ denotes the vector from the point A to B. Li and Liao [LL08] showed that this method behaves well with parabolic solutions, but not so

well with exponential solutions. So they proposed an improved approximation which introduces more upwind information:

$$r = \frac{u^U - u^{FU^*}}{u^D - u^U}, \quad u^{FU^*} \approx u^{FU} + \frac{du^{FU}}{dx} r_{FU,FU^*}. \tag{3.66}$$

Hou et al. [HSH12] introduced a different and more rigorous approach. The idea in order to improve the approximations described above was to consider not only the distances between the degrees of freedom, but also the sizes of the cells around them. Let us consider for example a non-uniform staggered grid as in Figure 3.9.

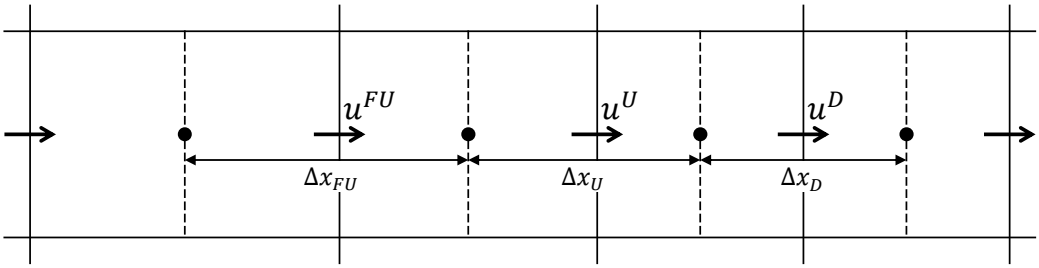

Figure 3.9: Non-uniform staggered grid with cell sizes.

We generalize (3.50) in the following way:

$$u^* = u^U + \frac{1}{R_{U,D}} \psi(r)(u^D - u^U), \tag{3.67}$$

$$R_{U,D} = \frac{\Delta x_U + \Delta x_D}{\Delta x_U}, \quad r = \frac{u^U - u^{FU}}{x^U - x^{FU}} \cdot \frac{x^D - x^U}{u^D - u^U}. \tag{3.68}$$

$R_{U,D}$ takes into account the sizes of the upstream and downstream staggered cells, while r is modified into the ratio between an approximation of the gradients. Notice that if the grid is uniform $R_{U,D} = 2$, as in the uniform formula (3.50).

Repeating the procedure described in the Subsection 3.1.3, the TVD condition (3.49) and the second order accuracy are imposed, obtaining the following modified bounds for the flux limiter function ψ:

$$\begin{aligned} \psi(r) &= 0 \quad \text{if} \quad r < 0 \\ r \leq \psi(r) &\leq \min\left\{\frac{R_{FU,U}}{R_{FU,U} - 1}, 1\right\} \quad \text{if} \quad 0 \leq r \leq 1 \\ 1 \leq \psi(r) &\leq \min\{r, R_{U,D}\} \quad \text{if} \quad r > 2 \end{aligned} \tag{3.69}$$

In Figure 3.10 we can see the modified TVD region; with respect to Figure 3.5, the upper bounds have changed. At last, the flux limiter functions (3.58)–(3.63) have to be generalized in order to fit into these new bounds.

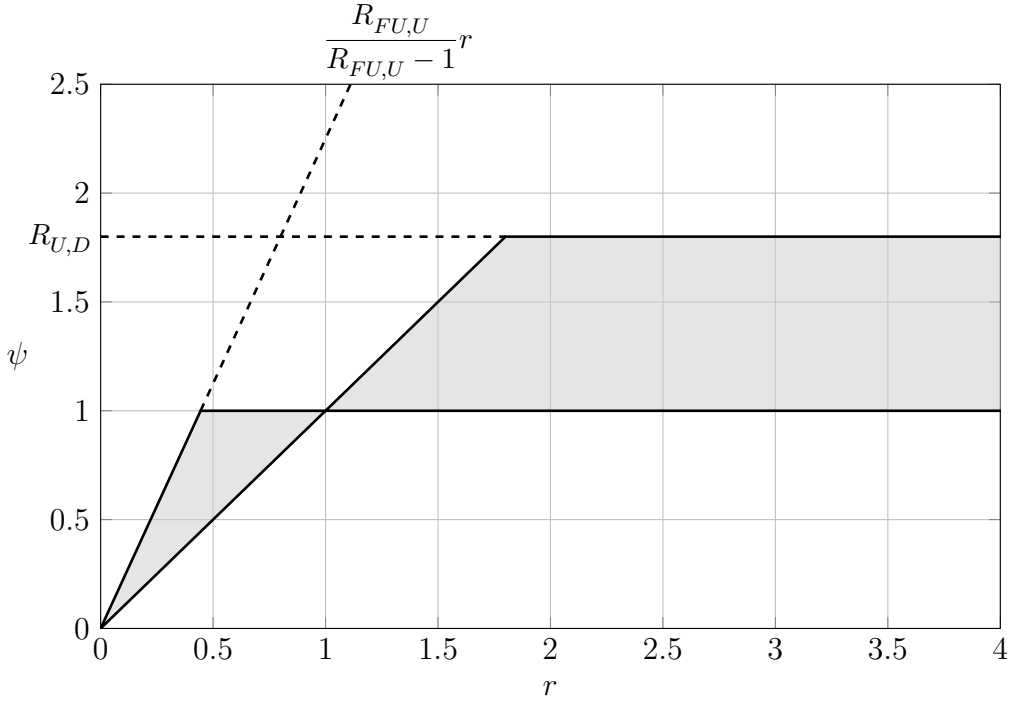

Figure 3.10: In grey the modified TVD region for non-uniform grids in which the flux limiter functions must fit [HSH12].

3.1.4 Time discretization

The RANS equations have to be discretized in time. Let us consider a vector $\boldsymbol{\phi}$ containing all the degrees of freedom of the components of the velocity $\mathbf{v}$, of the turbulent kinetic energy k and of its specific dissipation rate ω. After having performed the spatial discretization, we obtain the following system of Ordinary Differential Equations (ODEs):

$$\frac{d\boldsymbol{\phi}}{dt} = \mathbf{f}(\boldsymbol{\phi}, t), \tag{3.70}$$

where we have included in the function $\mathbf{f}$ at the right-hand side all the terms except the time derivative. We introduce a discretization of the time interval $(0, T)$ into N_t uniform time-steps, such that $\Delta t = T/Nt$ is the time-step size and $t^n = n\Delta t,\ n = 0, \ldots, N_t$. Let $\boldsymbol{\phi}^n$ be the numerical solution at the time t^n. In order to discretize in time the equations (3.70), we have employed two implicit schemes, so that at every iteration $\mathbf{f}$ will depend on $\boldsymbol{\phi}$ and t at the current time-step and not at the previous one.

Backward Euler method

The Backward Euler (BE) method (or implicit Euler method) consists in approximating the time derivative with a backward finite difference:

$$\frac{d\boldsymbol{\phi}}{dt} \approx \frac{\boldsymbol{\phi}^n - \boldsymbol{\phi}^{n-1}}{\Delta t} = \mathbf{f}(\boldsymbol{\phi}^n, t^n). \tag{3.71}$$

It is a first order method in terms of convergence and it is unconditionally stable, so no particular attention must be paid to the choice of Δt in order to guarantee the stability. Of course an initial condition $\boldsymbol{\phi}^0$ must be provided.

BDF2 method

The Backward Differencing Formula 2 (BDF2) method consists in approximating the time derivative with a backward finite difference of second order:

$$\frac{d\boldsymbol{\phi}}{dt} \approx \frac{3\boldsymbol{\phi}^n - 4\boldsymbol{\phi}^{n-1} + \boldsymbol{\phi}^{n-2}}{2\Delta t} = \mathbf{f}(\boldsymbol{\phi}^n, t^n). \tag{3.72}$$

It is of second order in terms of convergence and it is unconditionally stable too. It is a two-step method because it requires two initial conditions; this is a problem at the very first time step because we would need to know $\boldsymbol{\phi}^{-1}$. This issue is usually solved performing the first time-step with a one-step method, the BE usually, and then starting with the BDF2 from the second iteration. This procedure does not affect the overall convergence order, because a single step of a first order one-step method introduces a local truncation error that is of second order.

The method can be generalized to case of non constant time-steps. Let us define $\Delta t^n = t^n - t^{n-1},\ n = 1, \ldots, N_t$, then the scheme becomes:

$$\frac{d\boldsymbol{\phi}}{dt} \approx \boldsymbol{\phi}^n \left(\frac{1}{\Delta t^n + \Delta t^{n-1}} + \frac{1}{\Delta t^n} \right) - \boldsymbol{\phi}^{n-1} \frac{\Delta t^n + \Delta t^{n-1}}{\Delta t^n \Delta t^{n-1}} + \\ + \boldsymbol{\phi}^{n-2} \frac{\Delta t^n}{\Delta t^{n-1}(\Delta t^n + \Delta t^{n-1})} = \mathbf{f}(\boldsymbol{\phi}^n, t^n). \tag{3.73}$$

See [QSS07] for more detailed information about time discretization methods.

3.2 Porous-medium flow

In the porous-medium region Ω_{pm} we have to solve only a steady scalar equation, with the pressure as a primary variable, where, due to the incompressibility of the fluid, the time derivative is not present. It is obtained

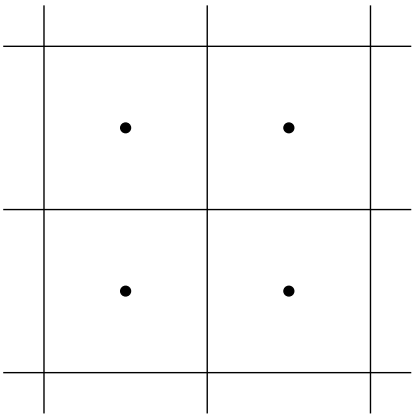

Figure 3.11: Location of the degrees of freedom within a cell-centred approach.

substituting the velocity computed with (3.75) into (3.74):

$$\nabla \cdot \mathbf{v} = 0 \tag{3.74}$$

$$\mathbf{v} + C_F\sqrt{\mathbf{K}}\frac{\varrho}{\mu}|\mathbf{v}|\mathbf{v} + \frac{1}{\mu}\mathbf{K}(\nabla p - \varrho\mathbf{g}) = \mathbf{0} \tag{3.75}$$

We employ a cell-centred finite volumes method, so the degrees of freedom of the pressure are located at the centre of each cell, as we can see in Figure 3.11, and the cells of the grid correspond to the control volumes.

Let us integrate the equation (3.74) over a control volume V_L (see Figure 3.12) and apply the Gauss's divergence theorem:

$$\int_{V_L} \nabla \cdot \mathbf{v}\, dV = \int_{\partial V_L} \mathbf{v} \cdot \mathbf{n}\, dA. \tag{3.76}$$

The Forchheimer's law (3.75) is non-linear, so locally we use the Newton's method to compute the velocity, i.e. the flux over the boundary ∂V_L:

$$\mathbf{J}_f(\mathbf{v}_k)\delta\mathbf{v}_{k+1} = -\mathbf{f}(\mathbf{v}_k), \quad \forall k \geq 0 \text{ until convergence} \tag{3.77}$$

$$\mathbf{v}_{k+1} = \mathbf{v}_k + \delta\mathbf{v}_{k+1}, \tag{3.78}$$

where

$$\mathbf{f}(\mathbf{v}) = \mathbf{v} + C_F\sqrt{\mathbf{K}}\frac{\varrho}{\mu}|\mathbf{v}|\mathbf{v} + \frac{1}{\mu}\mathbf{K}(\nabla p - \varrho\mathbf{g}) \tag{3.79}$$

and $\mathbf{J}_f(\mathbf{v})$ is its Jacobian matrix:

$$\mathbf{J}_f(\mathbf{v}) = \mathbf{I} + C_F\sqrt{\mathbf{K}}\frac{\varrho}{\mu}\Big(|\mathbf{v}|\mathbf{I} + \frac{1}{|\mathbf{v}|}\mathbf{v}\mathbf{v}^{\mathrm{T}}\Big). \tag{3.80}$$

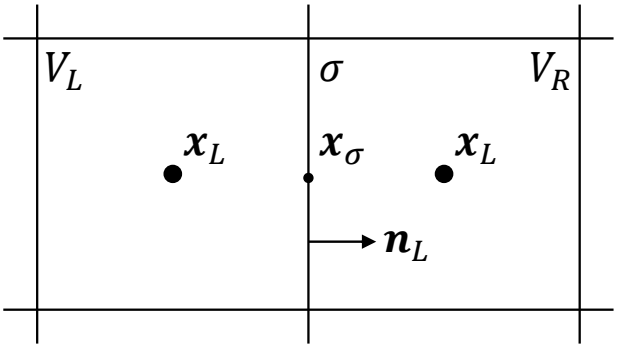

Figure 3.12: Two cells V_L and V_R sharing the face σ.

We use as initial guess $\mathbf{v}_0$ the velocity computed with the Darcy's law (2.67).

The evaluation of (3.79) and (3.80) over ∂V_L is performed with a Two Point Flux Approximation (TPFA) method, which exploits the values of the two cells sharing the face; it is a simple but robust method, commonly used in commercial software. Let us consider, for instance, the face $\sigma = \partial V_L \cup \partial V_R$, according to Figure 3.12, and let the permeability tensor be diagonal so that it act as a scalar. We approximate the derivative of the pressure $\partial p/\partial x$ with a centred finite difference:

$$\frac{\partial p}{\partial x} \approx \frac{p_R - p_L}{x_R - x_L}. \tag{3.81}$$

We approximate the permeability $\mathbf{K}$ with its value at $\mathbf{x}_\sigma$, while for the viscosity μ (and eventually the density ϱ) we employ the upwind value.

In case of discontinuous permeabilities at the face σ, an harmonic average weighted on the distances between the cell centres and the face is performed:

$$\frac{|x_R - x_L|}{\mathrm{K}} \approx \frac{|x_\sigma - x_L|}{\mathrm{K}_L} + \frac{|x_R - x_\sigma|}{\mathrm{K}_R}. \tag{3.82}$$

These formulas for the TPFA approximation are the simplified version for a Cartesian grid, while in the general case of an unstructured grid the method is derived exploiting a decomposition of the vector

$$\mathbf{d}_{L,\sigma} = \mathbf{x}_\sigma - \mathbf{x}_L, \tag{3.83}$$

based on the co-normal vector $\mathbf{K}\mathbf{n}_L$. Moreover it can be shown that this approximation is consistent only if the grid is $\mathbf{K}$-orthogonal, i.e. if $\mathbf{K}\mathbf{n}_L$ is parallel to $\mathbf{d}_{L,\sigma}$. See [Wol13] for further details.

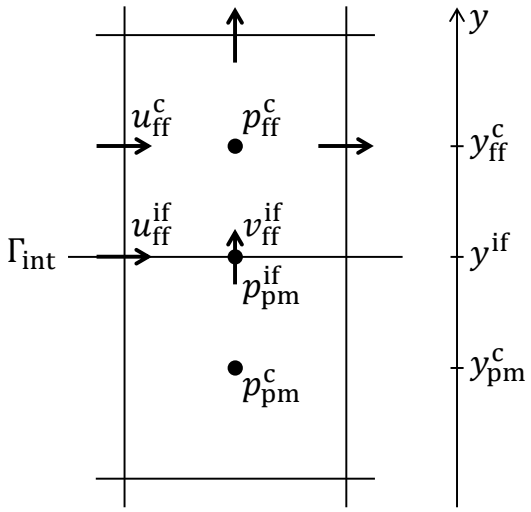

Figure 3.13: Cells at the coupling interface. The degrees of freedom $u^{\mathrm{if}}_{\mathrm{ff}}$ and $p^{\mathrm{if}}_{\mathrm{pm}}$ are fictitious.

3.3 Coupling conditions

The discretization of coupling conditions described in Section 2.3 requires attention because of the different concepts employed in the two subdomains. For the sake of simplicity, let us suppose to have a two-dimensional domain split by an horizontal interface, so that u and v are respectively the tangential and normal component of the velocity to the interface, and that the porous-medium occupies the lower subdomain. In Figure 3.13 the degrees of freedom of two cells touching the interface are represented. The superscripts $^{\mathrm{if}}$ and $^{\mathrm{c}}$ denote respectively the interface and the internal part of the cells. The degrees of freedom $u^{\mathrm{if}}_{\mathrm{ff}}$ and $p^{\mathrm{if}}_{\mathrm{pm}}$ are additional with respect to the staggered and cell-centred approaches, respectively, but they are fictitious, i.e. there is no equation associated to them, but their value is used only to impose the interface conditions. Let us suppose also that the permeability in the porous-medium is isotropic, so that we can consider it a positive scalar.

For the continuity of mass fluxes (2.72) we use the velocity of the free-flow at the interface $v^{\mathrm{if}}_{\mathrm{ff}}$ to express the flux across the boundary of the porous-medium.

For the continuity of normal stresses (2.74) the key point is the approximation of $p^{\mathrm{if}}_{\mathrm{pm}}$. This is done exploiting the Forchheimer's law (3.75) and approximating the derivative of p with a finite difference:

$$p^{\mathrm{if}}_{\mathrm{pm}} = p^{\mathrm{c}}_{\mathrm{pm}} + (y^{\mathrm{if}} - y^{\mathrm{c}}_{\mathrm{pm}})\Big[- \frac{\mu}{\mathrm{K}}\Big(v^{\mathrm{if}}_{\mathrm{ff}} + C_F\sqrt{\mathrm{K}} + \frac{\varrho}{\mu}|v^{\mathrm{if}}_{\mathrm{ff}}|v^{\mathrm{if}}_{\mathrm{ff}}\Big) + \varrho g\Big], \qquad (3.84)$$

where y^{if} and y^{c}_{pm} denote respectively the coordinates along the y-axis of $p^{\text{if}}_{\text{pm}}$ and p^{c}_{pm}. K and μ are evaluated at the centre of the porous-medium cell. Then, $p^{\text{if}}_{\text{pm}}$ is applied at the right-hand side of (2.74) and it is thus used as a natural boundary condition on Γ_{int}.

The Beavers-Joseph-Saffman condition (2.77) can be rewritten as

$$u = \frac{\sqrt{\text{K}}}{\alpha_{\text{BJ}}} \frac{\partial u}{\partial y} \quad \text{on } \Gamma_{\text{int}}. \tag{3.85}$$

Equation (3.85) is then discretized as

$$u^{\text{if}}_{\text{ff}} = \frac{\sqrt{\text{K}}}{\alpha_{\text{BJ}}} \frac{u^{\text{c}}_{\text{ff}} - u^{\text{if}}_{\text{ff}}}{y^{\text{c}}_{\text{ff}} - y^{\text{if}}} \tag{3.86}$$

and, rearranging the terms, we obtain

$$u^{\text{if}}_{\text{ff}} = \frac{u^{\text{c}}_{\text{ff}} \beta_{\text{BJS}}}{1 + \beta_{\text{BJS}}}, \quad \beta_{\text{BJS}} = \frac{\sqrt{\text{K}}}{\alpha_{\text{BJ}}} \frac{1}{y^{\text{c}}_{\text{ff}} - y^{\text{if}}}, \tag{3.87}$$

which can be used as a Dirichlet condition for the tangential component of the velocity.

3.4 Resulting algebraic equations

When all the equations have been discretized, we obtain for every time-step a non-linear algebraic system:

$$\mathbf{F}(\mathbf{x}^n) = \mathbf{0} \quad \forall n \geq 1, \tag{3.88}$$

where $\mathbf{x}^n \in \mathbb{R}^{N_{\text{dof}}}$ is the vector containing all the degrees of freedom of all the unknowns at the time-step t^n. This system is then solved monolithically using the Newton's method:

$$\mathbf{J}_F(\mathbf{x}^n_k)\delta\mathbf{x}^n_{k+1} = -\mathbf{F}(\mathbf{x}^n_k), \quad \forall k \geq 0 \text{ until convergence} \tag{3.89}$$

$$\mathbf{x}^n_{k+1} = \mathbf{x}^n_k + \delta\mathbf{x}^n_{k+1}, \tag{3.90}$$

starting from the solution at the previous time-step as initial guess $\mathbf{x}^n_0 = \mathbf{x}^{n-1}$. $\mathbf{J}_F$ is the Jacobian matrix of $\mathbf{F}$. Its entries are computed numerically using centred finite differences:

$$[\mathbf{J}_F]_{ij} = \frac{F_i(\mathbf{x}^n_k + \varepsilon_j \mathbf{e}_j) - F_i(\mathbf{x}^n_k - \varepsilon_j \mathbf{e}_j)}{2\varepsilon_j}, \tag{3.91}$$

where $\varepsilon_j = 10^{-8}|[\mathbf{x}_k^n]_j|$ and $\mathbf{e}_j$ is the j-th vector of the canonical basis in $\mathbb{R}^{N_{\text{dof}}}$. Notice that the evaluation of the residuals F_i related to the degrees of freedom in the porous-medium involves the application of the Newton's method (3.77)–(3.78). The convergence criterium is based on the relative shift: given a relative shift vector $\mathbf{s}$, whose components are computed as

$$s_i = \frac{[\delta\mathbf{x}_{k+1}^n]_i}{([\mathbf{x}_{k+1}^n]_i + [\mathbf{x}_k^n]_i)/2}, \tag{3.92}$$

and a tolerance *tol*, for example equal to 10^{-5}, we stop iterating when

$$\|\mathbf{s}\|_\infty < tol, \tag{3.93}$$

where $\|\cdot\|_\infty$ denotes the norm of the maximum

$$\|\mathbf{s}\|_\infty = \max_i |s_i|. \tag{3.94}$$

Eventually, the linear system (3.89) is solved with a direct solver, using the library UMFPack.

The time-step size is variable since at each new time iteration it is chosen multiplying the previous time-step size by a factor depending on how many iterations were required for the convergence of the Newton's method at the previous time iteration.

Chapter 4

Numerical results

In this chapter we present the numerical results. First, we perform some verification tests of the methods developed for the Navier-Stokes equations. The convergence of higher order methods is tested, first in space, then in time. After that, another comparison test between the upwind method and the TVD methods is performed, using a channel flow. Eventually, the results from the backward facing step test using RANS equations are shown and compared to those from the CFL3D code from [Lan15]. A second set of tests concerns the coupling with the porous-medium flow. First, we consider a turbulent flow through a channel with two cavities separated by a porous-medium and we study the influence of its permeability on the flow pattern. Then, we study a flow in a channel with a porous obstacle.

4.1 Navier-Stokes tests

4.1.1 Space convergence

We want to test the spatial convergence order of the error of the solution of the Navier-Stokes equations computed in the $L^2(\Omega)$ norm as

$$\|\phi_{\text{ex}} - \phi_h\|_{L^2(\Omega)} = \int_\Omega (\phi_{\text{ex}} - \phi_h)^2 \, dA, \tag{4.1}$$

where ϕ can denote velocity or pressure and ϕ_{ex} and ϕ_h are the corresponding exact and numerical solutions. We compare the results obtained with the upwind method (3.41) and the TVD methods described in Subsection 3.1.3. We consider a steady version of the equations (2.7)–(2.8), neglecting the

gravity term but taking into account two possible source terms h and $\mathbf{f}$:

$$\nabla \cdot \mathbf{v} - h = 0 \tag{4.2}$$

$$\nabla \cdot (\mathbf{v}\mathbf{v}^{\mathrm{T}}) - \nabla \cdot (\nu \nabla \mathbf{v}) + \frac{1}{\varrho}\nabla p - \mathbf{f} = \mathbf{0} \tag{4.3}$$

For the sake of simplicity, we consider here all the quantities appearing in the equations to be non-dimensional.

Sin-Cos test

Let us solve the equations (4.2)–(4.3) over a two-dimensional unit domain $\Omega = (0,1)^2$, with the following source terms:

$$h(x,y) = 0, \tag{4.4}$$

$$\mathbf{f}(x,y) = [-2\nu \cos(x)\sin(y),\ 2\nu \cos(y)\sin(x)]^{\mathrm{T}}, \tag{4.5}$$

so that, choosing $\varrho = 1$, the analytical solution, depicted in Figure 4.1, is given by

$$u_{\mathrm{ex}}(x,y) = -\cos(x)\sin(y), \tag{4.6}$$

$$v_{\mathrm{ex}}(x,y) = \sin(x)\cos(y), \tag{4.7}$$

$$p_{\mathrm{ex}}(x,y) = -\frac{\cos(2x) + \sin(2y)}{4}. \tag{4.8}$$

Dirichlet boundary conditions for the velocity are applied on the whole boundary $\partial\Omega$ using the exact solution. Because of this choice, the pressure solution is defined up to a constant, since it does not appear in the boundary conditions and only its gradient is involved in the momentum equation (4.3). Therefore, in order to match the particular exact solution (4.8), we fix at one point in the domain the value of the numerical solution.

The problem is solved over a sequence of five uniform grids, starting from 4×4 cells and each time halving their sizes. Both the cases of $\nu = 1$ and $\nu = 10^{-3}$ are tested, that correspond respectively to $Re = 1$ and $Re = 10^3$. In Figure 4.2, the computed errors are reported as functions of the square root of the number of cells, while in Table 4.1 we can compare directly the order of convergence for different differencing schemes.

We observe, as expected, a better behaviour of the TVD methods with respect to the upwind method. In Table 4.1a, we can see that, at $Re = 1$, the formers show a full second order convergence for the velocity, while for the pressure the rate is a bit lower; the latter, instead, shows a first order convergence for all variables. At $Re = 10^3$, a slight decrease of the rates of the

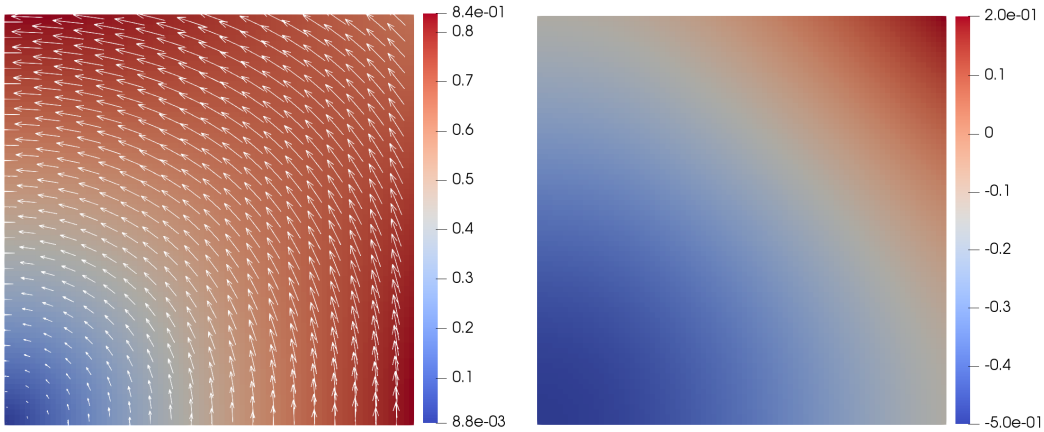

Figure 4.1: Exact solution of the Sin-Cos test (4.6)–(4.8). On the left the magnitude of the velocity field, on the right the pressure field.

	Upwind	Min-Mod	Van Leer
p	1.008	1.569	1.626
u	1.143	1.962	1.977
v	1.058	1.928	1.945

(a) $Re = 1$

	Upwind	Min-Mod	Van Leer
p	1.148	1.659	1.058
u	1.071	1.441	1.437
v	1.068	1.533	1.560

(b) $Re = 10^3$

Table 4.1: Convergence orders for the Sin-Cos test. They are computed considering the last two refinements of the grid.

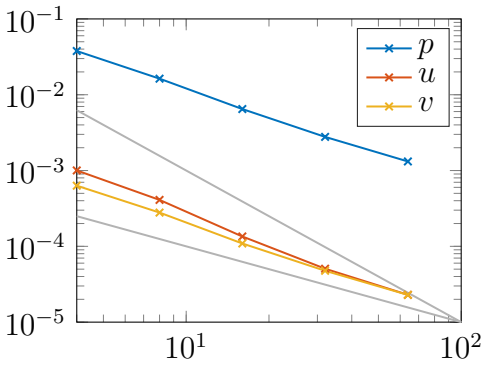

(a) Upwind, $Re = 1$

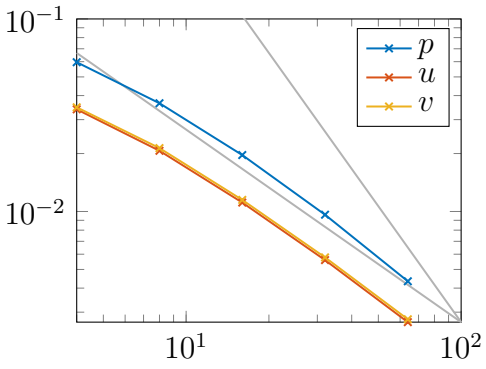

(b) Upwind, $Re = 10^3$

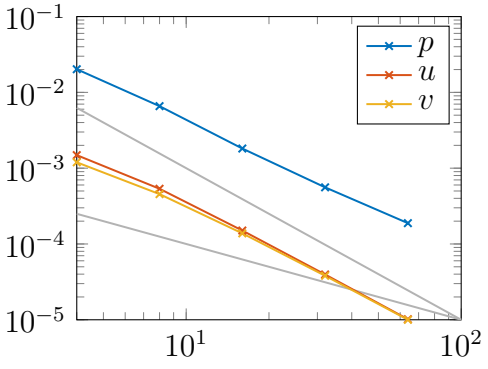

(c) Min-Mod, $Re = 1$

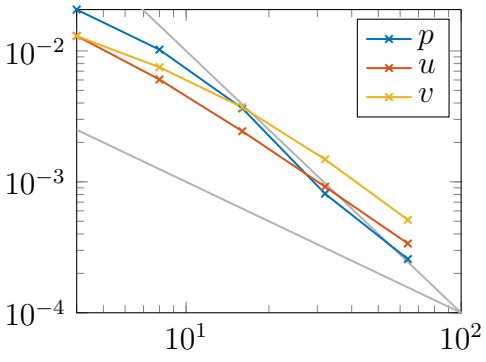

(d) Min-Mod, $Re = 10^3$

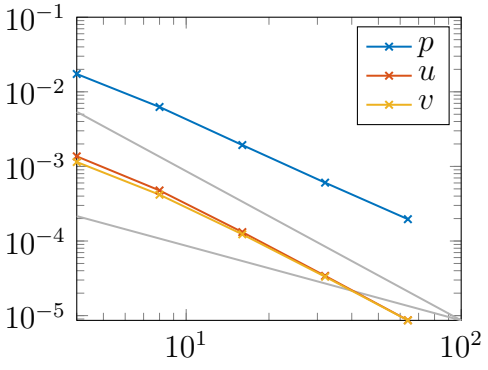

(e) Van Leer, $Re = 1$

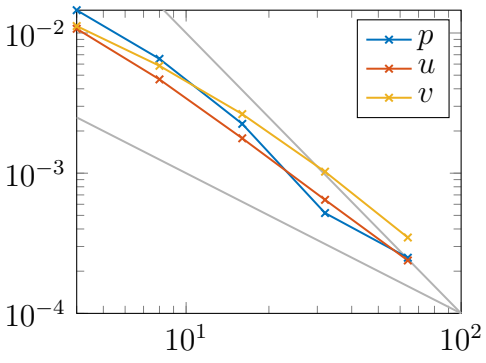

(f) Van Leer, $Re = 10^3$

Figure 4.2: $L^2(\Omega)$ norm of the errors for the Sin-Cos test depending on the square root of the number of cells in the grid. The grey lines are the reference lines parallel to a first order convergence (the lower one) and a second order convergence (the upper one).

TVD methods can be observed also for the velocities, but they remain higher then the ones of the upwind method. In Table 4.1b, we observe a convergence order of 1 for the pressure using the Van Leer flux limiter, but, looking at Figure 4.2f, we can see that the global trend points to a convergence of higher order. In this case the ratio between the errors at the last two refinements, reported in Table 4.1b, is misleading, because the error at the second-last refinement is smaller than expected. Moreover, it can be observed how, thanks to the faster convergence, on the same grid the absolute values of the errors reach smaller values using the TVD methods. The performances of the Min-Mod and Van Leer flux limiters are very similar.

Analogous tests with other analytical solutions are reported in Appendix A. They show always a better convergence of the TVD methods with respect to the upwind method, even of in some cases the convergence order of pressure and velocity behave differently.

4.1.2 Time convergence

We test the time convergence of the $L^\infty(0,T;L^2(\Omega))$ norm of the error of the solution of the Navier-Stokes equations:

$$\|\phi_{\text{ex}} - \phi_h\|_{L^\infty(0,T;L^2(\Omega))} = \operatorname{ess\,sup}_{t\in(0,T)} \|\phi_{\text{ex}}(t) - \phi_h(t)\|_{L^2(\Omega)}, \tag{4.9}$$

where ess sup denotes the *essential supremum* that for a function $f : \Omega \to \mathbb{R}$ is defined as

$$\operatorname{ess\,sup}_\Omega f = \inf\{M \in \mathbb{R} : |f(x)| \leq M \text{ a.e. in } \Omega\}. \tag{4.10}$$

In our case it will be the maximum of the $L^2(\Omega)$ norm of error over the time interval $(0,T)$. We compare the results obtained with the BE method (3.71) and the BDF2 method (3.72).
We consider the unsteady version of the equations (4.2)–(4.3):

$$\nabla \cdot \mathbf{v} - h = 0 \tag{4.11}$$

$$\frac{\partial \mathbf{v}}{\partial t} + \nabla \cdot (\mathbf{v}\mathbf{v}^{\mathrm{T}}) - \nabla \cdot (\nu \nabla \mathbf{v}) + \frac{1}{\varrho}\nabla p - \mathbf{f} = \mathbf{0} \tag{4.12}$$

Again gravity is neglected and two possible sources h and $\mathbf{f}$ are taken into account, moreover all the quantities are considered to be non-dimensional.

Unsteady Sin-Cos test

Let us solve the equations (4.11)–(4.12) over a two dimensional unit domain $\Omega = (0,1)^2$ and in the time interval $(0,T)$, with $T = 1$. We use the following

source terms:

$$h(x,y,t) = 0, \tag{4.13}$$

$$\mathbf{f}(x,y,t) = 2\Big(\frac{\cos(2t)}{\varrho} + \nu\sin(2t)\Big)[-\cos(x)\sin(y),\ \cos(y)\sin(x)]^{\mathrm{T}}, \tag{4.14}$$

so that, choosing $\varrho = 1$, the analytical solution is given by

$$u_{\mathrm{ex}}(x,y,t) = -\cos(x)\sin(y)\sin(2t), \tag{4.15}$$

$$v_{\mathrm{ex}}(x,y,t) = \sin(x)\cos(y)\sin(2t), \tag{4.16}$$

$$p_{\mathrm{ex}}(x,y,t) = -\frac{\cos(2x)+\sin(2y)}{4}\sin^2(2t). \tag{4.17}$$

The solution is equal to (4.6)–(4.8), used in the steady test for the space convergence, except for the modulation over time. We choose $\nu = 0.1$, so that $Re = 10$. Dirichlet boundary conditions for the velocity are applied on the whole boundary $\partial\Omega$ using the exact solution. The pressure is again fixed at one point in order to match the particular exact solution (4.17).

The problem is solved seven times subdividing the time interval $(0, T)$ into uniform time-steps and each time doubling their number, starting from a discretization with a single time-step. Uniform grids of 40×40 and 80×80 cells are employed and, as a differencing scheme, the TVD method with the Van Leer flux limiter (3.58) is used. From Figure 4.3, we observe that, as expected, the BE method shows a first order convergence, while the BDF2 method is of second order. Moreover we notice that, with a grid of 40×40 cells, in the last refinement the error with the BDF2 method does not decrease anymore. This happens because the grid is too coarse and the spatial error becomes dominant over the temporal one, so that, even with small time-steps, we cannot improve the solution. Refining the grid, the spatial error is reduced and the temporal order of convergence is restored entirely for the pressure and almost entirely for the velocity.

4.1.3 Rough channel test

We test the behaviour of the TVD methods compared to the upwind method solving the unsteady Navier-Stokes equations (2.7)–(2.8) in a two-dimensional channel with a *rough* (i.e. non-flat) lower boundary that consists of small, evenly spaced cavities. Two different configurations are studied, one with shallow cavities, depicted in Figure 4.4, and another with deeper cavities, depicted in Figure 4.10.

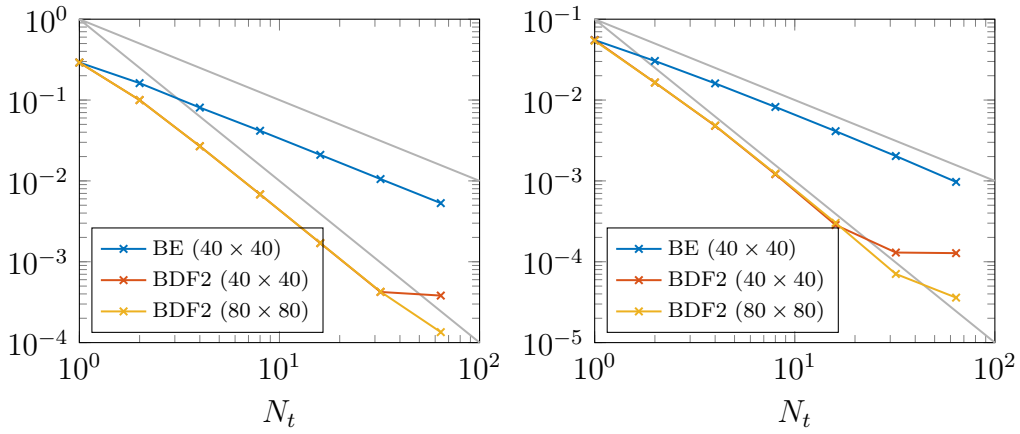

Figure 4.3: $L^\infty(0,T;L^2(\Omega))$ norm of the errors for the unsteady Sin-Cos test depending on the number of time-steps. On the left the errors for the pressure, on the right the errors for the magnitude of the velocity. The grey lines are the reference lines parallel to a first order convergence (the lower one) and a second order convergence (the upper one).

On the left boundary Γ_{in} we set inflow boundary conditions (2.9), specifying a horizontal velocity

$$\mathbf{v} = \mathbf{v}_{\text{in}} = [u_{\text{in}}, 0]^{\text{T}}, \quad u_{\text{in}} = 1\,\text{m/s}. \tag{4.18}$$

On the lower and upper boundaries Γ_w, we set no-slip boundary conditions (2.10), while on the right boundary Γ_{out} we set outflow boundary conditions (2.12), fixing the value of the pressure

$$p = p_{\text{ext}} = 1.1 \times 10^5\,\text{Pa}. \tag{4.19}$$

As initial conditions, velocity is set to zero everywhere, while pressure is set to p_{ext} everywhere. Density is $\varrho = 1\,\text{kg/m}^3$. The gravity contribution in (2.8) is neglected.

Shallow cavities

In the case of shallow cavities we use the domain in Figure 4.4 and we employ a uniform grid of 95×50 cells. The problem is then solved over the time interval $(0,T)$, with $T = 10\,\text{s}$. The initial time-step is $\Delta t = 5 \times 10^{-3}\,\text{s}$, then it is adapted as explained in Section 3.4, allowing a maximum time-step of $0.1\,\text{s}$. At first we set $\nu = 5 \times 10^{-4}\,\text{m}^2/\text{s}$, so that $Re = 2 \times 10^3$. Since we

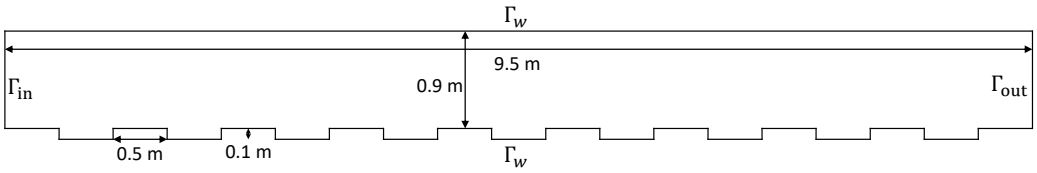

Figure 4.4: Domain of the rough channel test with shallow cavities.

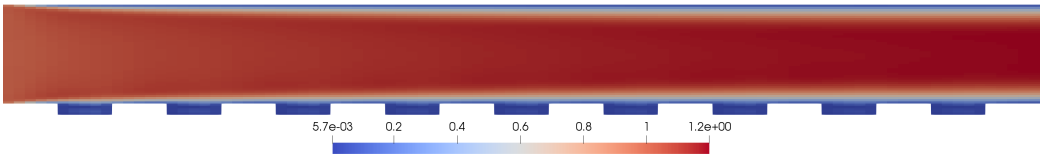

Figure 4.5: Magnitude of the velocity [m/s] in the rough channel test with shallow cavities at $t = T$. $Re = 2 \times 10^3$. Van Leer flux limiter.

do not have an analytical solution for this problem, we compute a *reference solution* using the upwind method over a grid six times finer (see Figure 4.7).

In Figure 4.8 we compare the profiles of the magnitude of the velocity along a cross-section near the end of the channel, at $x = 8.75\,\text{m}$, i.e. at the centre of the last cavity. The TVD solutions match the reference case, while the upwind solution shows a small shift, especially in the lower part of the channel, above the cavity. In Table 4.2, we can see the $L^2(\Omega)$ norm of the errors of the coarse solutions computed with respect to the reference one, along the cross-section mentioned above. The one related to the upwind method is at least one order of magnitude larger than the others.

We repeat the test choosing $\nu = 1\,\text{m}^2/\text{s}$, so that $Re = 1$. In Figure 4.9 we see that all the solutions have the same profile, moreover in the cavity there is not any recirculation. In Table 4.3 the $L^2(\Omega)$ norm of the errors are

Upwind	Van Leer	Van Alabada
1.708×10^{-4}	9.556×10^{-6}	1.119×10^{-5}
Min-Mod	Superbee	MC Limiter
1.537×10^{-5}	8.335×10^{-6}	8.659×10^{-6}

Table 4.2: $L^2(\Omega)$ norm of the errors for the profile of the magnitude of the velocity along the cross-section at $x = 8.75\,\text{m}$ and $t = T$ in the rough channel with shallow cavities. $Re = 2 \times 10^3$.

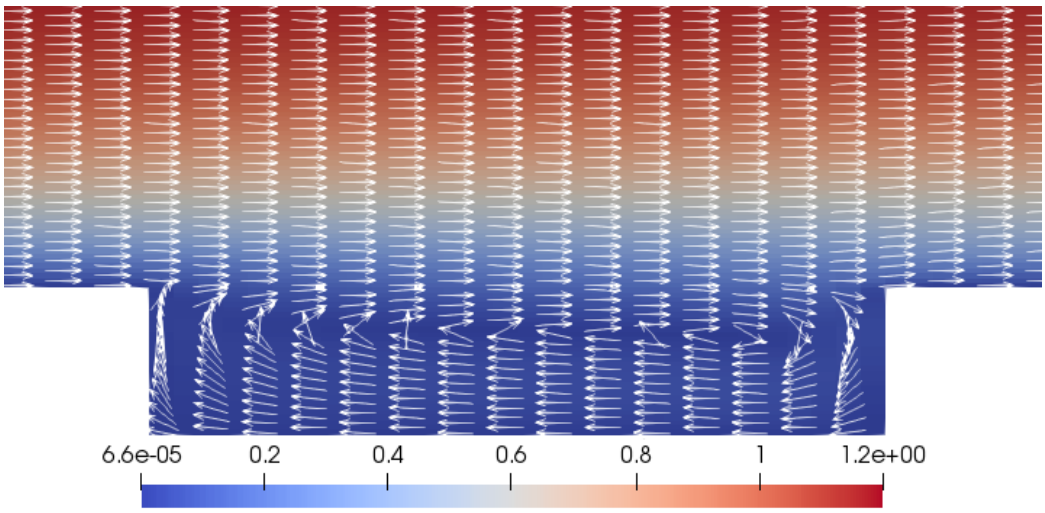

Figure 4.6: Magnitude of the velocity [m/s] in the rough channel test with shallow cavities, around the last cavity, at $t = T$, in the reference case. $Re = 2 \times 10^3$. The arrows are not scaled.

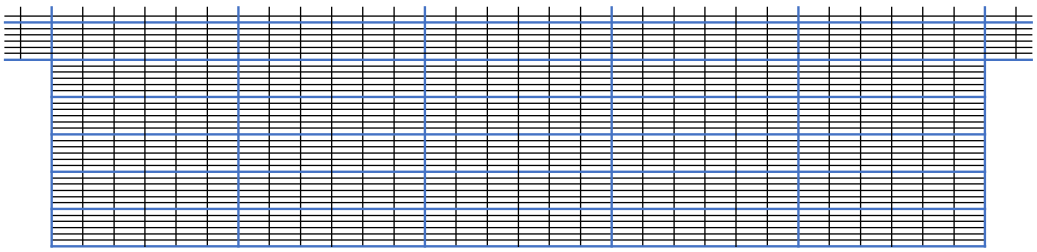

Figure 4.7: Comparison of the grids used in the rough channel test. In black the grid used for the reference solution, with cell sizes 16.7 mm × 3.3 mm, in blue the grid used in the other simulations, with cell sizes 100 mm × 20 mm.

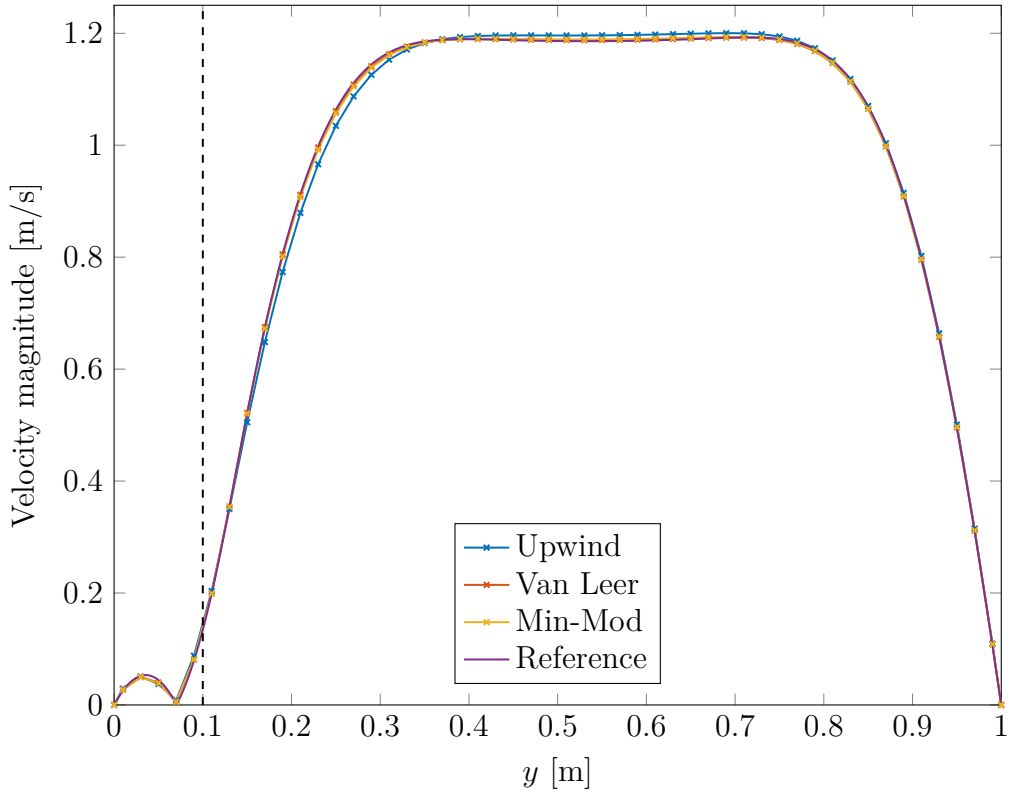

Figure 4.8: Profile of the magnitude of the velocity [m/s] in the rough channel with shallow cavities along the cross-section $x = 8.75\,\text{m}$, at $t = T$. $Re = 2 \times 10^3$. The region on the left of the dashed line is inside the cavity.

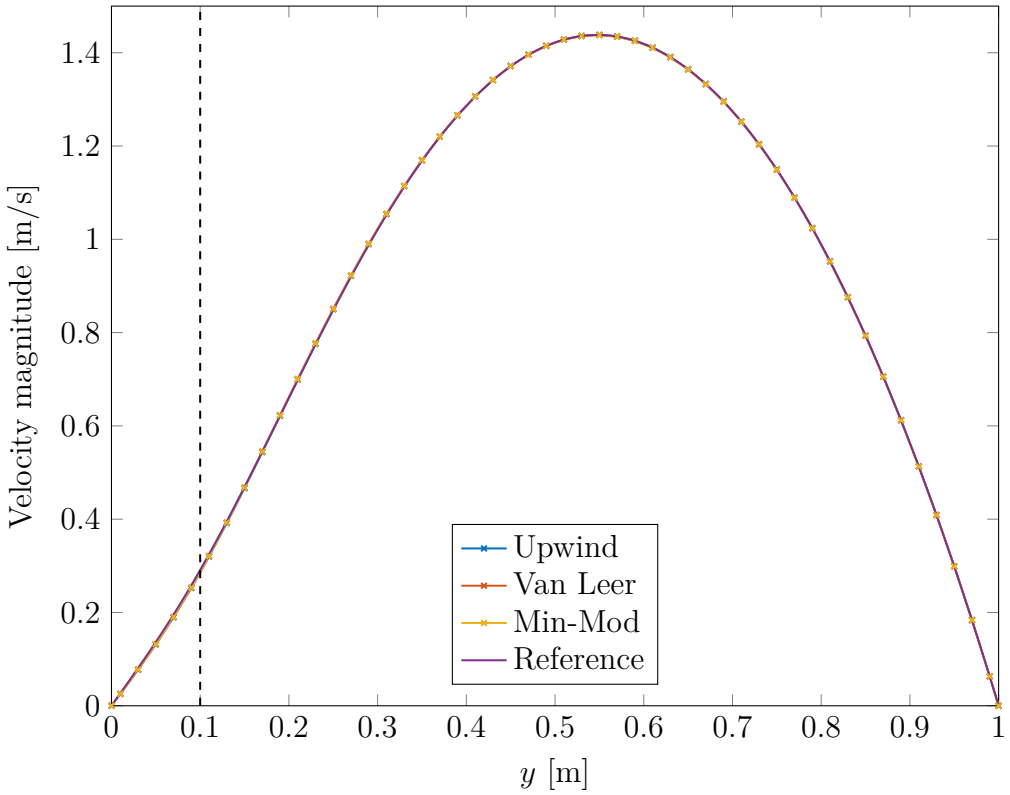

Figure 4.9: Profile of the magnitude of the velocity [m/s] in the rough channel with shallow cavities along the cross-section $x = 8.75\,\text{m}$, at $t = T$. $Re = 1$. The region on the left of the dashed line is inside the cavity.

reported; the upwind one is the bigger, but they are all very similar. So, in this situation of low Re, being the results very similar, the benefit of using a high-resolution scheme is reduced.

Deep cavities

In the case of deep cavities we use the domain in Figure 4.10 and we employ a uniform grid of 95×70 cells. Again we solve until $T = 10\,\text{s}$, starting from an initial time-step of $10^{-3}\,\text{s}$. We set $\nu = 5 \times 10^{-4}\,\text{m}^2/\text{s}$, so that $Re = 2.8 \times 10^3$. As before we compute a reference solution over a grid six times finer.

In Figure 4.11 we compare the profiles of the magnitude of the velocity along the cross-section at $x = 8.75\,\text{m}$. Now the biggest differences are in the region inside the cavity, where a recirculation occurs. The upwind method, with its numerical diffusion, smooths the profile, while the TVD methods produce more accurate results, even if they do not match exactly the reference

Upwind	Van Leer	Van Alabada
3.431×10^{-6}	2.917×10^{-6}	2.937×10^{-6}
Min-Mod	Superbee	MC Limiter
2.956×10^{-6}	2.899×10^{-6}	2.902×10^{-6}

Table 4.3: $L^2(\Omega)$ norm of the errors for the profile of the magnitude of the velocity along the cross-section at $x = 8.75\,\text{m}$ and $t = T$ in the rough channel with shallow cavities. $Re = 1$.

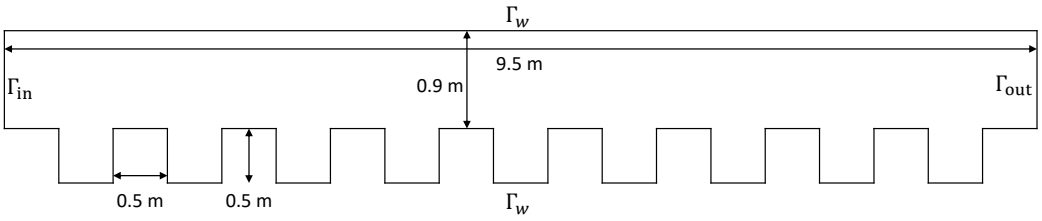

Figure 4.10: Domain of the rough channel test with deep cavities.

solution. Further, when looking at the $L^2(\Omega)$ norm of the absolute errors reported in Table 4.4, we see that the upwind method has again the largest error, but the difference with the other schemes is reduced with respect to the previous case of shallow cavities. This is due to the wider recirculation region with respect to the previous case, which is critical for the accuracy of all the methods because there we have local extrema for the velocity.

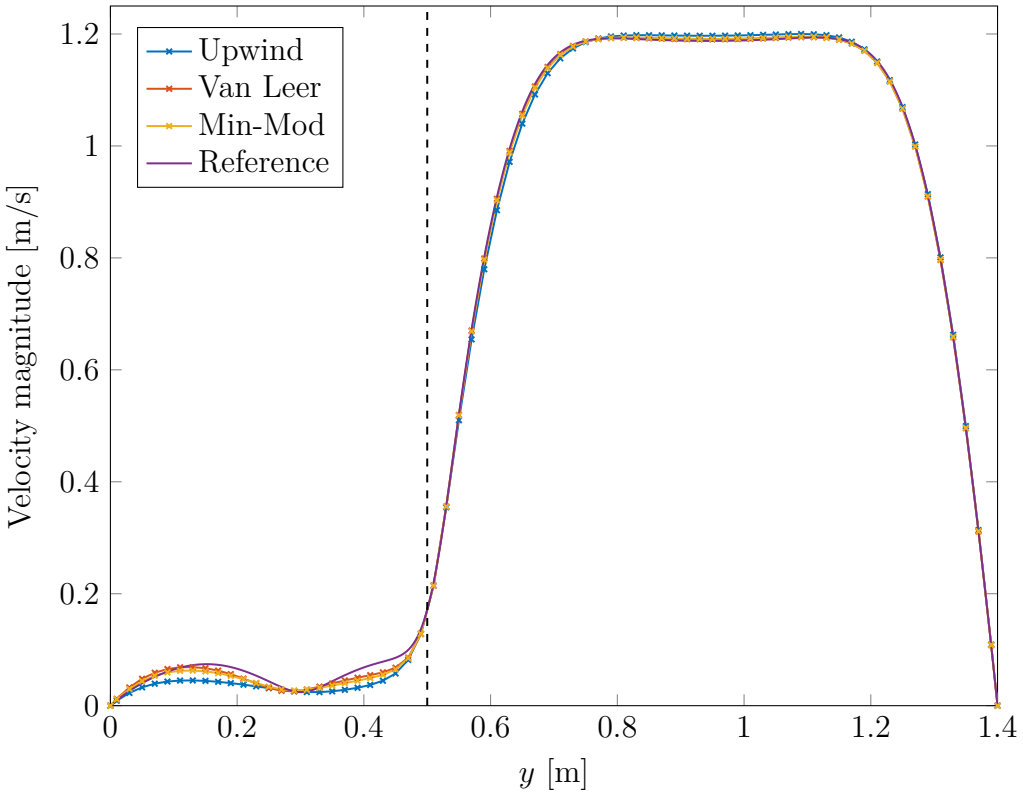

Figure 4.11: Profile of the magnitude of the velocity [m/s] in the rough channel with deep cavities along the cross-section $x = 8.75\,\text{m}$, at $t = T$. $Re = 2.8 \times 10^3$. The region on the left of the dashed line is inside the cavity.

Upwind	Van Leer	Van Alabada
3.180×10^{-4}	5.862×10^{-5}	6.900×10^{-5}
Min-Mod	Superbee	MC Limiter
8.579×10^{-5}	7.883×10^{-5}	5.584×10^{-5}

Table 4.4: $L^2(\Omega)$ norm of the errors for the profile of the magnitude of the velocity along the cross-section at $x = 8.75\,\text{m}$ and $t = T$ in the rough channel with deep cavities. $Re = 2.8 \times 10^3$.

4.2 RANS test: backward facing step

The backward facing step is a widely-used test configuration, in which a turbulent flow in a channel incurs separation because of a sudden enlargement in the flow domain. We see in Figure 4.13 the big recirculation that arises after the step, a smaller eddy near the corner and a very small eddy precisely at the corner. We want to use this problem in order to test the results that we obtain using the TVD method, with the Van Leer flux limiter (3.58), and the k-ω turbulence model, comparing them with the numerical results from [Lan15], computed using the NASA CFL3D code, and the experimental results from [DS85].

In the domain Ω, depicted in Figure 4.12, with a step height $H = 1\,\mathrm{m}$, we solve the RANS equations (2.22)-(2.23)-(2.47)-(2.49), imposing inflow boundary conditions on the left boundary Γ_{in}

$$\mathbf{v} = \mathbf{v}_{\mathrm{in}} = [u_{\mathrm{in}}, 0]^{\mathrm{T}}, \quad u_{\mathrm{in}} = 44.2\,\mathrm{m/s}, \tag{4.20}$$

no-slip boundary conditions on the lower and upper boundaries Γ_w and outflow boundary conditions on the right boundary Γ_{out}, fixing the value of pressure

$$p = p_{\mathrm{ext}} = 1.1 \times 10^5\,\mathrm{Pa}. \tag{4.21}$$

The density is $\varrho = 1\,\mathrm{kg/m^3}$ and the viscosity is $\nu = 1.228 \times 10^{-3}\,\mathrm{m^2/s}$, so that, in order to match [Lan15], the Reynolds number based on the step height results

$$Re_H = \frac{u_{\mathrm{in}} H}{\nu} \simeq 3.6 \times 10^4. \tag{4.22}$$

The domain sizes are chosen according to [Lan15], with the only exception of the channel length before the step. In fact, in [Lan15], a small portion of the horizontal boundary near Γ_{in} uses symmetry boundary conditions, but we simplify the model employing no-slip boundary conditions on the whole horizontal boundaries. As a consequence, we shorten the channel length in

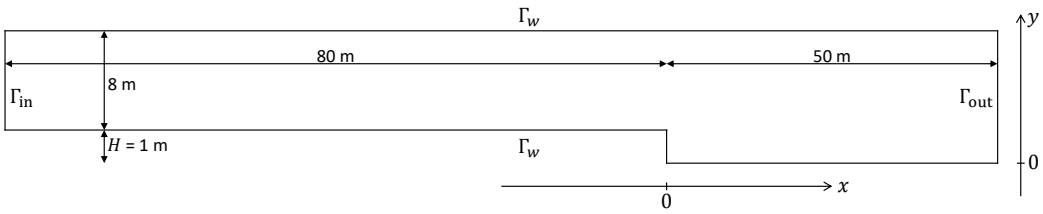

Figure 4.12: Domain Ω of the backward facing step test. For convenience, we set the origin of the x-axis in correspondence of the step and the origin of the y-axis at the bottom of the channel.

order to match the profile of the u component of the velocity along the cross-section at the position $x/H = -4$ as closely as possible, with a boundary layer thickness of approximately $1.5H$ (see Figure 4.16).

According to [Lan15], CFL3D is a code for compressible fluids, but it was used at "essentially incompressible" conditions, such that the influence of compressibility should be very small. Moreover it is reported that the model is unsteady, but it is solved until quasi-steady solution are obtained. In [KBR98] it is explained that a second order implicit method for the advancement in time is used.

Thus, we employ the BDF2 method with non-constant time-steps (3.73), starting from $\Delta t = 10^{-5}\,\mathrm{s}$ and simulating until $T = 30\,\mathrm{s}$. It can be observed that, after approximately $t = 20\,\mathrm{s}$, the solution stabilizes at a steady state. As initial conditions we set

$$p = p_{\text{ext}} \quad \forall \mathbf{x} \in \Omega, \quad \mathbf{v} = [u_{\text{init}}, 0]^{\mathrm{T}} \quad u_{\text{init}} = \begin{cases} u_{\text{in}} & \text{if } x \leq 0 \\ \frac{8}{9} u_{\text{in}} & \text{if } x > 0 \end{cases} \tag{4.23}$$

The factor $8/9$ ensures that the flow rate at Γ_{in} and at Γ_{out} is the same. For k and ω we set in the whole domain the values estimated with (2.56).

According to [Lan15], a key indicator for the reliability of a simulation is the prediction of the *reattachment length* l_{rea}, i.e. the distance after the step at which the recirculation finishes and thus the u component of the velocity at the bottom of the channel becomes positive. We analyse this length computing the *friction coefficient* C_f, that is a non-dimensional indicator of the stress at the wall, defined as

$$C_f = \frac{\tau_w}{\frac{1}{2}\varrho U_{\text{ref}}^2}, \quad \tau_w = \mu \frac{\partial u}{\partial y}\bigg|_{y=0}. \tag{4.24}$$

U_{ref} is the u component of the velocity at the centre of the channel at $x/H = -4$. In our case when $C_f < 0$ the flow is recirculating, then, at $x = l_{rea}$, C_f becomes positive. The numerical results from [Lan15] predict $l_{\text{rea}}/H \simeq 6.8$, while the experimental results from [DS85] predict $l_{\text{rea}}/H = 6.26 \pm 0.10$, as it can be seen in Figure 4.15.

Performing a sensitivity analysis in order to choose a suitable grid, we observe that:

- with a coarse mesh the reattachment length decreases, in particular a refinement of the smallest cell in the y-direction is effective.
- high aspect ratios in the cells increase the number of Newton iteration needed to get the convergence of the problem.

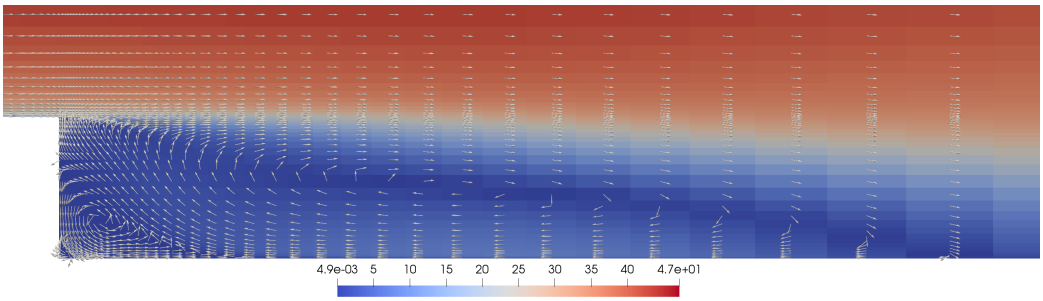

Figure 4.13: Velocity field [m/s] after the backward facing step at $t = T$. $Re_H = 3.6 \times 10^4$. The arrows are not scaled.

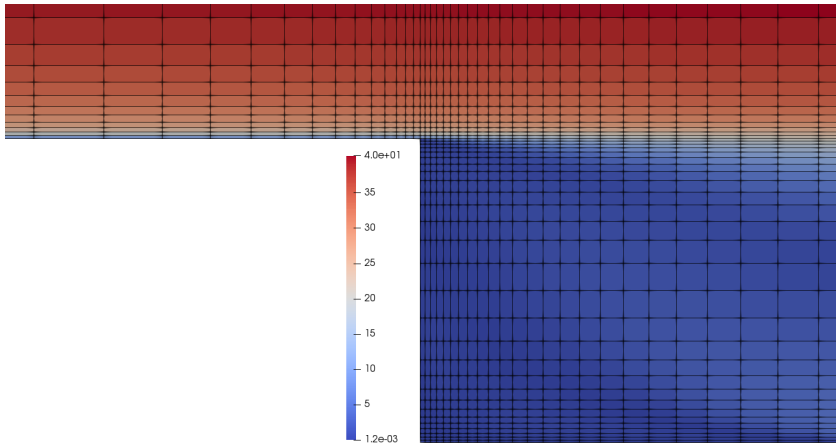

Figure 4.14: Velocity field [m/s] and grid around the backward facing step at $t = T$. $Re_H = 3.6 \times 10^4$. The arrows are not scaled.

- the cells in the portion of the channel after the step can be coarsened in the x-direction without a great influence on the solution.
- too refined cells in the y-direction in the area with the recirculation do not improve the solution in a relevant way.

So, in the following analysis, we choose a grid made of 119×70 cells, employing gradings up to 1.25 in order to have small cells near the walls, as it is required by the k-ω model. In Figure 4.14 we can see the grid in the region around the step.

Regarding the reattachment length, we obtain a good agreement with the CFL3D code; looking at Figure 4.15, with the Van Leer flux limiter we predict $l_{\text{rea}}/H \simeq 6.67$. Moreover, in the whole recirculating region, the two patterns are very similar, also compared to the experimental data from [DS85]. Using the first order upwind method, instead, we compute $l_{\text{rea}}/H \simeq$

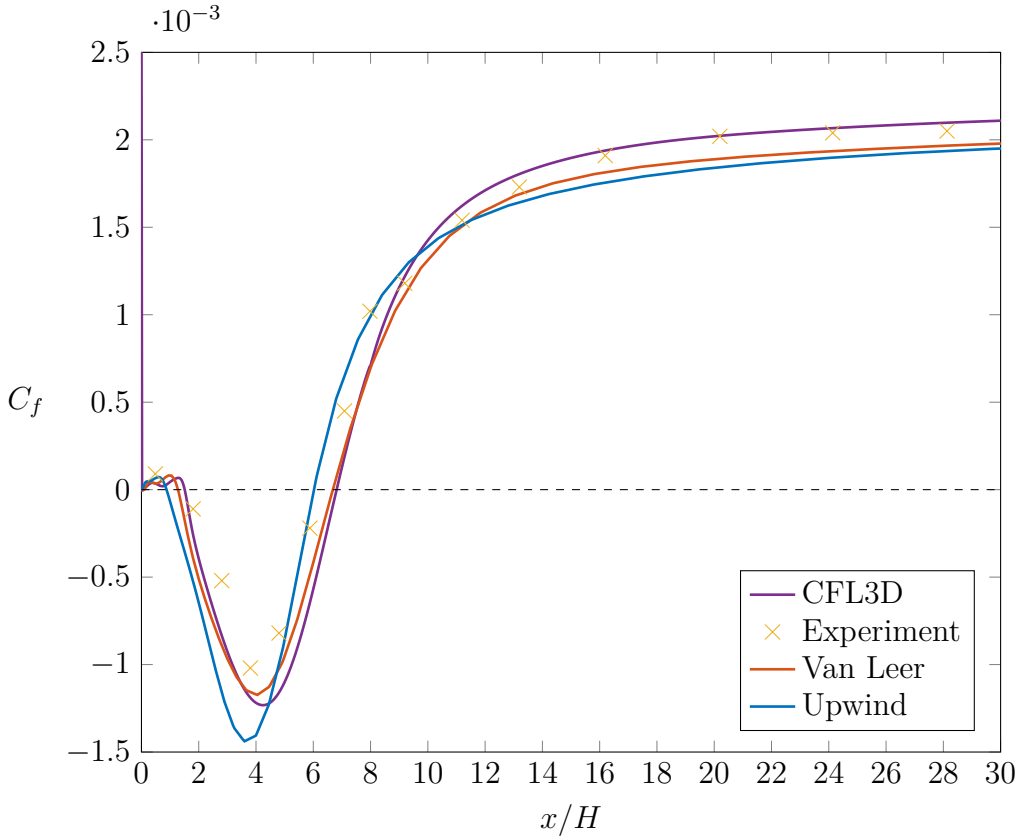

Figure 4.15: Friction coefficient at the bottom of the channel after the backward facing step at $t = T$. The reattachment length is the distance at which it becomes positive after its global minimum.

6.02, so approximately a 10% underestimation occurs. From the profile, it seems that the whole recirculation is slightly smaller. Looking at the value near the end of the channel, instead, both the Van Leer and the upwind show a lower value with respect to the CFL3D code. Comparing in Figure 4.16 the profiles of the u component of the velocity along some cross-sections downstream with respect to the step, we obtain, similarly, a good agreement between the Van Leer results and those from the CFL3D code, while the results from the upwind method present a small shift, in particular in the cases $x/H = 4$ and $x/H = 10$. Along the cross-section at $x/H = 1$, the velocity at the wall is positive for the Van Leer and the CFL3D, since we are in correspondence of the corner eddy. For the upwind method, instead, the velocity is negative, as we are already in the bigger eddy because the whole pattern is shifted.

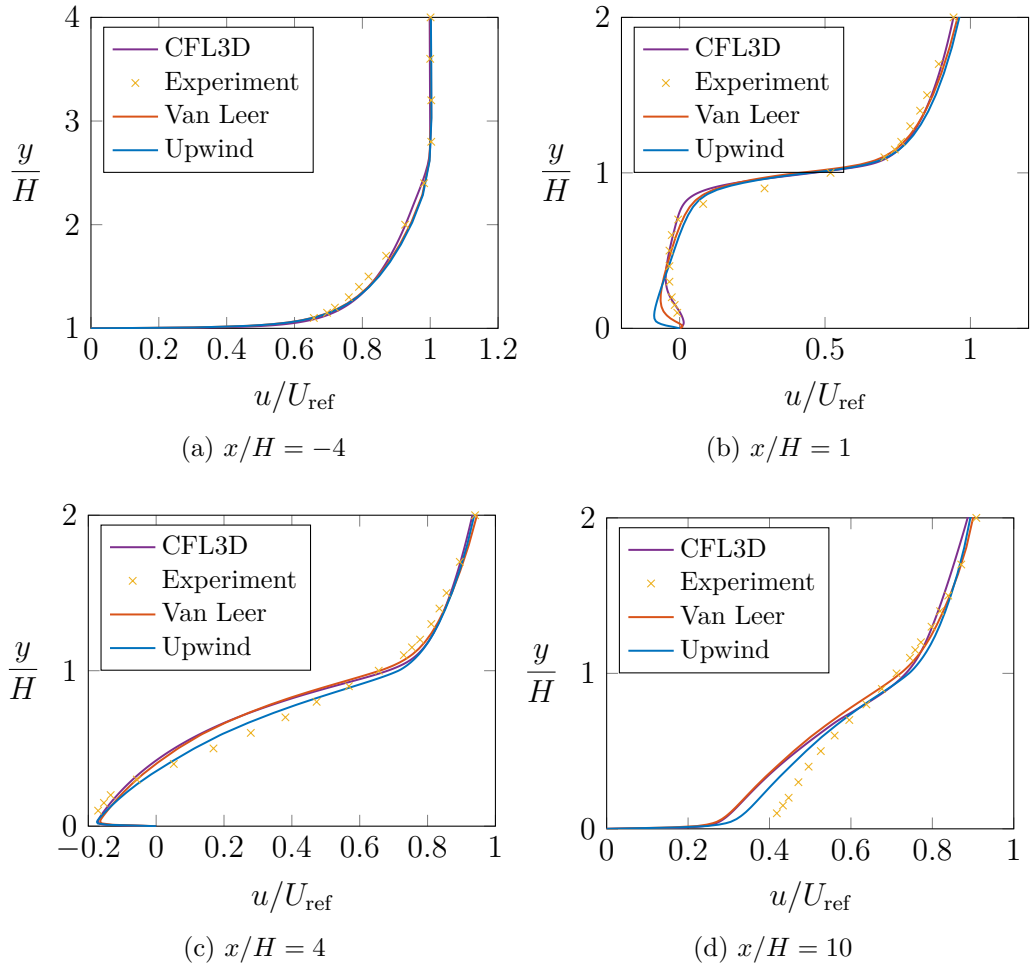

(a) $x/H = -4$ (b) $x/H = 1$

(c) $x/H = 4$ (d) $x/H = 10$

Figure 4.16: Profiles of the u component of the velocity [m/s] along four cross-sections in the backward facing step test at $t = T$. $Re_H = 3.6 \times 10^4$. U_{ref} is the velocity in the centre of the channel at $x/H = -4$.

4.3 Free-flow and porous-medium flow coupling

4.3.1 Cavities problem

In this subsection our goal is to study the behaviour of a coupled system with turbulent free-flow and porous-medium flow, that are in contact by means of a rough interface, exploiting the benefit of high resolution methods. A first approximation of this kind of interface can be obtained with a series of little cavities, as it is used in Subsection 4.1.3 to study the *rough channel* with the Navier-Stokes equations. Now we use the RANS equations with the k-ω that we tested in the previous section using the backward facing step case. In order to resolve the viscous sub-layer, we need very small cells next to the walls, that in this case are not flat but have different orientations. Since we are using a structured grid, the flexibility of employing local refinements in order not to increase the computational effort too much is limited, thus we decide to consider a simple configuration with only two cavities.

We start our analysis from the free-flow, studying the pattern of the velocity field and, in particular, how, without the porous-medium, the two cavities influence each other. After choosing a configuration such that this influence is minimized, we take into account the effect of a porous-medium, to see how its presence affects the whole flow field. We consider both the cases of shallow cavities and deep cavities.

Cavities mutual influence

In this first test we simulate only the free-flow, solving the RANS equations (2.22)-(2.23)-(2.47)-(2.49) in the domain Ω_{ff} depicted in Figure 4.17. It consists of a channel with inflow boundary conditions on the left boundary Γ_{in}:

$$\mathbf{v} = \mathbf{v}_{\text{in}} = [u_{\text{in}}, 0]^{\text{T}}, \quad u_{\text{in}} = 1\,\text{m/s}, \tag{4.25}$$

no-slip boundary conditions on the lower boundary Γ_w, symmetry boundary conditions on the upper boundary Γ_{sym} and outflow boundary conditions on the right boundary Γ_{out}, fixing the value of the pressure:

$$p = p_{\text{ext}} = 1.1 \times 10^5\,\text{Pa}. \tag{4.26}$$

The height of the channel is 0.6 m and it is chosen such that the flow is almost uniform in the upper part of the domain so that we can exploit the symmetry boundary conditions. The first portion of the lower wall is flat,

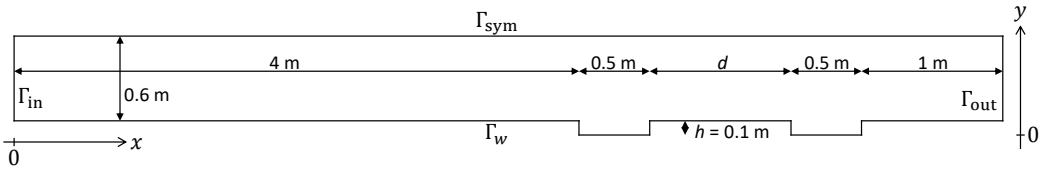

Figure 4.17: Free-flow domain Ω_{ff} in the cavities problem. The distance d is varied from 0.05 m to 2 m. For convenience we set the origin of the x-axis at Γ_{in} and the origin of the y-axis at the bottom of the cavities.

in order to let the flow develop, then there are the two shallow cavities of height $h = 0.1\,\text{m}$ and length 0.5 m, spaced by a tunable distance d.

We want to see how the flow field in the second cavity is affected by the presence of the first cavity, depending on the distance d between them, that can range from 0.05 m to 2 m.

The density of the fluid is $\varrho = 1\,\text{kg/m}^3$ and its kinematic viscosity is $\nu = 10^{-5}\,\text{m}^2/\text{s}$, so that the Reynolds number is $Re = 6 \times 10^5$. We neglect the gravity contribution. We simulate the time interval $(0, T)$, with $T = 30\,\text{s}$, such that the solution reaches an equilibrium, and we use an initial time-step $\Delta t = 10^{-3}\,\text{s}$. We start from the initial conditions of uniform parallel flow for $y > h$ and no flow for $y \leq h$

$$\mathbf{v} = [u_{\text{init}}, 0]^{\text{T}}, \quad u_{\text{init}} = \begin{cases} u_{\text{in}} & \text{if } y > h \\ 0 & \text{if } y \leq h \end{cases} \tag{4.27}$$

while we set in the whole domain Ω_{ff} $p = p_{\text{ext}}$, $k = k_{\text{in}}$ and $\omega = \omega_{\text{in}}$, estimated with the formulas (2.56).

Performing a sensitivity analysis, we choose a grid made of 377×50 cells for the case of $d = 1\,\text{m}$. It is important to have small uniform cells in the region of the cavities, so we employ gradings of 1.1 in the x-direction in the inlet and outlet portions of the channel, where we can afford to have longer cells. In the y-direction we employ instead a grading of 1.2 in the region above the cavities. As a result, the cell size around the two cavities is $5\,\text{mm} \times 3.3\,\text{mm}$. When $d < 1\,\text{m}$ also the cells between the cavities are uniform, while when $d \geq 1\,\text{m}$ a slight symmetric grading of 1.025 is employed.

At a first glance, the behaviour of the fluid in the two cavities is very similar, there is not any strong influence of the first one on the second one and the pattern of the velocity field is the same, as we see in Figure 4.18. In order to better analyse the results of the simulations, we compare the profiles of the u component of the velocity in the first cells above $y = h$. The velocity in these points drives the flow in the cavities, since we start from an initial condition of zero velocity inside them. Looking at the profiles in Figure 4.19,

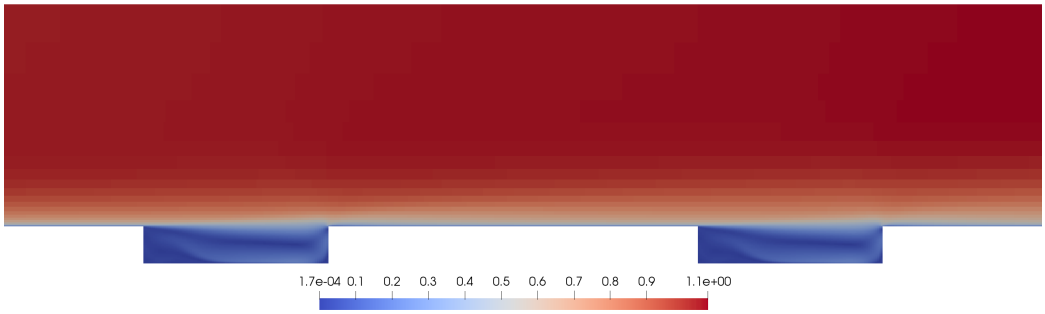

Figure 4.18: Magnitude of the velocity field [m/s] around the cavities, with $d = 1\,\text{m}$ at $t = T$. $Re = 6 \times 10^5$.

there is a positive peak of the velocity near the centre of each cavity, then, after the end of the cavity, there is a negative peak, followed by a length of approximately 0.5 m, hereby referred to as the recovery distance d_{rec}. In this distance, the flow returns nearly to the dynamics before the cavity, in particular the velocity recovers the value correspondent to $x = 4\,\text{m}$. The values in the second cavity are slightly lower than the corresponding ones in the first cavity, but the shape is the same. This confirms the fact that the behaviour of the flow in the two cavities is analogous.

The peaks above the cavities are due to the fact that those sections of the profile are not touching the wall, so the effect of wall friction is lower with respect to other sections and this allows the velocity to reach higher values. Then, at the end of the cavities, where the wall begins, there is a sudden decrease in the velocity because, before the corner of the cavity, the flow is split into a portion that goes down and generates the recirculation and another portion that instead goes up, as we observed in Figure 4.20. It is likely that this change in the flow direction implies a reduction in the u component of the velocity. After the distance d_{rec}, the effect of the wall has restored the boundary layer present before the cavity. If the distance between the cavities is smaller than the recovery distance, i.e. $d < d_{rec}$, the flow in the second cavity will be slower because it will be driven by lower velocities.

We report in Figure 4.21 the maximum values of the u component of the velocity in correspondence of the peak above the second cavity, depending on the distance between the cavities. We see that if $d < d_{rec}$ the velocity is affected by the presence of the first cavity, which reduces its value. For $d > d_{rec}$ the velocity is slightly decreasing as d increases; this fact can be interpreted as the effect of the turbulence that is generated near the end of the first cavity. As it can be seen in Figure 4.22, the turbulent kinetic energy

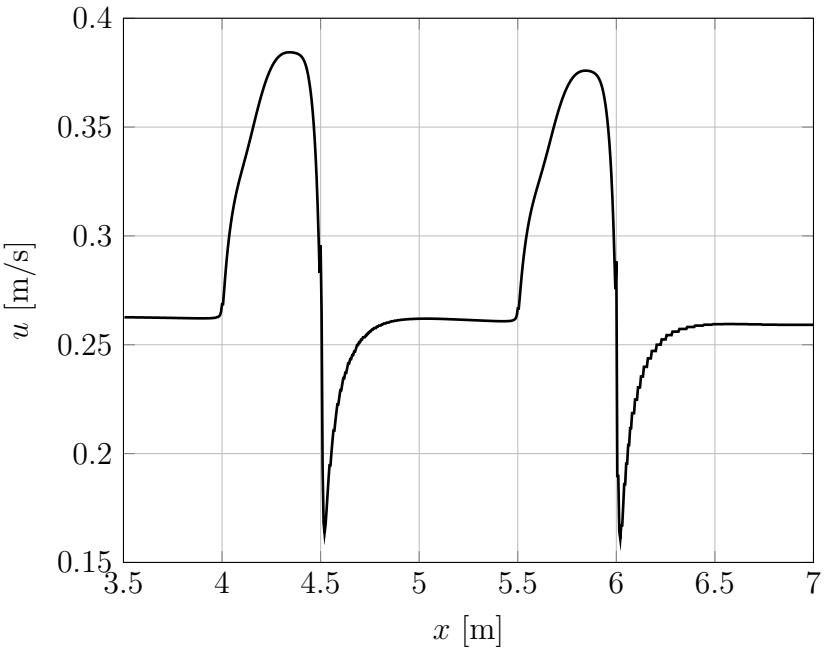

Figure 4.19: Profile of the u component of the velocity at $y = h$, with a distance $d = 1\,\text{m}$ between cavities, at $t = T$. $Re = 6 \times 10^5$.

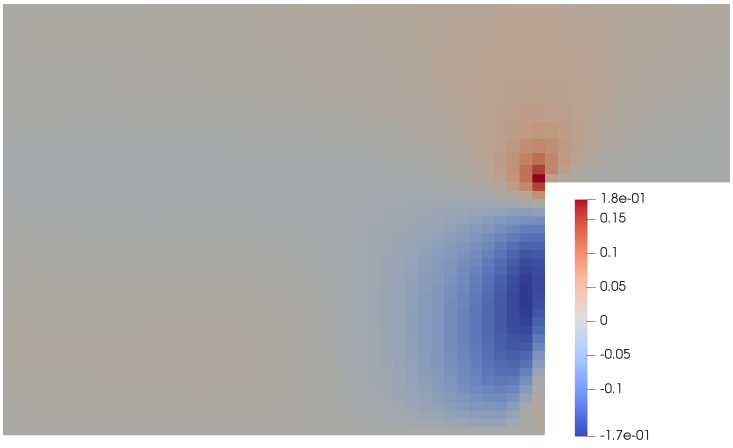

Figure 4.20: v component of the velocity [m/s] near end of a cavity at $t = T$. It can be observed that the flow splits. $Re = 6 \times 10^5$.

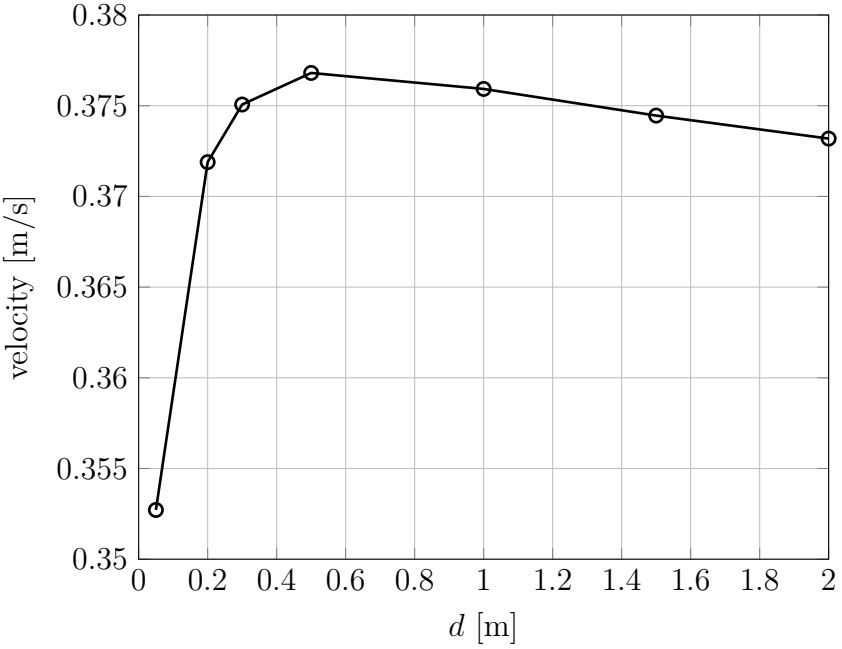

Figure 4.21: Relation between the maximum velocity in the peak above the second cavity and the distance d between the cavities.

produced from the first cavity is transported towards the second one, leading to an increased thickness of the boundary layer as we move in the x-direction.

Coupled problem with shallow cavities

In this second test we simulate the same situation as in the previous single-domain test, choosing a distance between the two shallow cavities $d = 1\,\mathrm{m}$, so that they do not influence each other directly. In addition to this, we couple the free-flow with the simulation of a flow inside a porous-medium that fills the space between the cavities, as shown in Figure 4.23. In this way, we have two domains, Ω_{ff} and Ω_{pm}, that are in contact through the interface Γ_{int}. The considered fluid is always isothermal, single-phase and single-component and gravity is neglected, as in the previous cases.

We want to analyse the differences that the presence of the porous-medium induces in the flow field with respect to the previous case and study how they change as we vary the permeability.

In the domain Ω_{ff} we solve, as before, the RANS equations with the k-ω model, while in the Ω_{pm} we solve the continuity equation for a porous-medium flow (2.66), exploiting the Forchheimer's law (2.68), in which we

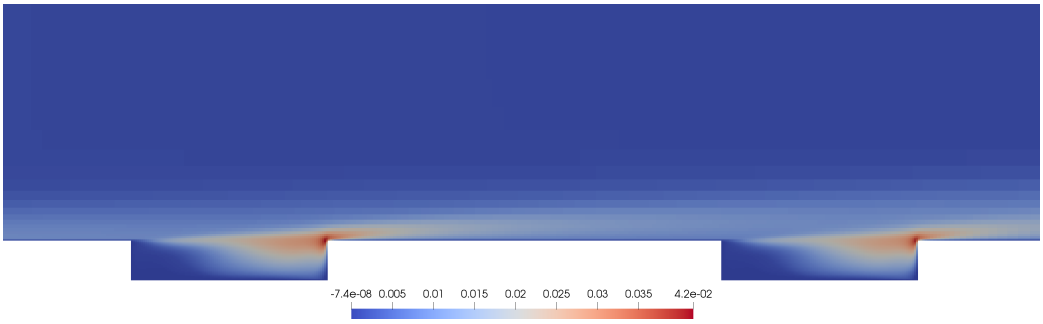

Figure 4.22: Turbulent kinetic energy [m^2/s^2] around the cavities with $d = 1\,m$, at $t = T$. $Re = 6 \times 10^5$.

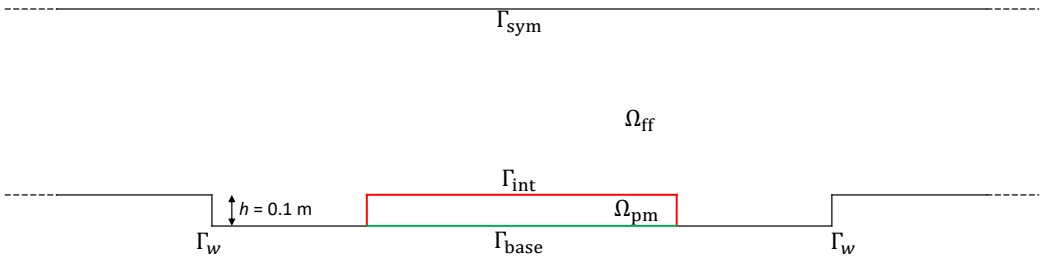

Figure 4.23: Domain change with respect to Figure 4.17 for the coupled problem with shallow cavities. The subdomain Ω_{pm} is introduced between the cavities.

neglect the gravity contribution. We use the same initial and boundary conditions we used before, but this time we have to impose, in addition, the coupling conditions described in Section 2.3 on the interface Γ_{int} and no-flow conditions on the boundary Γ_{base}, fixing the normal flux, i.e. the v component of the velocity to zero. We employ the same time discretization and the same grid we used before in Ω_{ff} and we extend it in Ω_{pm} in a conforming way.

As we did in the previous case, we compare in Figure 4.24 the profiles of the u component of the velocity at the position $y = h$ for several values of permeability. For values of K lower than $10^{-8}\,m^2$, the porous-medium results to be almost impermeable, or at least the flow field in Ω_{ff} is the same that we had in the previous test considering only the free-flow and impervious boundaries. The maximum velocities in the corner of the porous-medium are some orders of magnitude lower than those in the cavities (see Figure 4.25).

Starting from $K = 3.1 \times 10^{-8}\,m^2$, we observe some changes in the velocity profile and increasing the permeability those changes are enhanced. The increase of the maximum velocity in correspondence of the first cavity can be due to the reduction of the *wall* behaviour of the porous-medium. The flow

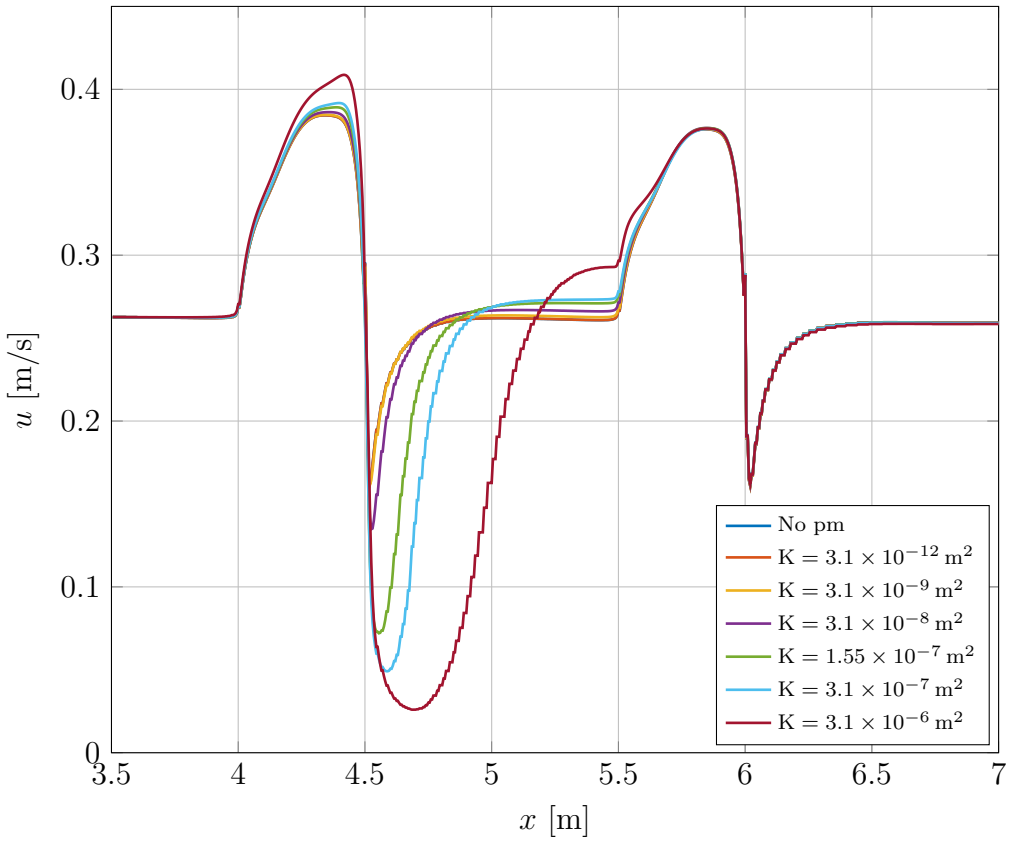

Figure 4.24: Profiles of the u component of the velocity at $y = h$ in the coupled problem with shallow cavities for several values of permeability, at $t = T$. $Re = 6 \times 10^5$.

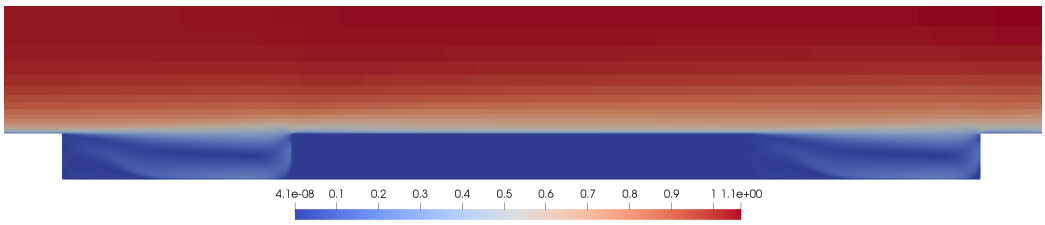

Figure 4.25: Magnitude of the velocity field [m/s] in the coupled problem with shallow cavities, with K = 3.1×10^{-9} m^2, at $t = T$. $Re = 6 \times 10^5$.

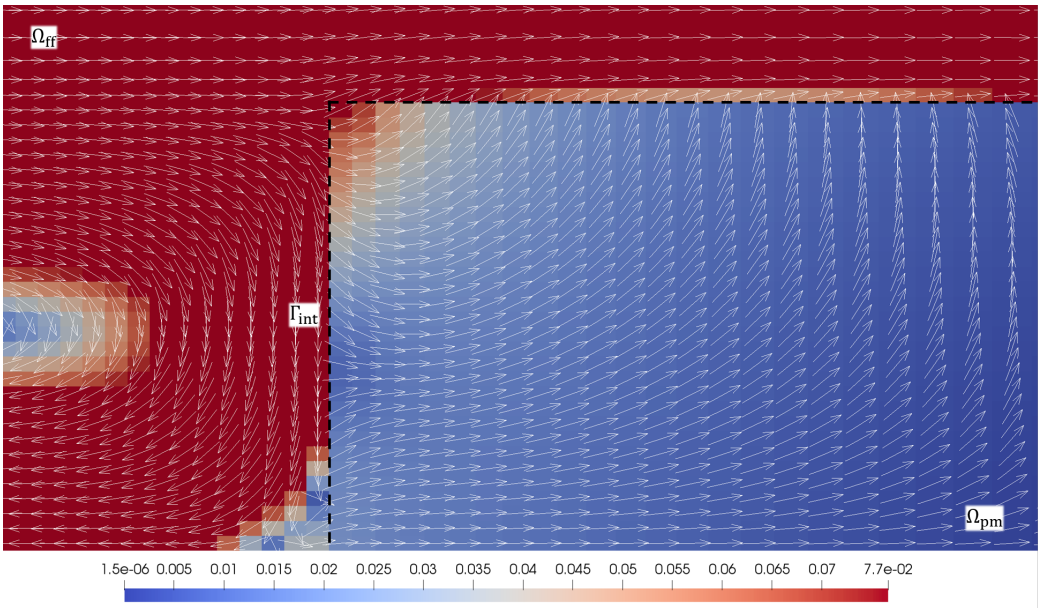

Figure 4.26: Velocity field [m/s] near the end of the first cavity in the coupled problem with shallow cavities, with $\mathrm{K} = 3.1 \times 10^{-7}\,\mathrm{m}^2$, at $t = T$. A portion of fluid enters into the porous-medium. The dashed line is the interface Γ_{int}. The length of the arrows is not scaled. $Re = 6 \times 10^5$.

is allowed to reach higher velocities and it is less forced to reduce its velocity because a more relevant amount of fluid enters into the porous-medium (see Figure 4.26). Then this flow exits from the top of Ω_{pm} within approximately the first 20 cm; in the case of high permeability, this region with a peak in the v component of the velocity spreads and moves a bit to the right, as it can be seen in Figure 4.27.

After the distance d_{rec}, the value of the velocity observed before the effect of the cavity is recovered and the boundary layer is restored. With high values of permeability this value is higher than the one with low permeabilities; this is due to the Beavers-Joseph-Saffman condition (2.77) at the interface, which allows more slip as the permeability increases. Eventually the behaviour around the second cavity is approximately the same with all the permeabilities. There is a portion of fluid that goes back inside the porous-medium, but, since it comes from the corner eddy, the values involved are lower compared to what happens in the first cavity, so this effect does not seem to influence the free-flow notably (see Figure 4.28).

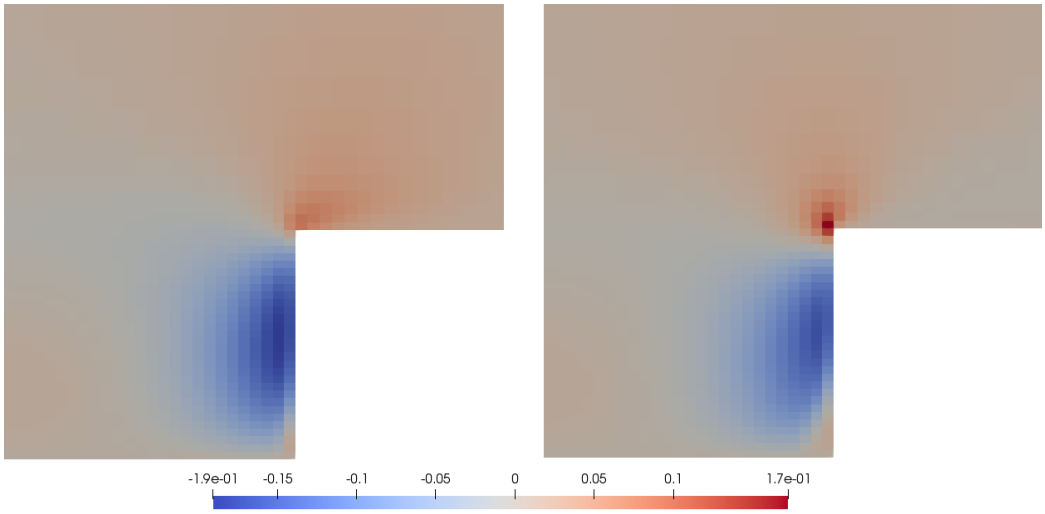

Figure 4.27: v component of the velocity [m/s] near the end of the first cavity in the free-flow domain Ω_{ff}, $t = T$. $\text{K} = 3.1 \times 10^{-7}\,\text{m}^2$ on the left and $\text{K} = 3.1 \times 10^{-9}\,\text{m}^2$ on the right. $Re = 6 \times 10^5$.

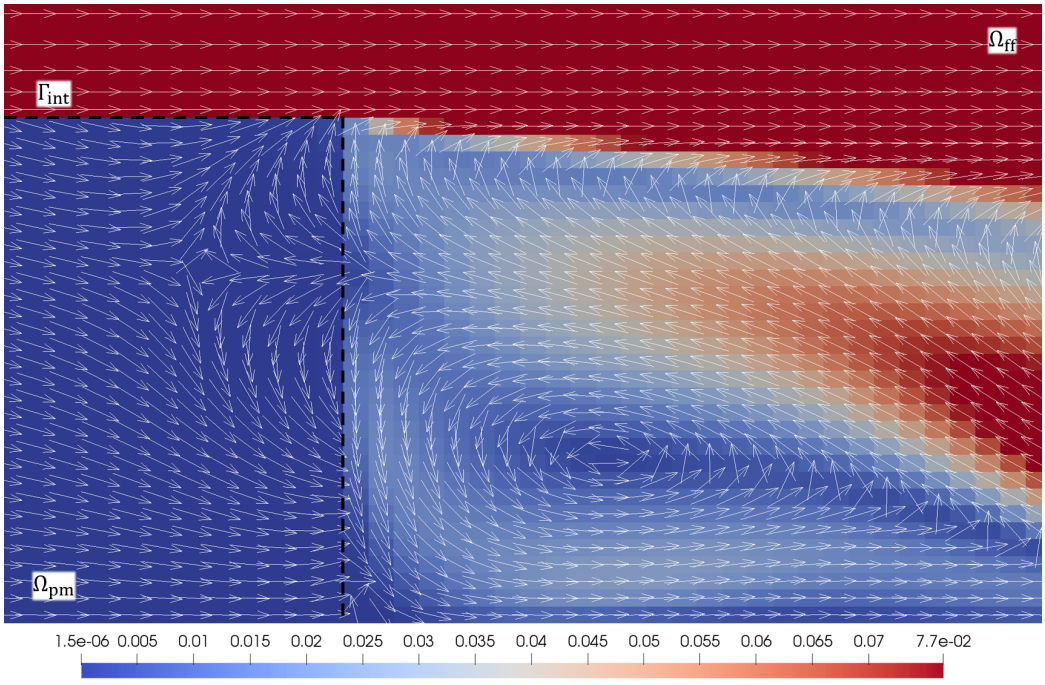

Figure 4.28: Velocity field [m/s] near the beginning of the second cavity in the coupled problem with shallow cavities, with $\text{K} = 3.1 \times 10^{-7}\,\text{m}^2$ at $t = T$. Some flow enters into the porous medium. The dashed line is the interface Γ_{int}. The length of the arrows is not scaled. $Re = 6 \times 10^5$.

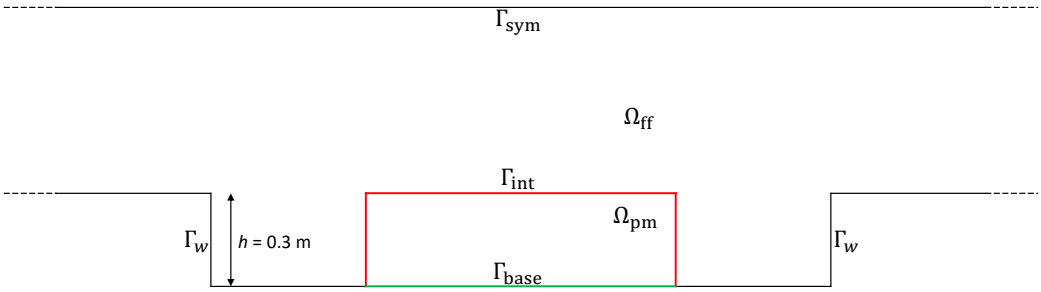

Figure 4.29: Domain change with respect to Figure 4.17 for the coupled problem with deep cavities. The subdomain Ω_{pm} is introduced between the cavities.

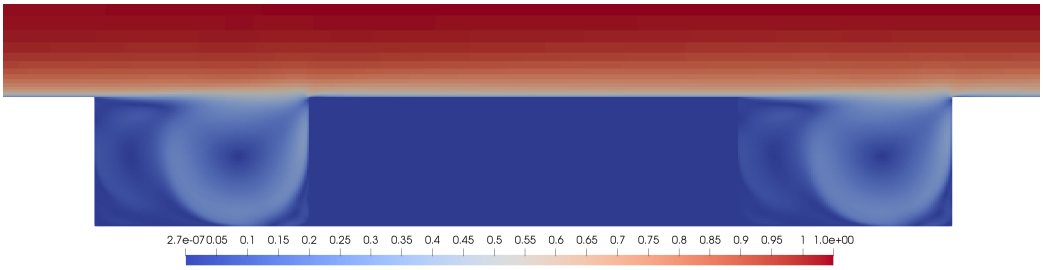

Figure 4.30: Magnitude of the velocity field [m/s] in the coupled problem with deep cavities, with $\mathrm{K} = 3.1 \times 10^{-9}\,\mathrm{m}^2$, at $t = T$. $Re = 6 \times 10^5$.

Coupled problem with deep cavities

We repeat the previous test considering the domain with deep cavities depicted in Figure 4.29, such that $h = 0.3\,\mathrm{m}$. The grid is extended uniformly. Using the same model and the same boundary and interface conditions, we want to see if, with a different height of the cavities, the porous-medium flow affects differently the flow field. As before, we vary the permeability of the porous-medium in order to understand which is the threshold value between a permeable and an almost impermeable behaviour.

In Figure 4.30, we can see the magnitude of the velocity field in the region around the cavities and the porous-medium. As before, the two cavities show the same recirculation pattern, but it is different from the one that is generated when the cavities are shallow (see Figure 4.25), because of the different size of the domain. Here, there is a bigger circular eddy touching the right boundary of the cavity and some smaller eddies in the left region of the cavity.

In Figure 4.31, we compare the profiles of the u component of the velocity at the position $y = h$, for several values of permeability. With respect

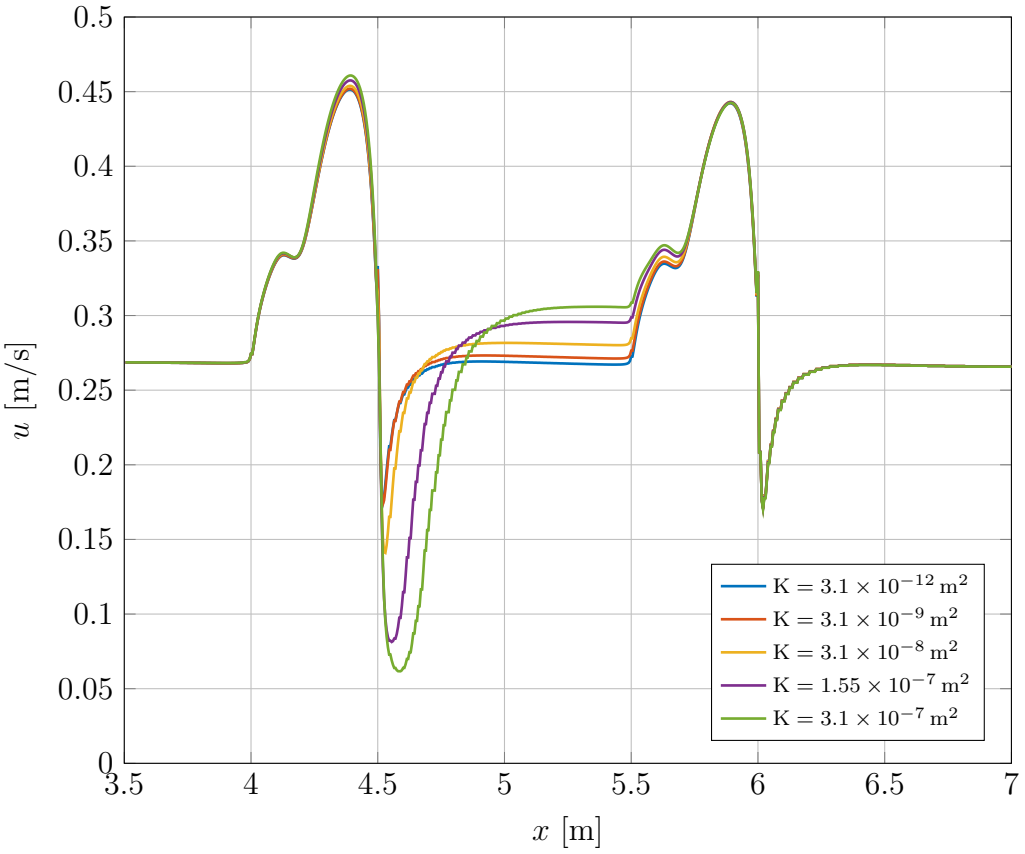

Figure 4.31: Profiles of the u component of the velocity at $y = h$ in the coupled problem with deep cavities for several values of permeability, at $t = T$. $Re = 6 \times 10^5$.

to Figure 4.24, we observe a different profile in correspondence of the cavities, because of the different recirculation pattern inside them. As before, we notice that, as the permeability increases, the maximum velocity in correspondence of the first cavity increases, the minimum velocity above the beginning of the porous-medium decreases and the velocity above the end of the porous-medium increases. The threshold value for the permeability of approximately $10^{-8}\,\mathrm{m}^2$ seems to be still valid. With respect to the previous test case, we observe that the value of the velocity before the second cavity, for $5 < x < 5.5$, increases faster. Indeed, when $\mathrm{K} = 3.1 \times 10^{-7}\,\mathrm{m}^2$, it is greater than $0.3\,\mathrm{m/s}$, while in the previous geometry, for the same value of permeability, it was approximately $0.27\,\mathrm{m/s}$. This fact could be due to a smaller amount of fluid exchanged with the porous-medium, or at least to differently distributed exchanges along the interface.

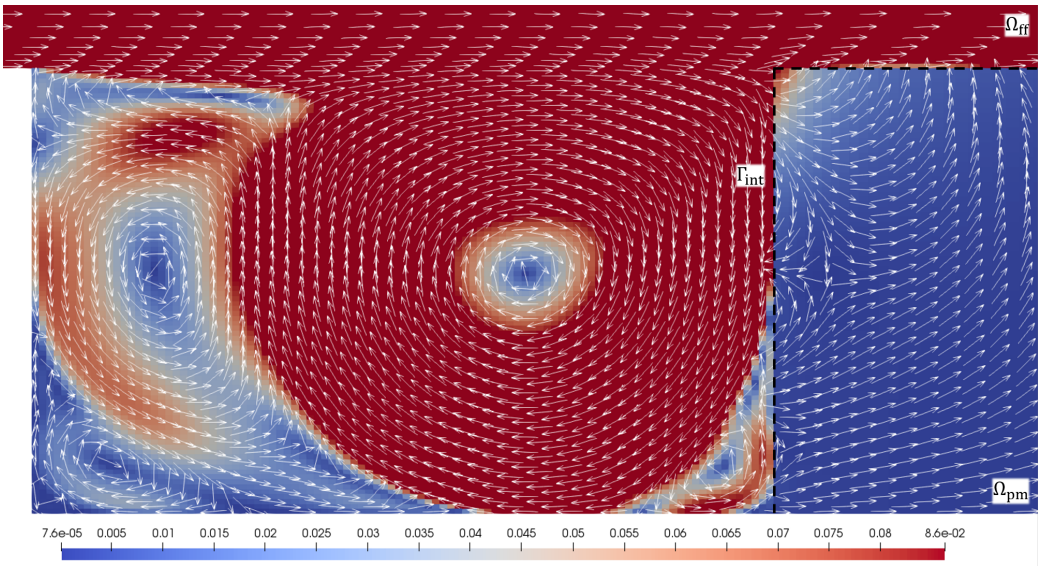

Figure 4.32: Velocity field [m/s] around the first cavity in the coupled problem with deep cavities, with $\mathrm{K} = 3.1 \times 10^{-7}\,\mathrm{m}^2$, at $t = T$. The dashed line is the interface Γ_{int}. The length of the arrows is not scaled. $Re = 6 \times 10^5$.

In Figure 4.32 we see the velocity field around the first cavity. A portion of flow enters into the porous-medium near its upper-left corner, then it exits from above as in the case of shallow cavities. The section of Γ_{int} such that $y < h/2$ is characterized by a more complex behaviour for what concerns the flow direction. In fact, because of the multiple eddies, the exchange of fluid occurs both from the free-flow region to the porous-medium and vice versa. In Figure 4.33 we see the velocity field around the second cavity. Here, the flow pattern across the interface is analogous to the one in the case of shallow cavities, depicted in Figure 4.28.

It is interesting to evaluate the mass flow rate $\dot{m}$ across the interface between the free-flow and the porous-medium flow. In particular, we compute, at $t = T$, the amount of mass that goes from the free-flow region to the porous-medium per unit of time as:

$$\dot{m} = \int_{\Gamma_{\mathrm{int}}} \max\{\varrho \mathbf{v} \cdot \mathbf{n}, 0\}\, dA, \tag{4.28}$$

where $\mathbf{n}$ is the outward unit vector normal to $\partial\Omega_{\mathrm{ff}}$. Notice that, being the fluid incompressible and imposing no-flow conditions on the lower boundary of the porous-medium Γ_{base}, the net mass flow rate across Γ_{int} is zero.

In Figure 4.34 we compare the values in the two cases of shallow and deep cavities. In both the situations we observe a relevant increase of the mass

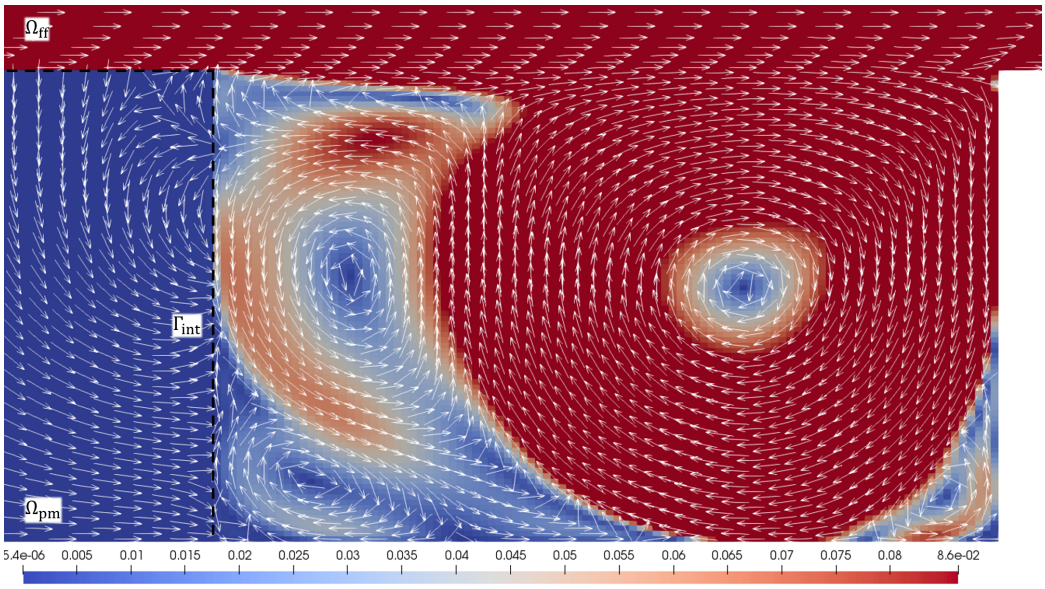

Figure 4.33: Velocity field [m/s] around the second cavity in the coupled problem with deep cavities, with $\mathrm{K} = 3.1 \times 10^{-7}\,\mathrm{m}^2$ at $t = T$. The dashed line is the interface Γ_{int}. The length of the arrows is not scaled. $Re = 6 \times 10^5$.

flow rate when the permeability is approximately greater than $10^{-8}\,\mathrm{m}^2$, so the same threshold value that we found in the previous analysis. $\dot{m}$ is always greater in the case of deep cavities than in the case of shallow cavities. In Table 4.5 we compare the values and we compute the ratio $\dot{m}_{\mathrm{deep}}/\dot{m}_{\mathrm{shallow}}$, that results to be between 1.3 and 1.5 for every value of permeability. The ratio between the measure of the Γ_{int} is $1.6/1.2 = 1.\bar{3}$, so it is likely that the difference in the mass flow rate between the two cases is simply due to the different surface of the interface.

4.3.2 Obstacle problem

In this subsection we study the behaviour of a turbulent flow in a channel with a porous obstacle of height $h = 0.1\,\mathrm{m}$ on the lower boundary, as depicted in Figure 4.35. We want to analyse how the porous-medium affects the flow field, considering several possible values of permeability. We solve the RANS equations (2.22)-(2.23) with the k-ω turbulence model (2.47)-(2.49) in the subdomain Ω_{ff} and the continuity equation for a porous-medium flow (2.66), exploiting the Forchheimer's law (2.68), in the subdomain Ω_{pm}. We neglect the gravity contributions. We impose inflow boundary conditions on the left

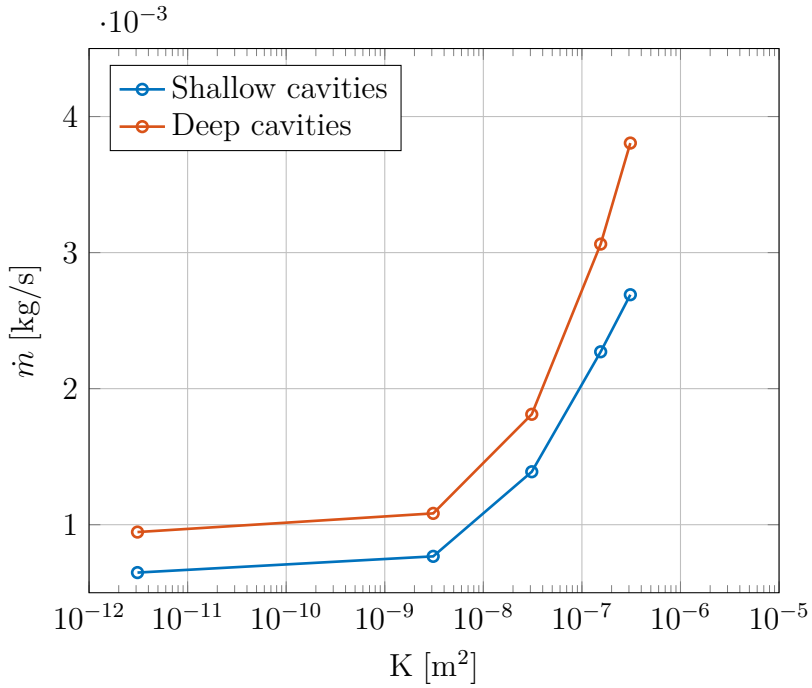

Figure 4.34: Mass flow rate from the free-flow region to the porous-medium across Γ_{int}, depending on the permeability.

K [m^2]	$\dot{m}_{\text{deep}}$ [kg/s]	$\dot{m}_{\text{shallow}}$ [kg/s]	$\dot{m}_{\text{deep}}/\dot{m}_{\text{shallow}}$
3.1×10^{-12}	9.455×10^{-4}	6.401×10^{-4}	1.477
3.1×10^{-9}	1.083×10^{-3}	7.673×10^{-4}	1.411
3.1×10^{-8}	1.812×10^{-3}	1.389×10^{-3}	1.304
1.55×10^{-7}	3.063×10^{-3}	2.271×10^{-3}	1.349
3.1×10^{-7}	3.805×10^{-3}	2.690×10^{-3}	1.414

Table 4.5: Mass flow rate from the free-flow region to the porous-medium across Γ_{int}, depending on the permeability.

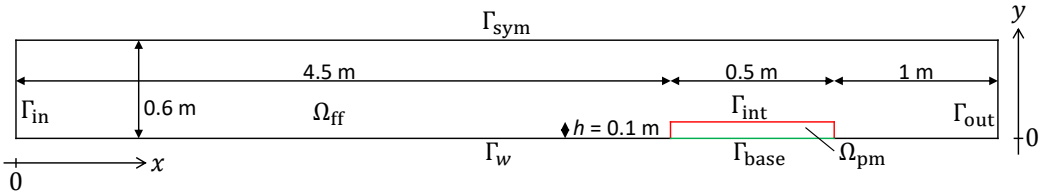

Figure 4.35: Domain for the obstacle problem.

boundary Γ_{in}:

$$\mathbf{v} = \mathbf{v}_{\text{in}} = [u_{\text{in}}, 0]^{\text{T}}, \quad u_{\text{in}} = 1\,\text{m/s}, \tag{4.29}$$

no-slip boundary conditions on the lower boundary Γ_w, symmetry boundary conditions on the upper boundary Γ_{sym} and outflow boundary conditions on the right boundary Γ_{out}, fixing the value of the pressure:

$$p = p_{\text{ext}} = 1.1 \times 10^5\,\text{Pa}. \tag{4.30}$$

On the interface Γ_{int}, we impose the coupling conditions described in Section 2.3, while on the boundary Γ_{base} we impose no-flow conditions. The density of the fluid is $\varrho = 1\,\text{kg/m}^3$ and its kinematic viscosity is $\nu = 10^{-5}\,\text{m}^2/\text{s}$, so that the Reynolds number is $Re = 6 \times 10^5$. We start considering a permeability $\text{K} = 10^{-9}\,\text{m}^2$. We simulate the time interval $(0, T)$, with $T = 30\,\text{s}$, such that the solution reaches an equilibrium, and we use an initial time-step $\Delta t = 10^{-4}\,\text{s}$. As initial conditions we set:

$$\mathbf{v} = [u_{\text{init}}, 0]^{\text{T}} \quad \forall \mathbf{x} \in \Omega_{\text{ff}}, \quad u_{\text{init}} = \begin{cases} u_{\text{in}} & \text{if } x \leq 0 \vee x > 1\,\text{m} \\ \frac{7}{6} u_{\text{in}} & \text{if } 0 \leq x \leq 1\,\text{m} \end{cases}, \tag{4.31}$$

$$p = p_{\text{ext}} \quad \forall \mathbf{x} \in \Omega_{\text{ff}} \cup \Omega_{\text{pm}}, \tag{4.32}$$

$$k = k_{\text{in}},\ \omega = \omega_{\text{in}} \quad \forall \mathbf{x} \in \Omega_{\text{ff}}. \tag{4.33}$$

The factor 7/6 ensures that the flow rate is uniform along the channel. Performing a sensitivity analysis, we choose a grid made of 280×82 cells, employing gradings up to 1.2 in order ho have refined cells near the walls. The size of the cells in the region around the upper-left corner of the obstacle shows to affect significantly the solution. Indeed, looking at Figure 4.36, we can see how the pattern of the velocity field changes for three different grids.

In Figure 4.37, we see the velocity field near the beginning of the porous obstacle. At the frontal face of the porous-medium, corresponding to $x = 4.5\,\text{m}$, a small portion of the main flow enters into the obstacle, while the left amount of fluid recirculates near the bottom of the channel. At the corner of the porous-medium, the flow is deflected towards an higher region, so that, above the upper surface of the obstacle, a recirculation is generated and the velocity at the porous wall is negative. In Figure 4.38, we can see, instead, the velocity field near the end of the obstacle. The velocity pattern is analogous to the one generated by a backward facing step, as studied in Section 4.2. There is a small amount of fluid exiting from the porous-medium, but it does not seem to affect the eddies in the region after the obstacle.

Now we analyse how a change in the permeability of the porous obstacle influences the flow field, considering a range from $10^{-11}\,\text{m}^2$ to $10^{-8}\,\text{m}^2$.

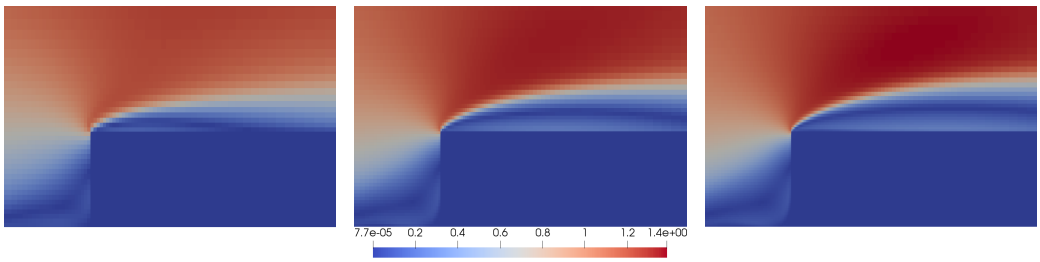

(a) (b) (c)

Figure 4.36: Magnitude of the velocity field [m/s] near the beginning of the porous-medium, at $t = T$, considering a grid of (a) 207×52 cells, with minimum cell size at the obstacle corner equal to $3.3\,\text{mm} \times 4.4\,\text{mm}$, (b) 242×68 cells, with minimum cell size at the obstacle corner equal to $2\,\text{mm} \times 2.7\,\text{mm}$, (c) 280×82 cells, with minimum cell size at the obstacle corner equal to $1.4\,\text{mm} \times 2\,\text{mm}$. $Re = 6 \times 10^5$.

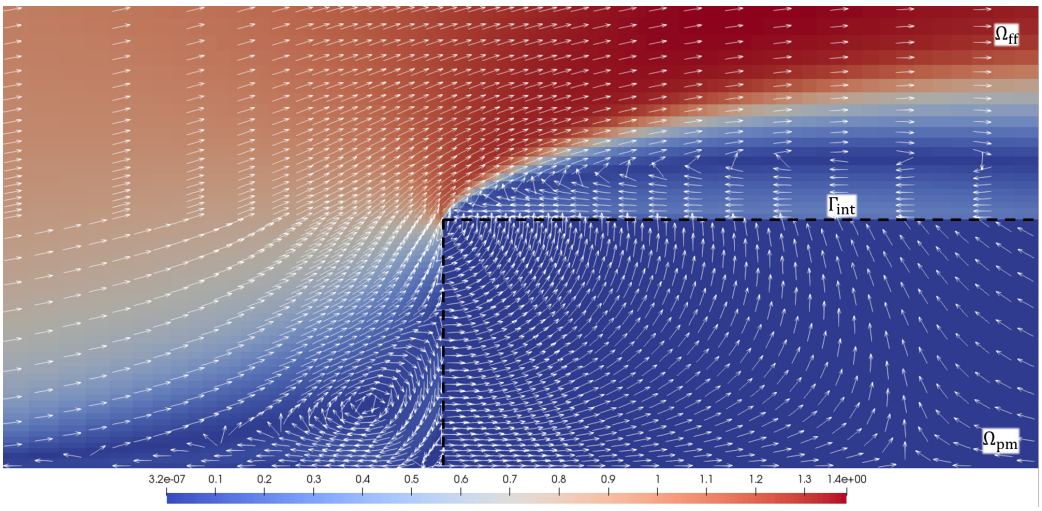

Figure 4.37: Velocity field [m/s] near the beginning of the obstacle in the obstacle problem, with $\text{K} = 10^{-9}\,\text{m}^2$ at $t = T$. The dashed line is the interface. The length of the arrows is not scaled. $Re = 6 \times 10^5$.

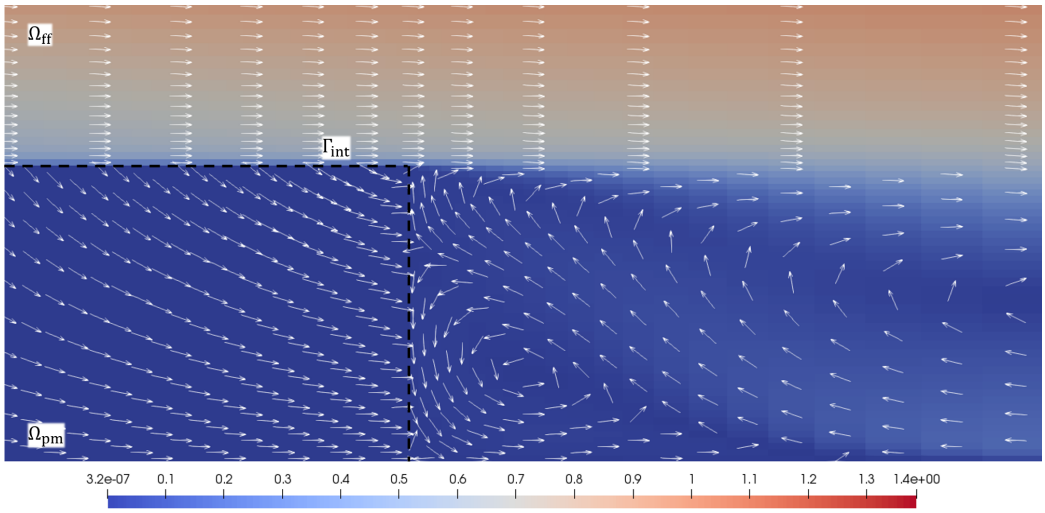

Figure 4.38: Velocity field [m/s] near the end of the obstacle in the obstacle problem, with $\mathrm{K} = 10^{-9}\,\mathrm{m}^2$ at $t = T$. The dashed line is the interface. The length of the arrows is not scaled. $Re = 6 \times 10^5$.

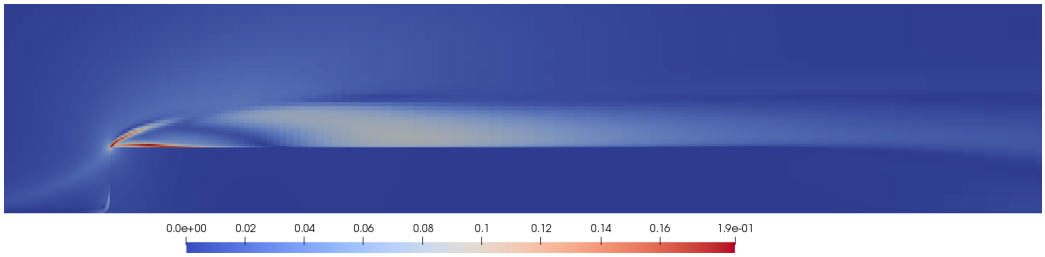

Figure 4.39: Magnitude of the difference of the velocity field [m/s] in the obstacle problem between the cases $\mathrm{K} = 10^{-8}\,\mathrm{m}^2$ and $\mathrm{K} = 10^{-11}\,\mathrm{m}^2$.

In Figure 4.39 we see the magnitude of the difference between the velocity field when $\mathrm{K} = 10^{-8}\,\mathrm{m}^2$ and $\mathrm{K} = 10^{-11}\,\mathrm{m}^2$. We observe that the most relevant differences are near the beginning of the obstacle, arising from the upper-left corner. Near the end of the obstacle, instead, the flow field is approximately the same. In Figure 4.39 we observe the two components of the same velocity difference, at the beginning of the porous-medium domain. The area around the upper-left corner is the one with the greatest difference. In particular, when $\mathrm{K} = 10^{-8}\,\mathrm{m}^2$, both components of the velocity present higher values, so that more fluid coming from the free-flow region "crosses" the corner of the porous obstacle and exits from above. In Figure 4.41, the profiles of the u component of the velocity along the section at $y = h$, i.e. above the obstacle, are reported for different values of permeability. We observe negative values

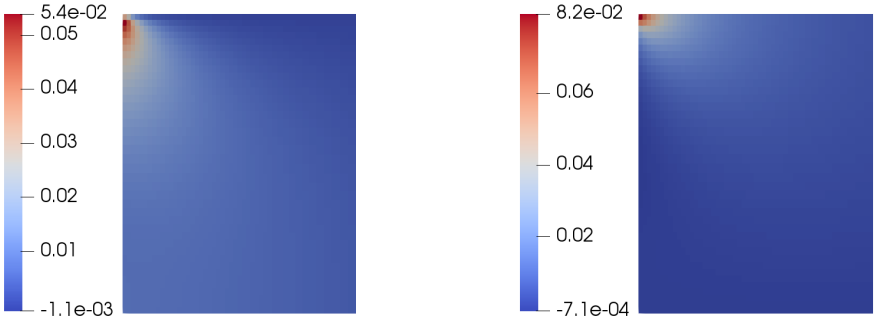

(a) u component (b) v component

Figure 4.40: Components of the difference $\mathbf{v}_8 - \mathbf{v}_{11}$ [m/s] at the beginning of the porous obstacle, where $\mathbf{v}_n$ is the velocity field computed considering a permeability $\mathrm{K} = 10^{-n}$ m^2.

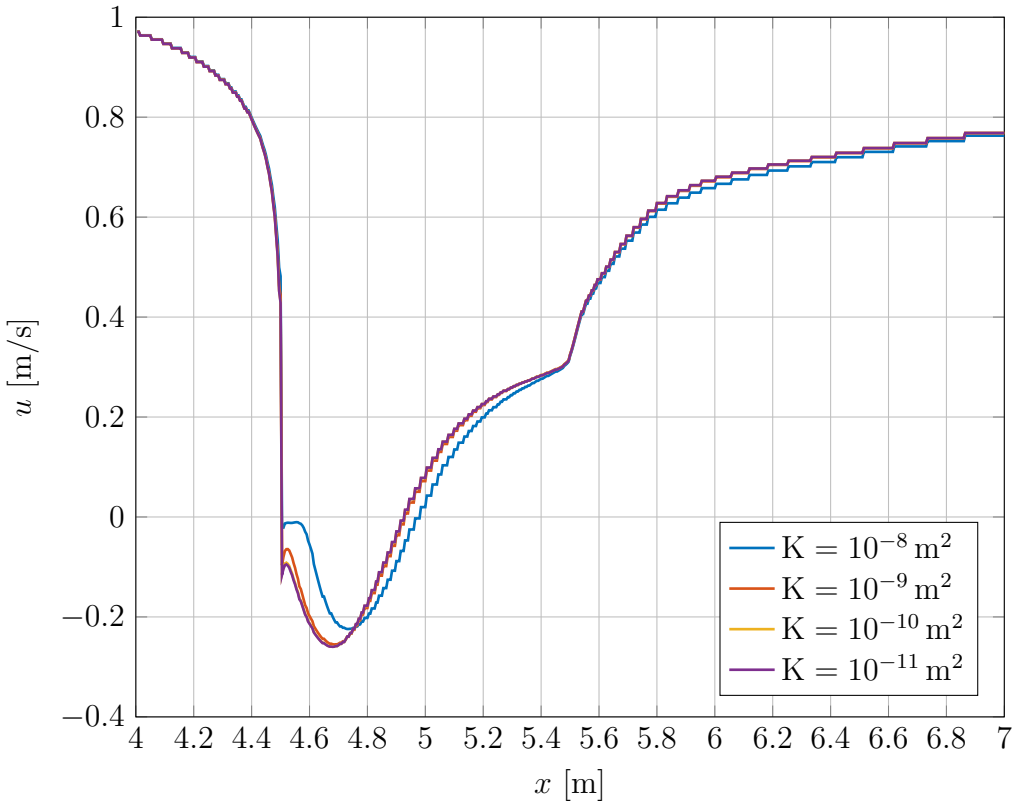

Figure 4.41: Profiles of the u component of the velocity at $y = h$, i.e. above the porous obstacle, which occupies the region $4.5 < x < 5.5$. $t = T$, $Re = 6 \times 10^5$.

starting from $x = 4.5$, corresponding to the recirculation above the porous-medium. As K increases, the minimum value of u and the reattachment length, i.e. the point where the velocities becomes positive, increase. It is likely that, as a more relevant amount of fluid crosses the corner of the porous-medium, the area where the flow is deflected is extended. As a result, the recirculation il slightly shifted in the flow direction, with the consequent increase of the reattachment length.

Chapter 5

Conclusions and outlook

5.1 Conclusions

In this thesis we have dealt with the study of the TVD methods for the approximation of the convective term in the momentum equation of the Navier-Stokes equations and of the RANS equations, within a finite volumes framework. We implemented them for the simulation of coupled free-flow and porous-medium flow models, with the aim of improving the results obtained by standard first order upwind schemes by reducing numerical dissipation in the solution, while guaranteeing stability and avoiding the creation of unphysical oscillations.

In all the tests that have been performed, we have experienced an increased accuracy of the solution with respect to those obtained when using the first order upwind method. The spatial convergence rates in the tests with analytical solution were between 1.5 and 2 in many cases, while with the upwind method we had always a first order convergence. The differences were more relevant at large Reynold numbers (10^3 with respect to 1), because of the increased importance of the convective term with respect to the diffusive one. For what concerns the validation of the code for turbulent flows, in the backward facing step test we have obtained, using the Van Leer flux limiter, a satisfying agreement with validated numerical results from the CFL3D code and experimental data. Moreover, employing a BDF2 scheme for the temporal discretization, we can guarantee a high order discretization both in space and in time, thus allowing a more accurate study of transient phenomena.

With this tool, we have studied a coupled model consisting of a free-flow and a porous-medium flow, focusing in particular on the effects that a rough interface, with cavities or porous obstacles, has on the flow field.

At first, we have considered only the free-flow and we have studied how the velocity is affected by the presence of two cavities at the interface. In particular, we have investigated which is the distance between the cavities such that the variation in the flow field due to the first cavity does not influence the behaviour around the second one significantly. We have obtained that, for cavities 0.5 m long, after a distance equal to one cavity the flow field has recovered the undisturbed configuration it had before the first cavity. However, each cavity introduces an increase in the turbulent kinetic energy, that accelerates the growth of the turbulent boundary layer.

Then, we have chosen a distance such that the two cavities do not influence each other and we have placed a porous-medium between them, in order to analyse how its presence affects the flow field. We have observed that, for values of permeability greater than $10^{-8}\,\mathrm{m}^2$, the flow field in the free-flow shows noticeable differences when compared to a case with impermeable boundaries, both in the case of the shallow cavities and deep cavities. In particular, not only the fact that the flow can enter into the porous-medium has an effect, but also the Beaver-Joseph-Saffman slip condition imposed at the interface between the two subdomains affects the flow dynamics. The presence of eddies in the cavities influences the flow in the porous-medium, because in correspondence of the corner it can enter also from a direction opposite to the one of the main flow. However, when this happens, the values of the velocity are relatively small and thus this behaviour does not affect the free-flow as it happens when the flow enters the porous-medium at the end of a cavity. We have evaluated the mass flow rate from the free-flow region to the porous-medium and we have noticed a relevant increase for values of permeability greater than $10^{-8}\,\mathrm{m}^2$. Comparing the cases of shallow and deep cavities, the mass flow rate has shown to be proportional to the measure of the interface.

At last, we have considered a flow in a channel with a porous obstacles on the lower boundary. We have observed that the porous-medium flow influences the free-flow only at the frontal face of the obstacle, where the flow is stopped by the porous medium, while at the backward face the behaviour remains the same independently of the permeability.

5.2 Future developments

Future developments to this work can be devoted to the investigation of more complex models, involving multiphase, multi-component and non-isothermal models. Exploiting the accuracy of high-resolution methods, a more reliable prediction of the evaporation rate from a wet soil could be performed.

Moreover, it could be interesting to study other types of *rough* interfaces, for example to see if a smooth interface described by a sinusoidal function could behave differently with respect to those we have analysed.

In this work the TVD methods have been adopted only in the momentum equation, but, in particular with non-isothermal models with non-constant density, from the numerical point of view it could be important to analyse their application to the continuity equation as well.

From the point of view of the coupling, the interface conditions could be adapted in order to employ other finite volumes discretization schemes in the porous-medium, including, for example, a Multi Point Flux Approximation (MPFA). Moreover, iterative algorithms to decouple the two subdomains could be taken into account and compared to the monolithic approach we have adopted.

Within the DuMu^{x} framework a possibility to improve the efficiency of the simulations could be to employ an adaptive algorithm in order to refine the grid only where it is useful. This approach can lead to non-conforming meshes containing hanging nodes, thus a challenge would be the application of the TVD scheme to this case. Moreover, a parallelization of the code would be beneficial for the computational time, but the extended stencil of high order methods requires attention whilst decomposing the domain.

Appendix A

Space convergence

We report here some more convergence examples in addition to the Sin-Cos presented in Subsection 4.1.1.

A.1 1D test

We solve the equations (4.2)–(4.3) over a one-dimensional unit domain $\Omega = (0, 1)$, with the following source terms:

$$h(x) = 6x^2, \tag{A.1}$$

$$f(x) = 12x^5 - 24\nu x - \frac{2}{\varrho}, \tag{A.2}$$

so that, choosing $\varrho = 1$, the analytical solution, depicted in Figure A.1, is given by

$$u_{\text{ex}}(x) = 2x^3, \tag{A.3}$$

$$p_{\text{ex}}(x) = 2 - 2x. \tag{A.4}$$

Dirichlet boundary conditions for the velocity are applied on the whole boundary $\partial\Omega$ using the exact solution. The pressure is fixed at one point in order to match the exact solution (A.4).

The problem is solved over a sequence of eight uniform grids, starting from 4 cells and each time halving their size. Both the cases of $\nu = 1$ and $\nu = 10^{-3}$ are considered, that correspond respectively to $Re = 1$ and $Re = 10^3$. In Figure A.2 the computed errors are reported as functions of the number of cells, while in Table A.1 we can compare directly the convergence orders for the different differencing schemes.

In this test, at $Re = 1$, all the methods behave similarly, as we can see in Table A.1a, with the second order convergence for the velocity also using the

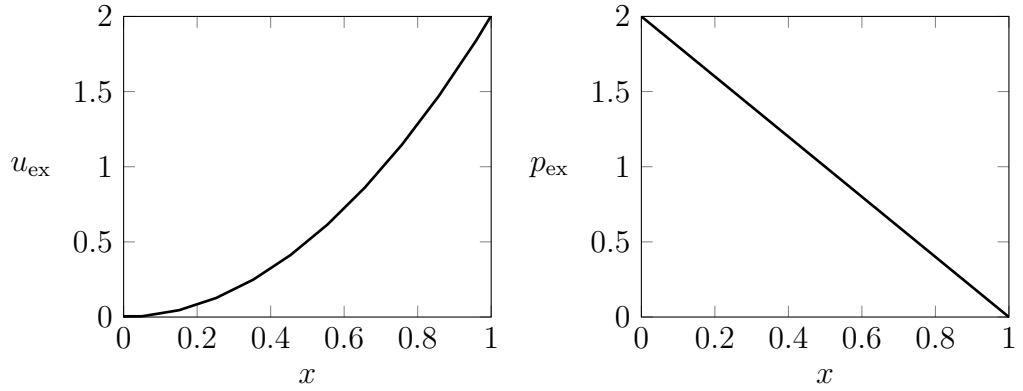

Figure A.1: Exact solution of the 1D test (A.3)–(A.4). On the left the velocity field, on the right the pressure field.

	Upwind	Min-Mod	Van Leer
p	0.985	1.000	0.990
u	1.985	1.996	1.996

(a) $Re = 1$

	Upwind	Min-Mod	Van Leer
p	0.852	1.501	2.172
u	1.318	2.274	2.356

(b) $Re = 10^3$

Table A.1: Convergence orders with for the 1D test. They are computed considering the last two refinements of the grid.

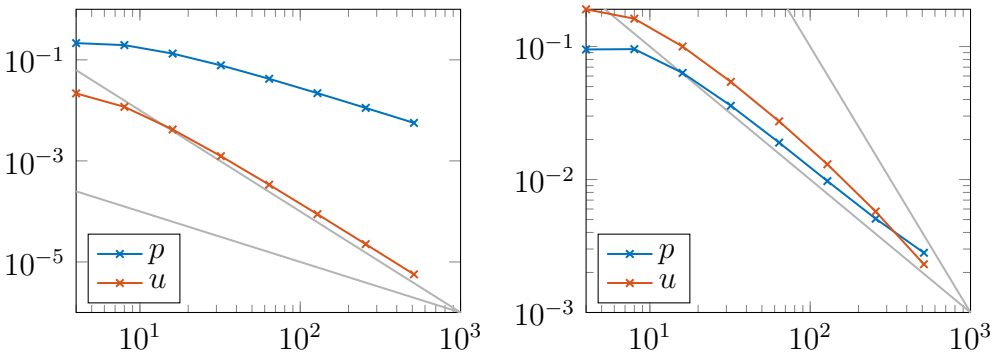

(a) Upwind, $Re = 1$

(b) Upwind, $Re = 10^3$

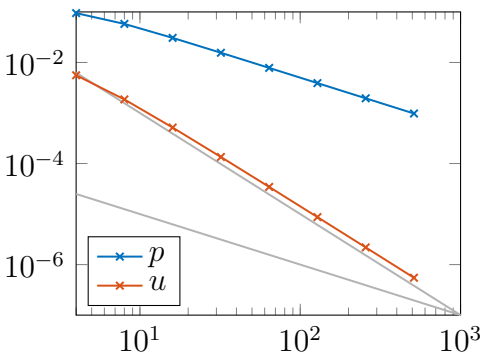

(c) Min-Mod, $Re = 1$

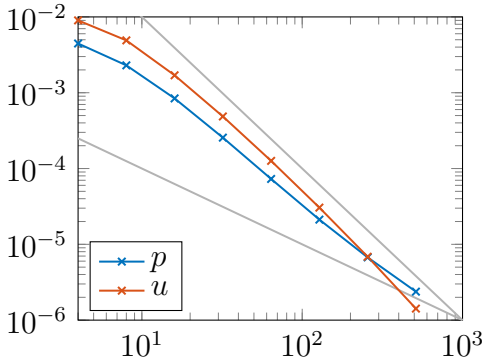

(d) Min-Mod, $Re = 10^3$

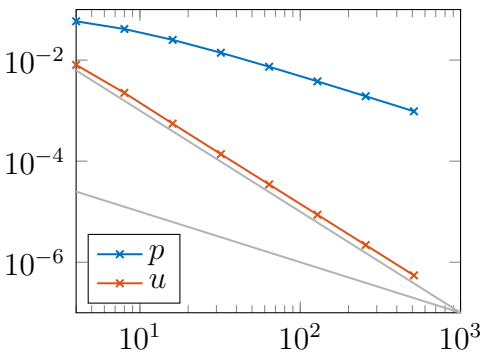

(e) Van Leer, $Re = 1$

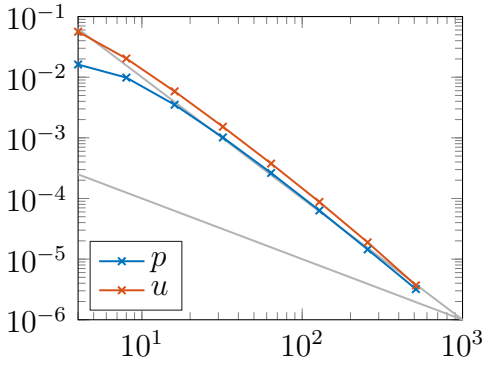

(f) Van Leer, $Re = 10^3$

Figure A.2: $L^2(\Omega)$ norm of the errors for the 1D test depending on the number of cells in the grid. The grey lines are the reference lines parallel to a first order convergence (the lower one) and a second order convergence (the upper one).

upwind method. Probably, in this one-dimensional configuration, the second order diffusive term is dominating. From Table A.1b we observe instead that, at $Re = 10^3$, the TVD methods keep the second order convergence for the velocity and increase the rate also for the pressure, while the upwind method presents decreased convergence orders with respect to the case at $Re = 1$. With the finest grid we observe from Figure A.2 that with the TVD methods the errors are three orders of magnitude lower than with the upwind method.

A.2 Kovasznay test

We solve the equations (4.2)–(4.3) over a two-dimensional domain $\Omega = (-0.5, 2) \times (-0.5, 1.5)$, without any source term, so that, choosing $\varrho = 1$, the analytical solution, depicted in Figure A.3, is given by

$$u_{\text{ex}}(x, y) = 1 - e^{\lambda x} \cos(2\pi y), \tag{A.5}$$

$$v_{\text{ex}}(x, y) = \frac{\lambda}{2\pi} e^{\lambda x} \sin(2\pi y), \tag{A.6}$$

$$p_{\text{ex}}(x, y) = \frac{1}{2}(1 - e^{2\lambda x}), \tag{A.7}$$

$$\lambda = \frac{1}{2\nu} - \sqrt{\frac{1}{4\nu^2} + 4\pi^2}, \tag{A.8}$$

as reported in [Kov48]. Dirichlet boundary conditions for the velocity are applied on the whole boundary $\partial\Omega$ using the exact solution. The pressure is fixed at one point in order to match the exact solution (A.7).

The problem is solved over a sequence of seven uniform grids, starting from 4×4 cells and each time halving their size. Both the cases of $\nu = 2.5 \times 10^{-2}$ and $\nu = 2.5 \times 10^{-4}$ are considered, that correspond respectively to $Re = 80$ and $Re = 8 \times 10^3$. In Figure A.4 the computed errors are reported as functions of the number of cells, while in Table A.2 we can compare directly the convergence orders for the different differencing schemes.

From Table A.2, we see that in this test the convergence results for $Re = 80$ and $Re = 8 \times 10^3$ are very similar. With the upwind method the convergence orders are always 1, while with the TVD methods we obtain a second order, but only for the velocity. However, observing Figure A.4, the convergence orders for the TVD methods at $Re = 8 \times 10^3$ are increasing in the last four refinements, indicating that further refinements would be needed to reach the asymptotic behaviour.

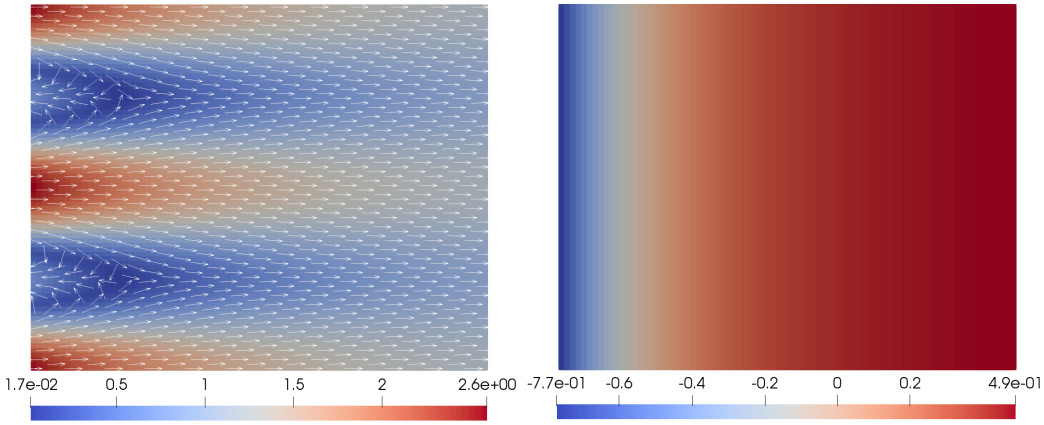

Figure A.3: Exact solution of the Kovasznay test (A.5)–(A.7). On the left the magnitude of the velocity field, on the right the pressure field. The arrows are not scaled.

	Upwind	Min-Mod	Van Leer
p	0.823	0.890	0.902
u	0.928	2.436	2.379
v	0.940	2.422	2.565

(a) $Re = 80$

	Upwind	Min-Mod	Van Leer
p	1.000	0.907	0.865
u	1.030	1.835	1.822
v	0.997	1.960	1.958

(b) $Re = 8 \times 10^3$

Table A.2: Convergence orders with for the Kovasznay test. They are computed considering the last two refinements of the grid.

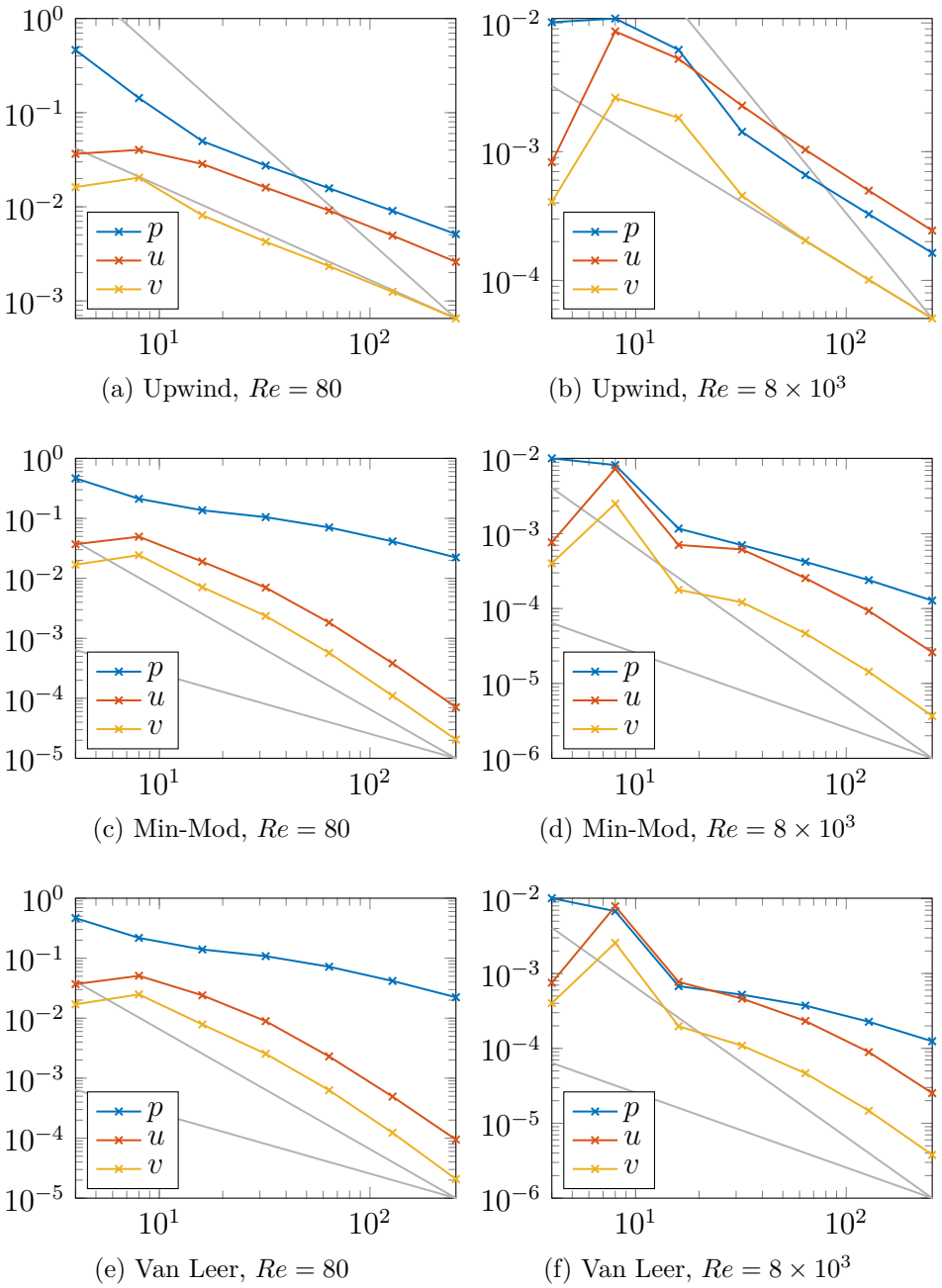

(a) Upwind, $Re = 80$ (b) Upwind, $Re = 8 \times 10^3$

(c) Min-Mod, $Re = 80$ (d) Min-Mod, $Re = 8 \times 10^3$

(e) Van Leer, $Re = 80$ (f) Van Leer, $Re = 8 \times 10^3$

Figure A.4: $L^2(\Omega)$ norm of the errors for the Kovasznay test depending on the number of cells in the grid. The grey lines are the reference lines parallel to a first order convergence (the lower one) and a second order convergence (the upper one).

Bibliography

[All89] G. Allaire. 'Homogenization of the Stokes flow in a connected porous medium'. In: *Asymptotic Analysis* 2 (1989), pp. 203–222.

[ANS09] ANSYS Inc. *ANSYS FLUENT 12.0 - User's Guide*. 12th ed. 2009.

[Bab14] K. I. Baber. 'Coupling free flow and flow in porous media in biological and technical applications: From a simple to a complex interface description'. PhD thesis. Universität Stuttgart, 2014.

[BAM05] M. Berger, M. Aftosmis and S. Muman. 'Analysis of Slope Limiters on Irregular Grids'. In: *43rd AIAA Aerospace Sciences Meeting and Exhibit*. 2005.

[BJ67] G. S. Beavers and D. D. Joseph. 'Boundary conditions at a naturally permeable wall'. In: *Journal of Fluid Mechanics* 30.1 (1967), pp. 197–207.

[Bou77] J. Boussinesq. *Essai sur la théorie des eaux courantes*. Impremerie Nationale, 1877.

[BQQ09] S. Badia, A. Quaini and A. Quarteroni. *Coupling Biot and Navier-Stokes problems for fluid-poroelastic structure interaction*. Technical report. Universitat Politècnica de Catalunya, 2009.

[Bri47] H. C. Brinkman. 'Calculation of the viscous force exerted by a flowing fluid on a dense swarm of particles'. In: *Applied Science Research* 1 (1947), pp. 27–34.

[Bro+18] T. Broecker, W. Elsesser, K. Teuber, I. Özgen, G. Nützmann and R. Hinkelmann. 'High-resolution simulation of free-surface flow and tracer retention over streambeds with ripples'. In: *Limnologica* 68 (2018), pp. 46–58.

[Bru96] C. W. S. Bruner. 'Parallelization of the Euler Equations on Unstructured Grids'. PhD thesis. Virgina Polytechnic Institute and State University, 1996.

[CD13] F. Cimolin and M. Discacciati. 'Navier-Stokes/Forchheimer models for filtration through porous media'. In: *Applied Numerical Mathematics* 72 (2013), pp. 205–224.

[Dah+14] W. Dahmen, T. Gotzen, S. Müller and M. Rom. 'Numerical simulation of transpiration cooling through porous material'. In: *International Journal of Numerical Methods in Fluids* 76.6 (2014), pp. 331–365.

[Dav+14] H. Davarzani, K. Smits, R. M. Tolene and T. Illangasekare. 'Study of the effect of wind speed on evaporation from soil through integrated modeling of the atmospheric boundary layer and shallow subsurface'. In: *Water Resources Research* 50 (2014), pp. 661–680.

[Dav04] P. A. Davidson. *Turbulence - an introduction for scientists and engineers*. Oxford University Press, 2004.

[DBC10] T. Defraeye, B. Blocken and J. Carmeliet. 'CFD analysis of convective heat transfer at the surfaces of a cube immersed in a turbulent boundary layer'. In: *International Journal of Heat and Mass Transfer* 53.1 (2010), pp. 297–308.

[DM03] M. Darwish and F. Moukalled. 'TVD schemes for unstructured grids'. In: *International Journal of Heat and Mass Transfer* 46.4 (2003), pp. 599–611.

[DMQ02] M. Discacciati, E. Miglio and A. Quarteroni. 'Mathematical and numerical models for coupling surface and groundwater flows'. In: *Applied Numerical Mathematics* 43.1–2 (2002), pp. 57–74.

[DQ09] M. Discacciati and A. Quarteroni. 'Navier-Stokes/Darcy Coupling: Modeling, Analysis, and Numerical Approximation'. In: *Revista Matemática Complutense* 22.2 (2009), pp. 315–426.

[DS85] D. M. Driver and H. L. Seegmiller. 'Features of Reattaching Turbulent Shear Layer in Divergent Channel Flow'. In: *AIAA Journal* 23.2 (1985), pp. 163–171.

[DUN18] *DUNE*. 2018. URL: `https://www.dune-project.org/`.

[FAO19] FAO. *Soil salinity management*. 2019. URL: `http://www.fao.org/tc/exact/sustainable-agriculture-platform-pilot-website/soil-salinity-management/en/`.

[Fat+15] E. Fattahia, C. Waluga, B. Wohlmuth, U. Rüde, M. Manhart and R. Helmig. 'Pore-scale lattice Boltzmann simulation of laminar and turbulent flow through a sphere pack'. In: *arXiv preprint arXiv:1508.02960* (2015).

[Fet18] T. Fetzer. 'Coupled Free and Porous-Medium Flow Processes Affected by Turbulence and Roughness'. PhD thesis. Universität Stuttgart, 2018.

[Fle+11] B. Flemisch, M. Darcis, K. Erbertseder, B. Faigle, A. Lauser, K. Mosthaf, S. Müthing, P. Nuske, A. Tatomir, M. Wolff et al. 'DuMu^{x}: DUNE for multi-{phase, component, scale, physics, ...} flow and transport in porous media'. In: *Advances in Water Resources* 34.9 (2011), pp. 1102–1112.

[For01] P. Forchheimer. 'Wasserbewegung durch Boden'. In: *Zeitschrift des Vereines Deutscher Ingenieure* 45 (1901), pp. 1781–1788.

[FSH16] T. Fetzer, K. M. Smits and R. Helmig. 'Effect of Turbulence and Roughnesson Coupled Porous-Mediu/Free-Flow Exchange Processes'. In: *Transport in Porous Media* 114.2 (2016), pp. 395–424.

[God59] S. K. Godunov. 'A difference method for numerical calculation of discontinuous solutions of the equations of hydrodynamics'. In: *Mat. Sb. (N. S.)* 47.3 (1959), pp. 271–303.

[Har83] A. Harten. 'High resolution schemes using flux limiters for hyperbolic conservation laws'. In: *Journal of Computational Physics* 49.3 (1983), pp. 357–393.

[Hel97] R. Helmig. *Multiphase Flow and Transport Processes in the Subsurface: A Contribution to the Modeling of Hydrosystems*. Springer, 1997.

[Hir06] C. Hirsch. *Numerical Computation of Internal and External Flows*. Vol. 2. Butterworth-Heinemann Limited, 2006.

[Hol95] M. Holmes. *Introduction to Perturbation Methods*. Springer, 1995.

[HSH12] J. Hou, F. Simons and R. Hinkelmann. 'Improved total variation diminishing schemes for advection simulation of arbitrary grids'. In: *International Journal for Numerical Methods in Fluids* 70 (2012), pp. 359–382.

[HW65] F. H. Harlow and J. E. Welch. 'Numerical Calculation of Time-Dependent Viscous Incompressible Flow of Fluid with Free Surface'. In: *The Physics of Fluids* 8.12 (1965), pp. 2182–2189.

[Jam+16] V. A. Jambhekar, E. Mejri, N. Schröder, R. Helmig and N. Shokri. 'Kinetic Approach to Model Reactive Transport and Mixed Salt Precipitation in a Coupled Free-Flow-Porous-Media System'. In: *Transport in Porous Media* 114.2 (2016), pp. 341–369.

[Jam11] V. A. Jambhekar. 'Forchheimer Porous-media Flow Models - Numerical Investigation and Comparison with Experimental Data'. Master thesis. Universität Stuttgart, 2011.

[JM00] W. Jäger and A. Mikelić. 'On the interface boundary condition of Beavers, Joseph and Saffman'. In: *SIAM Journal on Applied Mathematics* 60.4 (2000), pp. 1111–1127.

[KB04] A. V. Kuznetsov and S. M. Becker. 'Effect of the interface roughness on turbulent convective heat transfer in a composite porous/fluid duct'. In: *International Communications in Heat and Mass Transfer* 31.1 (2004), pp. 11–20.

[KBR98] S. L. Krist, R. T. Biedron and C. L. Rumsey. *CFL3D User's Manual (version 5.0)*. 1998. URL: `https://cfl3d.larc.nasa.gov/Cfl3dv6/cfl3dv6_v5manual.html`.

[Koc+18] T. Koch, D. Gläser, K. Weishaupt, S. Ackermann, M. Beck, B. Becker, S. Burbulla, H. Class, E. Coltman, T. Fetzer, B. Flemisch, C. Grüninger, K. Heck, J. Hommel, T. Kurz, M. Lipp, F. Mohammadi, M. Schneider, G. Seitz, S. Scholz and F. Weinhardt. *DuMu^x 3.0.0*. Dec. 2018. DOI: `10.5281/zenodo.2479595`. URL: `https://doi.org/10.5281/zenodo.2479595`.

[Kol41] A. N. Kolmogorov. 'The local structure of turbulence in incompressible viscous fluid for very large Reynolds numbers'. In: *Dokl. Akad. Nauk SSSR*. Vol. 30. 4. 1941, pp. 299–303.

[Kol42] A. N. Kolmogorov. 'Equations of Turbulent Motion in an Incompressible Fluid'. In: *Izvestia Academii Nauk USSR: Physics* 6.1–2 (1942), pp. 56–58.

[Kov48] L. I. G. Kovasznay. 'Laminar flow behind a two-dimensional grid'. In: *Mathematical Proceedings of the Cambridge Philosophical Society* 44 (1948), pp. 58–62.

[Kra+15] M. Krafczyk, K. Kucher, Y. Wang and M. Geier. 'DNS/LES studies of turbulent flows based on the cumulant lattice Boltzmann approach'. In: *High performance computing in science and engineering '14*. Springer, 2015, pp. 519–531.

[Kuz04] A. V. Kuznetsov. 'Numerical modeling of turbulent flow in a composite porous/fluid duct utilizing a two-layer k–ε model to account for interface roughness'. In: *International Journal of Thermal Sciences* 43.11 (2004), pp. 1047–1056.

[Lan15] Langley Research Center. *Turbulence Modeling Resource*. 2015. URL: `https://turbmodels.larc.nasa.gov/backstep_val.html`.

[Leo79] B. P. Leonard. 'A stable and accurate convective modelling procedure based on quadratic upstream interpolation'. In: *Computer Methods in Applied Mechanics and Engineering* 19.1 (1979), pp. 59–98.

[LeV02] R. J. LeVeque. *Finite Volume Methods for Hyperbolic Problems*. Cambridge University Press, 2002.

[LL08] L. Li and H. Liao. 'An improved r-factor algorithm for TVD schemes'. In: *International Journal of Heat and Mass Transfer* 51 (2008), pp. 610–617.

[LL94] F. S. Lien and M. A. Leschziner. 'Upstream monotonic interpolation for scalar transport with application to complex turbulent flows'. In: *International Journal for Numerical Methods in Fluids* 19 (1994), pp. 527–548.

[LS74] B. E. Launder and B. I. Sharma. 'Application of the energy-dissipation model of turbulence to the calculation of flow near a spinning disc'. In: *Letters in Heat and Mass Transfer* 1.2 (1974), pp. 131–137.

[LYC04] F.S. Lien, E. Yee and Y. Cheng. 'Simulation of mean flow and turbulence over a 2D building array using high-resolution CFD and a distributed drag force approach'. In: *Journal of Wind Engineering and Industrial Aerodynamics* 92.2 (2004), pp. 117–158.

[MMD16] F. Moukalled, L. Mangani and M. Darwish. *The Finite Volume Method in Computational Fluid Dynamics*. Springer, 2016.

[Mos+11] K. Mosthaf, K. Baber, B. Flemisch, R. Helmig, A. Leijnse, I. Rybak and B. Wohlmuth. 'A coupling concept for two-phase compositional porous-media and single phase compositional free-flows'. In: *Water Resources Research* 47 (2011).

[Mos14] K. Mosthaf. 'Modeling and Analysis of Coupled Porous-Medium and Free Flow with Application to Evaporation Processes'. PhD thesis. Universität Stuttgart, 2014.

[MT08] R. Munns and M. Tester. 'Mechanisms of Salinity Tolerance'. In: *Annual Review of Plant Biology* 59 (2008), pp. 651–681.

[NB17] D. A. Nield and A. Bejan. *Convection in Porous Media*. 5th ed. Springer, 2017.

[Par17] N. Parolini. 'Computational Fluid Dynamics - Course Notes'. Notes for the master in mathematical engineering. 2017.

[Pop06] S. B. Pope. *Turbulent Flows*. Cambridge University Press, 2006.

[Pra25] L. Prandtl. 'Bericht über Untersuchungen zur ausgebildeten Turbulenz'. In: *Zeitschrift für angewandte Mathematik und Mechcanik* 5.2 (1925), pp. 136–139.

[QSS07] A. Quarteroni, R. Sacco and F. Saleri. *Numerical Mathematics*. 2nd ed. Springer, 2007.

[Qua14] A. Quarteroni. *Numerical Models for Differential Problems*. 2nd ed. Springer, 2014.

[RMH15] I. Rybak, J. Magiera and R. Helmig. 'Multirate time integration for coupled saturated/unsaturated porous medium and free flow systems'. In: *Computational Geosciences* 19 (2015), pp. 299–309.

[Roe85] P. L. Roe. 'Some contributions to the modeling of discontinous flows'. In: *Lectures in Applied Mathematics* 22 (1985), pp. 163–193.

[Saf71] P. G. Saffman. 'On the boundary condition at the surface of a porous medium'. In: *Studies in Applied Mathematics* 50.2 (1971), pp. 93–101.

[Sal16] S. Salsa. *Partial Differential Equations in Action: From Modelling to Theory*. 3rd ed. Springer, 2016.

[SG17] H. Schlichting and K. Gersten. *Boundary-Layer Theory*. 9th ed. Springer, 2017.

[Spa72] D. B. Spalding. 'A Novel Finite-difference Formulation for Differential Expression Involving Both First and Second Derivatives'. In: *International Journal for Numerical Methods in Engineering* 4.4 (1972), pp. 551–559.

[SRA04] U. Shavit, R. Rosenzweig and S. Assouline. 'Free flow at the interface of porous surfaces: a generalization of the Taylor brush configuration'. In: *Transport in Porous Media* 54.3 (2004), pp. 345–360.

[Swe84] P. K. Sweby. 'High Resolution Schemes Using Flux Limiters for Hyperbolic Conservation Laws'. In: *SIAM Journal on Numerical Analysis* 21.5 (1984), pp. 995–1011.

[TK08] N. Targui and H. Kahalerras. 'Analysis of fluid flow and heat transfer in a double pipe heat exchanger with porous structures'. In: *Energy Conversion and Management* 49.11 (2008), pp. 3217–3229.

[Val07] L. Valdettaro. 'Dispense del corso di Teoria, Modellistica e Simulazione della Turbolenza'. Notes for the master in mathematical engineering. 2007.

[Van56] E. R. Van Driest. 'On Turbulent Flow Near a Wall'. In: *Journal of the Aeronautical Sciences* 23.11 (1956), pp. 1007–1011.

[Van74] B. Van Leer. 'Towards the ultimate conservative difference scheme II. Monotonicity and conservation combined in a second order scheme'. In: *Journal of Computational Physics* 14.3 (1974), pp. 361–370.

[Van77] B. Van Leer. 'Towards the ultimate conservative difference scheme III. Upstream-centered finite-difference schemes for ideal compressible flow'. In: *Journal of Computational Physics* 23.3 (1977), pp. 263–275.

[Van82] G. D. Van Alabada. 'A comparative study of computational methods in cosmic gas dynamics'. In: *Astronomy and Astrophysics* 108 (1982), pp. 76–84.

[Ver+06] P. Verboven, D. Flick, B. Nicolaï and G. Alvarez. 'Modelling transport phenomena in refrigerated food bulks, packages and stacks: basics and advances'. In: *International Journal of Refrigeration* 29.6 (2006), pp. 985–997.

[VM07] H. K. Versteeg and W. Malalasekera. *An Introduction to Computational Fluid Dynamics: The Finite Volume Method*. 2nd ed. Pearson Education Limited, 2007.

[Wal08] L. Walter. 'Towards a model concept for coupling porousgas diffusion layer and gas distributor in PEM fuel cells'. Master thesis. Universität Stuttgart, 2008.

[War64] J. C. Ward. 'Turbulent flow in porous media'. In: *Journal of the Hydraulics Division* 90.5 (1964), pp. 1–12.

[Wil06] D. C. Wilcox. *Turbolence Modeling for CFD*. 3rd ed. DCW industries, 2006.

[Wil08] D. C. Wilcox. 'Formulation of the k-ω Turbulence Model Revisited'. In: *AIAA Journal* 46.11 (2008), pp. 2823–2838.

[Wit86] S. Withaker. 'Flow in Porous Media I: A Theoretical Derivation of Darcy's Law'. In: *Transport in Porous Media* 1 (1986), pp. 3–25.

[Wit96] S. Withaker. 'The Forchheimer equation: a theoretical development'. In: *Transport in Porous Media* 25 (1996), pp. 27–61.

[Wit99] S. Withaker. *The Method of Volume Averaging*. Springer, 1999.

[WJH19] K. Weishaupt, V. Joekar-Niasar and R. Helmig. 'An efficient coupling of free flow and porous media flow using the pore-network modeling approach'. In: *Journal of Computational Physics: X* 1 (2019), p. 100011.

[Wol13] M. Wolff. 'Multi-Scale Modeling of Two-Phase Flow in Porous Media including Capillary Pressure Effects'. PhD thesis. Universität Stuttgart, 2013.

[Wu16] H. Wu. 'A review of recent development: Transport and performance modeling of PEM fuel cells'. In: *Applied Energy* 165.C (2016), pp. 81–106.

[Yan+18] G. Yang, B. Weigand, A. Terzis, K. Weishaupt and R. Helmig. 'Numerical Simulation of Turbulent Flow and Heat Transfer in a Three-Dimensional Channel Coupled with Flow Through Porous Structures'. In: *Transport in Porous Media* 122.1 (2018), pp. 145–167.

[YL05] L. You and H. Liu. 'A two-phase flow and transport model for PEM fuel cells'. In: *Journal of Power Source* 155 (2005), pp. 219–230.

[Zen13] X. Zeng. 'A general approach to enhance slope limiters on non-uniform rectilinear grids'. In: *arXiv preprint arXiv:1301.0967* (2013).